

DOKUZ EYLÜL UNIVERSITY
GRADUATE SCHOOL OF NATURAL AND APPLIED SCIENCES

**INVESTIGATION OF FAN DRIVEN FLOW
FIELDS BY PARTICLE IMAGE VELOCIMETRY
AND INFRARED THERMOGRAPHY**

by
Özgün ÖZER

December, 2017
İZMİR

**INVESTIGATION OF FAN DRIVEN FLOW
FIELDS BY PARTICLE IMAGE VELOCIMETRY
AND INFRARED THERMOGRAPHY**

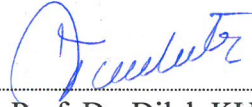
**A Thesis Submitted to the
Graduate School of Natural and Applied Sciences of Dokuz Eylül University
In Partial Fulfillment of the Requirements for the Degree of Doctor of
Department of Mechanical Engineering**

**by
Özgün ÖZER**

**December, 2017
İZMİR**

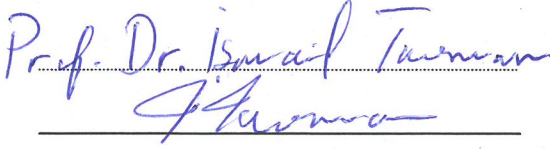
Ph.D. THESIS EXAMINATION RESULT FORM

We have read the thesis entitled “INVESTIGATION OF FAN DRIVEN FLOW FIELDS BY PARTICLE IMAGE VELOCIMETRY AND INFRARED THERMOGRAPHY” completed by ÖZGÜN ÖZER under supervision of PROF. DR. DİLEK KUMLUTAŞ and we certify that in our opinion it is fully adequate, in scope and in quality, as a thesis for the degree of Doctor of Philosophy.

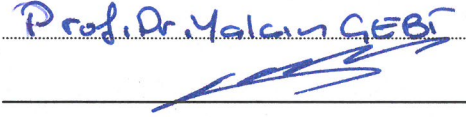


Prof. Dr. Dilek KUMLUTAŞ

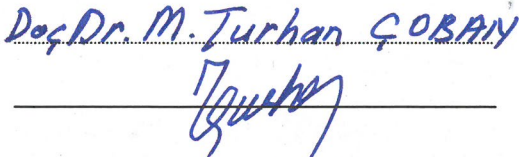
Supervisor



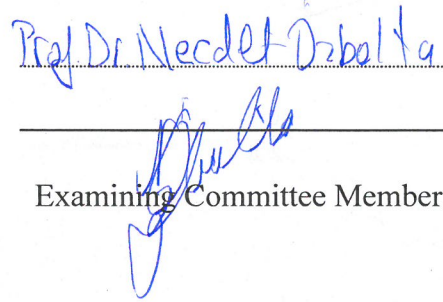
Thesis Committee Member



Thesis Committee Member



Examining Committee Member



Examining Committee Member



Prof. Dr. Kadriye ERTEKİN

Director

Graduate School of Natural and Applied Sciences

ACKNOWLEDGMENT

In the memory of Cengiz ÖZER. The man who created me, educated me and helped me to shape my ideals.

I would like to thank the project executive and my supervisor Prof. Dr. Dilek KUMLUTAŞ. She is a second mother to me. It is a great honor to work with her.

This thesis was supported by the Ministry of Science, Industry and Technology and Vestel Washing Machine Company with the 00998.STZ.2011-2 encoded SANTEZ project. I would like to express my gratitude about being in this project.

This thesis was supported by The Scientific and Technological Research Council of Turkey (TUBİTAK) and Vestel Air-Conditioner Company with the 5140039 encoded 1505 project. It was also supported by The Scientific and Technological Research Council of Turkey and Vestel Cooker Company with project grant no. TEYDEB 3130615. I would like to express my gratitude about being in this projects.

I would like to specially thank to my colleague M. Sc. Utku Alp YÜCEKAYA. We handled all the hardships of research together. I would also like to thank our CFD group, Hasan AVCI, Funda KURU, Berrin EKER, Gürkan ÇALIŞKAN. Working with them is a pleasure.

I would also like to thank the engineering team at R&D department of Vestel Company. Especially İlhami GÜMÜŞ, Soner SUDA, Kadir BOZDEMİR, Cem DEMİRKESEN thank you for your support and contributions on experiments.

I would like to thank to my dear wife Ayça YÜKSEL ÖZER, my daughter Işık, my beloved mother Suna ÖZER, Sevgi YÜKSEL and Yaşar YÜKSEL for supporting me to follow my ideals. They make my life meaningful. Lastly my gratitude to Çağlar EBEPERİ. Best support of my life in every area and aspect.

Özgün ÖZER

INVESTIGATION OF FAN DRIVEN FLOW FIELDS BY PARTICLE IMAGE VELOCIMETRY AND INFRARED THERMOGRAPHY

ABSTRACT

In this thesis, fan driven flow fields were investigated by using Particle Imaging Velocimetry (PIV) and infrared thermography methods.

In this context, appropriate improvements have been made primarily in the PIV method. In addition, Three Dimensional Meshed Infrared Temperature Measurement method has been developed that can measure the volumetric temperature distribution of air with a single camera.

Then these methods were then used to examine the impulsive flows of the fans used in practice.

In the third chapter, the flow structure of the cross flow fan in the Split Air Conditioner Indoor unit was investigated parametrically with the Particle Image Velocimetry Method. In the study, 420 design alternatives were evaluated. As a result of the examination made, the best design was obtained in the examined parameter range. In addition, the effects of the examined parameters on the design parameters were evaluated.

In the fourth chapter, these methods have been used to improve the cooling of a pyrolytic oven door. As a result of the work done, the average air velocity between the oven glasses was increased by 40.8% without increasing the fan rotation. Thus, the door surface temperature is reduced by 12 K.

In the fifth chapter, the flow driven by the axial fan in the Split Air Conditioner Outdoor Unit was investigated and appropriate improvements were made to the outdoor unit design. In addition, a unique outdoor unit design and prototype production with cross flow fan has been realized.

In the sixth chapter, the flow structure of the centrifugal fan in a washing machine with the drying feature is examined. As a result of the work done, the design of the drying duct has been improved.

In the seventh chapter, studies on the Three Dimensional Networked Temperature Measurement Method developed within the scope of the present thesis are presented.

As a result of all the work done, the methods developed and used for examining the flow structures of the fans are used in the examination of the flow patterns of the fans in the application. With the information obtained, the increase energy efficiency and other properties of these systems were improved.

Keywords: Particle image velocimetry, infrared thermography, 3D meshed infrared thermography, split air conditioner, pyrolytic oven, washer dryer

FANIN SÜRDÜĞÜ AKIŞ ALANLARININ PARÇACIK GÖRÜNTÜLEMELİ HIZ ÖLÇÜMÜ VE KIZILÖTESİ GÖRÜNTÜLEME İLE İNCELENMESİ

ÖZ

Bu tez kapsamında fanların ittiği akış yapıları, parçacık görüntülemeli hız ölçümü ve kızıl ötesi sıcaklık ölçümü yöntemleri kullanılarak incelenmiştir.

Bu kapsamda, öncelikle parçacık görüntülemeli hız ölçümü yönteminde amaca uygun geliştirmeler yapılmıştır. Ayrıca havadaki hacimsel sıcaklık dağılımını tek kamera ile incelenebilen Üç Boyutlu Ağ Yapılı Kızılötesi Sıcaklık Ölçümü yöntemi geliştirilmiştir.

Daha sonra bu yöntemler uygulamada kullanılan fanların ittiği akışların incelenmesi için kullanılmıştır.

Üçüncü Bölümde, Split Klima İç ünitesindeki çapraz akışlı fanın akış yapısı parametrik olarak Parçacık Görüntülemeli Hız Ölçümü Yöntemi ile incelenmiştir. Çalışmada 420 adet tasarım alternatifi değerlendirmiştir. Yapılan inceleme sonucunda incelenen parametre aralığında en iyi tasarım elde edilmiştir. Ayrıca incelenen parametrelerin, tasarım parametrelerine etkileri değerlendirilmiştir.

Dördüncü bölümde bu yöntemler, pirolitik bir fırın kapısının soğutulmasının iyileştirilmesi için kullanılmıştır. Yapılan çalışmalar sonucunda, fan devri arttırılmadan sadece tasarım geliştirmeleri ile cam arası ortalama hava hızı yüzde 40.8 arttırılmıştır. Böylece, kapı yüzey sıcaklığı 12 K düşürülmüştür.

Beşinci bölümde, Split Klima Dış Ünitesindeki eksenel fanın sürdüğü akış incelenmiş ve dış ünite tasarımında uygun geliştirmeler yapılmıştır. Ayrıca çapraz akış fanlı özgün bir dış ünite tasarımı ve prototip üretimi gerçekleştirilmiştir.

Altıncı bölümde kurutma özelliğine sahip bir çamaşır makinasının içinde bulunan santrifüj fanın akış yapısı incelenmiştir. Yapılan çalışma sonucunda kurutma kanalının tasarımı geliştirilmiştir.

Yedinci bölümde ise mevcut tez kapsamında geliştirilen Üç Boyutlu Ağ Yapılı Kızılötesi Sıcaklık Ölçümü Yöntemi ile ilgili yapılan çalışmalar sunulmuştur.

Yapılan tüm çalışmaların sonucunda, fanların ittiği akış yapılarının incelenmesi için geliştirilen ve bulunan yöntemler, uygulamadaki fanların akış yapılarının incelenmesinde kullanılmıştır. Elde edilen bilgiler ile bu sistemlerin geliştirilmesi ve enerji verimliliğinin artırılması sağlanmıştır.

Anahtar Kelimeler: Parçacık görüntülemeli hız ölçümü, kızılötesi sıcaklık ölçümü, üç boyutlu ağ yapılı kızılötesi sıcaklık ölçümü, split klima, pirolitik fırın, yıkayıcı kurutucu çamaşır makinası

CONTENTS

	Page
M.Sc THESIS EXAMINATION RESULT FORM	ii
ACKNOWLEDGMENTS	iii
ABSTRACT	iv
ÖZ	vi
LIST OF FIGURES	xii
LIST OF TABLES	xvii
CHAPTER ONE - INTRODUCTION	1
1.1 Literature	2
1.1.1 Literature Search on Cross Flow Fans and Split Air Conditioners.....	2
1.1.2 Literature Search on Axial Fans and Split Air Conditioners	5
1.1.3 Literature Search on Centrifugal Fans and Drier Washing Machines	6
1.1.4 Literature Search on Pyrolytic Ovens	9
1.1.5 Literature Search on Particle Image Velocimetry.....	11
1.1.6 Literature Search on Meshed Infrared Thermography and Measurement Screens.....	15
1.2 Aim and Motivation	19
CHAPTER TWO - METHODOLOGY.....	21
2.1 Particle Image Velocimetry	21
2.1.1 Particle Image Velocimetry Experiment System Components	23
2.1.1.1 Two pulse ND:YAG Laser	24
2.1.1.2 Particle Image Velocimetry Camera	26
2.1.1.3 Synchronizer	28
2.1.1.4 Particles and Mist Generator (Seeder)	28
2.1.1.5 Computer and Software.....	31
2.1.2 Obtaining Volumetric Average Flow Data by Stereo Particle Image Velocimetry	32

2.2 Three Dimensional Meshed Infrared Thermography	36
2.2.1 Validation.....	43
CHAPTER THREE - EXPERIMENTAL INVESTIGATION ON CROSS FLOW FAN'S CASING PARAMETERS INSIDE OF A SPLIT AIR CONDITIONER INDOOR UNIT BY STEREO PARTICLE IMAGE VELOCIMETRY	45
3.1 The Parametric Prototype of the Split Air Conditioner Indoor Unit and Investigated Parameters	46
3.2 Stereo Particle Image Velocimetry Parameters of the Study	51
3.3 Output Parameters	51
3.4 Results	53
3.4.1 Individual Parameter Effect on Split Air Conditioners Flow Structure.....	58
3.4.1.1 The Effect of Tongue Angle	59
3.4.1.2 The Effect of Vortex Wall Angle.....	60
3.4.1.3 The Effect of Vortex Wall Distance.....	60
3.4.1.4 The Effect of Volute Curvature.....	61
3.4.1.5 The Effect of Heat Exchanger.....	62
3.4.2 The Overall Effect of Investigated Parameters on Split Air Conditioner's Flow Structure	63
3.4.3 Investigation and Experimental Validation on Full Model	65
3.4.3.1 Calculation of the Correction Factor.....	66
3.4.3.2 The Effects on Noise.....	67
3.4.4 Repeatability Experiments and Validation	68
CHAPTER FOUR - INVESTIGATION OF THE CROSS-FLOW FAN INSIDE OF AN ASPIRATING COOLING SYSTEM FOR REGULATING TEMPERATURE OF PYROLYTIC OVEN GLASS	70
4.1 Numerical Study	70
4.2 Validation of Computational Fluid Dynamics Results.....	74

4.2.1 Fluid Flow Verification	74
4.2.2 Temperature Distribution Verification	77
4.3 Parametric Study	79
4.3.1 Effects of Position of the Cross-Flow Fan.....	79
4.3.2 Effects of Design of the Upper Blowing Channel.....	83
4.3.3 Effect of Rotational Speed of Cross-Flow Fan.....	85
4.3.4 The Cumulative Effects of Parametric Studies on Aspirating Cooling System to the Surface Temperatures	87

CHAPTER FIVE - IMPROVEMENT OF FLOW STRUCTURE. HEAT TRANSFER AND PERFORMANCE OF SPLIT AIRCONDITONER OUTDOOR UNITS AND DESIGN PROCESS OF NOVEL CROSS-FLOW FAN OUTDOOR UNIT..... 89

5.1 Design and Comparison of Alternative Axial Fan Designs With Numerical and Experimental Methods.....	90
5.1.1 Numerical and Experimental Methods of Designing Conventional Outdoor Unit with Alternative Axial Fan	92
5.1.2 Evaluation of Alternative Add-ons on Blade Forms for Reducing the Noise	96
5.2 Design of Split Air Conditioner Outdoor Unit with Cross-Flow Fan	101
5.2.1 Numerical Model and Parametric Analyses	103
5.2.2 The Production Process of the Split Air Conditioner Outdoor Unit Prototype with Cross Flow Fan.....	110
5.2.3 Investigation Experimental of the Cross Flow Fan Outdoor Unit Prototype	113
5.3 Comparison of Outdoor Unit with Axial and Cross Flow Fan.....	117

CHAPTER SIX - IMPROVING THE DESIGN OF WASHING MACHINE WITH DRYING FEATURE AND INCREASING ITS EFFICIENCY 120

6.1 Particle Image Velocimetry Experiments at the Output Section of the Centrifugal Fan 120

6.2 Investigation of the 3D Flow Profile of the Centrifugal Fan Output Mouth.. 128

6.3 Investigation of the 3D Flow Profile of the Centrifugal Fan Suction Mouth. 130

6.4 Comparison of Alternative Centrifugal Fans 131

6.5 Single Piece Heating Housing Design Studies 132

CHAPTER SEVEN - COMPARISON EXPERIMENTS OF 3D MESHED INFRARED THERMOGRAPHY 139

7.1 Experimental Comparison of Two Dimensional Targets 139

7.1.1 Comparison of Temperature Measurement Capabilities of Measurement Screens..... 139

7.2 3D Flow Structure Validation of 3D Meshed Infrared Thermography by Particle Image Velocimetry 142

CHAPTER EIGHT - CONCLUSION..... 144

REFERENCES 148

LIST OF FIGURES

	Page
Figure 1.1 General working principle schematic of a CFF inside of a SAC	3
Figure 1.2 The forward oblique blade centrifugal fan geometry and the velocity field taken from the central plane of the fans with varying amount and size of fans	7
Figure 1.3 The measurement points in the centrifugal fan and at the output section that are used for acoustic pressure measurements in the study conducted by Velarde-Suarez, Ballesteros-Tajadura, Hurtado-Cruz, Santolaria-Morros	8
Figure 1.4 a) Flow area channel $Q/Q_0=1$, b) Flow area channel $Q/Q_0=0.5$	9
Figure 1.5 The average heat and velocity areas on cooling inside the passenger cabin of a plane	14
Figure 2.1. The 3D model of the orientation of cameras, laser and prototype.....	22
Figure 2.2 The schematic of the experiment room	23
Figure 2.3 Elementary kinds of interactions between atoms and electromagnetic radiation, a) Absorbing, b) Spontaneous Emission, c) Stimulated Emission	25
Figure 2.4 Photo of the current laser	26
Figure 2.5 Photo of the current cameras	27
Figure 2.6 Particle distribution images	30
Figure 2.7 Photo of the current seed generator	31
Figure 2.8 Outdoor unit SPIV setup.....	33
Figure 2.9 Positions of the examination planes measured in the PGHÖ experiments for examining the volumetric flow distributions of the external units.....	34
Figure 2.10 Planar mean velocity distribution map obtained from the stereo PIV of the upper scan area of the axial fan of the SAC outdoor unit.	34
Figure 2.11 Velocity iso-surfaces of the split air conditioning outdoor unit at the blowing zones (3-8 m/s).....	35
Figure 2.12 Average scalar velocity distribution map of the split air conditioning outdoor unit at the blowing zones	36
Figure 2.13 Three dimensional meshed infrared thermography setup.....	37
Figure 2.14 a) Target projection on sensor, b) Simulated temperature map.....	40

Figure 2.15 Optical schematic of 3D MIT setup.....	41
Figure 2.16 Linear regression fitting between validation experiments.....	43
Figure 3.1 The parametric prototype of the SAC indoor unit	47
Figure 3.2 The schematic the blade parameter and the SAC	48
Figure 3.3 Averaged two dimensional three component flow structures of selected design points.....	55
Figure 3.4 Total pressure coefficient-Flow coefficient graphs	
a- Total pressure coefficient-Flow coefficient graph of all experiment, grouped according to heat exchanger.	
b- Total pressure coefficient-Flow coefficient graph of experiments without heat exchanger grouped according volute curvature.	
c- Total pressure coefficient-Flow coefficient graph of experiments without heat exchanger grouped according tongue angle.	
d- Total pressure coefficient-Flow coefficient graph of experiments without heat exchanger grouped according vortex wall distance.	
e- Total pressure coefficient-Flow coefficient graph of experiments without heat exchanger grouped according vortex wall angle.....	56
Figure 3.5 Comparison of the average flow profiles in scenarios with and without the heat exchanger	62
Figure 3.6 Average volumetric velocity iso-surfaces at the outflow area of the SAC prototype, selected based on the results of the parametric study	66
Figure 3.7 Sound power level - flow rate graphs	67
Figure 3.8 Velocity profile comparison between experiment and the validation experiment at design point 160	69
Figure 4.1 Pyrolytic oven views a) aspirating cooling system, b) pyrolytic oven assembly, c) oven door, d) top view of oven	71
Figure 4.2 Three dimensional air volume model a) model of oven door and aspirating cooling system, b) model of CFF air, c) model of oven door and air circulation of the oven, d) boundary conditions of model	72
Figure 4.3 Mesh details of the air volume model a) mesh detail of oven door and aspirating cooling system, b) mesh detail of oven door, c) mesh detail of fan, d) front view of fans' mesh detail.	73

Figure 4.4 Arrangement of anemometers in experimental study.....	75
Figure 4.5 Fluid flow of CFD study a) ACS and oven door, b) details of the inlet and outlet ACS.....	76
Figure 4.6 The temperature distribution of the outer surface of oven door a) experimental results, b) computational results.....	77
Figure 4.7 Scatter plot comparing the numerical and experimental temperature data.....	79
Figure 4.8 Mechanical construction of CFF.....	79
Figure 4.9 a) Air volume model of ACS, b) Cross-sectional view of ACS air volume model.....	80
Figure 4.10 Velocity vectors of ACS a) inlet channel and CFF tangent, b) back wall 2.5 mm from CFF, c) back wall move away 5 mm from CFF.....	81
Figure 4.11 The optimum positioning of the inlet channel depending on the boundary wall of interior body a) pressure contours of ACS, b) schematic view of CFF.....	82
Figure 4.12. The structure of upper blowing channel.....	83
Figure 4.13 Pressure comparison between design points of upper blowing channel.....	85
Figure 4.14 The effect of speed of the CFF on the outer surface of oven door.....	87
Figure 5.1 Screenshot taken in fanpal fan design process.....	91
Figure 5.2 Screenshot taken in the fan design process in AxCent.....	91
Figure 5.3 Photographs of newly designed and produced fans.....	92
Figure 5.4 Parameters of the examined profile.....	93
Figure 5.5 Air Flow Rate-RPM of axial outdoor fan graph.....	95
Figure 5.6 Noise-air flow rate comparison of axial outdoor fans.....	96
Figure 5.7 Form used on aircraft wings to break the tip vortex.....	97
Figure 5.8 Rain drop parameters.....	97
Figure 5.9 Velocity distribution map of the blade without droplet form add-on.....	99
Figure 5.10 Velocity distribution map of the droplet design providing the highest performance as the result of the 250 analysis.....	99
Figure 5.11 Fan prototype named V4R1 with added droplet form.....	100
Figure 5.12 Final prototype of outdoor unit with axial fan.....	100

Figure 5.13 Outdoor unit with CFF in which the fans are vertically. a) Exterior view, b) Compressor positioning	102
Figure 5.14 Outdoor unit with CFF in which the fans are horizontally positioned a) Exterior view, b) Compressor positioning	102
Figure 5.15 Air model for CFD	104
Figure 5.16 Schematic of the parameters examined on the outdoor unit design with CFF.....	105
Figure 5.17 Velocity distribution map of design number 20	108
Figure 5.18 Pressure distribution map of design number 20	108
Figure 5.19 Vorticity distribution map of design number 20.....	109
Figure 5.20 The CFF cut of prototypes used for endoscopic PIV	110
Figure 5.21 The effects of tongue angle on Estimated volumetric flow rate and average velocity	111
Figure 5.22 Front view of the prototype of the outdoor unit with CFF	112
Figure 5.23 Rear view of the final prototype of the outdoor unit with CFF	113
Figure 5.24 Investigation of prototype of outdoor unit with CFF by stereo PIV method	114
Figure 5.25 Planar mean three-component velocity distribution maps.....	115
Figure 5.26 Velocity isosurfaces of volumetric average three component flow field of CFF obtained by PIV (3-5 m/s).....	115
Figure 5.27 Noise test results of the Outdoor unit with CFF	116
Figure 5.28 Air flow rate test results of the Outdoor unit with CFF.....	116
Figure 5.29 Air flow rate-RPM chart.....	118
Figure 5.30 Noise-Air flow rate comparison chart	118
Figure 6.1 The photograph of the PIV experiments conducted at the output mouth of the centrifugal fan.....	121
Figure 6.2 3D vector maps compiled from PIV experiments	123
Figure 6.3 Locations of the investigated planes on the flow structure.....	128
Figure 6.4 Matching velocity surfaces illustrated on the volumetric 3D velocity data obtained via interpolation of the planar 3D velocity data compiled throughout the blowing mouth of the centrifugal fan (Inner Surface 12 m/s, Central Surface 7 m/s, Outer Surface 3 m/s).....	129

Figure 6.5 Matching velocity surfaces illustrated on the volumetric 3D velocity data obtained via interpolation of the planar 3D velocity data compiled throughout the suction mouth of the centrifugal fan (Outer 1 m/s, central 2 m/s, inner 3m/s).....	130
Figure 6.6 Matching velocity surfaces illustrated on the volumetric 3D velocity data obtained via interpolation of the planar 3D velocity data compiled throughout the blowing mouth of the centrifugal fan (Inner Surface 7 m/s, Outer Surface 3 m/s) (a) the current high diameter plastic fan (b) small diameter metal fan.....	131
Figure 6.7 3D model of the single piece heater housing design works.....	132
Figure 6.8 Air volume geometries of drier group a) Current state b) Design offer .	133
Figure 6.9 The downside view of the prototype heating housing manufactured for design offer-2.....	134
Figure 6.10 The side view of the prototype heating housing manufactured for design offer.....	135
Figure 6.11 The routing plastic section of the prototype heating housing manufactured for design offer.....	135
Figure 6.12 The detailed photograph of the resistance section of the prototype heating housing manufactured for design offer.....	136
Figure 6.13 Matching velocity planes of the prior routing plastic part obtained via SPIV method.....	137
Figure 6.14 Matching velocity planes of the new routing plastic part obtained via SPIV method.	137
Figure 7.1 Comparison of average temperature measurement obtained by measurement screens and thermocouples	141
Figure 7.2 Comparison of average temperature distribution obtained by a) MIT, b) plane target, c) Thin wire target.....	141
Figure 7.3. A) Average volumetric temperature iso-surfaces of CFF obtained by 3D MIT, B) Average volumetric velocity iso-surfaces of CFF obtained by PIV	142

LIST OF TABLES

	Page
Table 2.1 Parameter list of MIT study	39
Table 3.1 The parameters list of chapter three	46
Table 3.2 List of the investigated parameters and the total number of experiments .	50
Table 3.3 The rotor parameters	50
Table 3.4 Input parameters of the experiments that are given at Figure 3.3.....	54
Table 3.5 Averaged results of the parametric experiments	59
Table 3.6 The comparison of the best case scenarios with and without the heat exchanger	64
Table 4.1 The study of determining optimum mesh model	73
Table 4.2 Comparison of the computational and the experimental study for the inlet and outlet channel of ACS unit	76
Table 4.3 Temperature comparison between experimental and computational results	78
Table 4.4 Variations of velocity due to sizes and angle of back wall.....	82
Table 4.5 Design data of upper blowing channel.....	84
Table 4.6 Velocity comparison between first and final model of ACS system	85
Table 4.7 Surface temperature distributions obtained from the comparison experiments (⁰ C)	88
Table 5.1 Parametric study result shows the best 28-profile design	94
Table 5.2 Parametric CFD results of droplets	98
Table 5.3 Parameters and inspection interval	104
Table 5.4 Results of the parametric CFD analyses	107
Table 6.1. Locations of the measurements planes.....	120

CHAPTER ONE

INTRODUCTION

As an object become more complex, some parts of it develop different duties to fulfill. These parts form an intricate whole which is called system. In systems, some subsystems create products that need to be processed by other subsystems or some subsystems use these products to accomplish other duties. So every complex system requires transport phenomena to achieve these tasks. This is true for all living systems from cell to world ecology and it is also true for machines and human-built systems of all kinds.

Fluids are the most suitable material for enabling this transport due to their mobility. They are also capable of transporting molecules, materials or heat. Blood is a good example of this phenomena for living system.

Blood, carries the necessary materials for life such as oxygen, adenosine triphosphate (ATP), etc. to the cells and the tissues, on the other hand it discharges the waste materials and heat generated by the breathing and other living activities. While mammals use blood for transport phenomena due to their size, smaller livings such as insects use gases for directly with tracheal respiration.

The machines also contain similar structures due to nature of the systems. For example, heart provides needed pressure to blood cycle through the body. The pumps, compressors and fans take over this task on the machines and they are very critical for the performance of the device.

For designing better systems, this transport phenomenon must be investigated. However, the complexity of the system and chaotic behavior of the fluids stacks up and create a complicated models which are very hard to solve theoretically.

One of the best way for investigating such complex systems, is optical experiment methods. The most important advantage of these methods, they give two or three dimensional data.

In the following parts of this chapter, the literature on fans and optical experimental methods are reviewed.

1.1 Literature

1.1.1 Literature Search on Cross Flow Fans and Split Air Conditioners

The working principle of a Split Air Conditioner (SAC) indoor unit is based on the phase change of the refrigerant inside the heat exchanger as the air is driven over the heat exchanger by a mechanical fan such that heat transfer takes place between the surface of the heat exchanger and the air.

The indoor unit design must be reasonably small for esthetical purposes, as it will be placed in the household. Also, the air velocity and the temperature at the exit of the unit must satisfy the comfort conditions. To satisfy these needs, Cross Flow Fans (CFFs) are widely used in air conditioning and household applications due to their compactness and low noise.

The CFF drives the air using an eccentric vortex. As the rotor blades pass near the vortex wall, the flow passes through an extremely narrow section between the blade and the vortex wall. This causes a huge increase in the flow velocity and a decrease in the static pressure, as Daniel Bernoulli suggested (Eck, 1973). The general working principle and the parameters of a CFF are shown schematically in Figure 1.1.

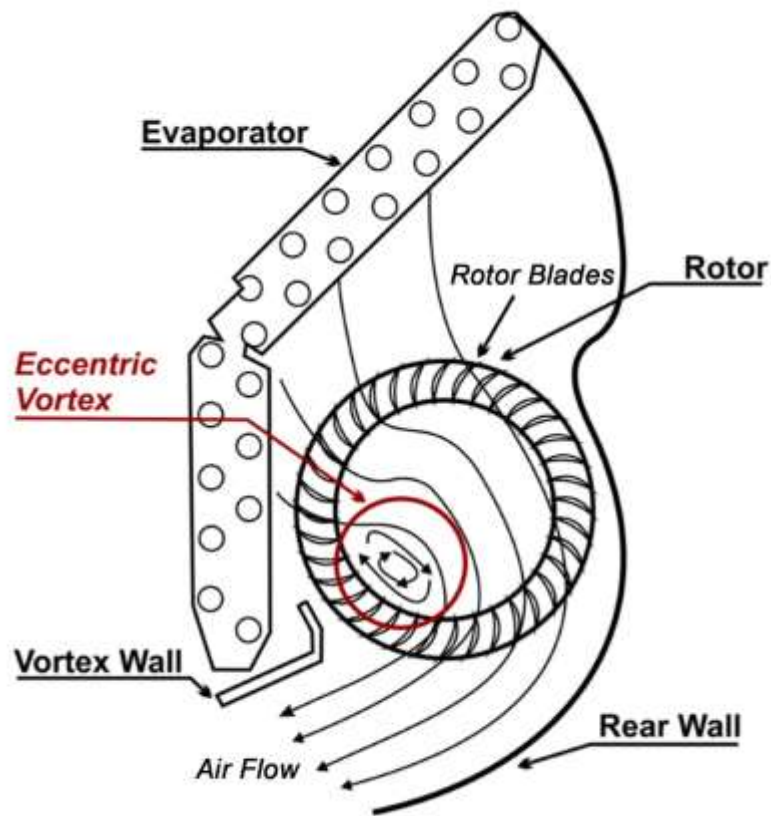


Figure 1.1 General working principle schematic of a CFF inside of a SAC (Özer & Kumlutaş, 2017)

Unlike axial fans, a CFF's ability to drive air is based on its casing. An axial fan can work without a casing, such as ventilator fans. A nozzle added to an axial fan generally increases the output speed. However, the same case is not always best when using CFFs. The fan will not drive the air in one direction without the vortex wall and the volute.

This working principle of CFFs was explained in Eck's book of "Fans" from 1973. Although the book provides insight for understanding the basic principles, the knowledge itself is not enough to optimise an individual system. Therefore, several studies have been published in the literature on enhancing these systems.

In late 1970s, Yamafuji (1975) studied the geometry of fan impellers, whereas Murata and Nisnihara (1976a; 1976b) studied the geometry of a fan's housing to improving the performance of a CFF. In all these experimental studies, qualitative flow

visualisation methods were used. Therefore, no quantitative whole field flow data were obtained due to inadequacies in the measurement technologies. These types of experimental studies continued until the early 2000s. There is a series of important studies conducted by Lazzaretto et.al between 2001 and 2003, which defined design parameters for the CFFs and suggested a systematic experimental approach to designing these systems (Lazzaretto, Lazzaretto A., Macor & Martegani, 2001; Lazzaretto, 2003; Lazzaretto, Toffolo & Martegani, 2003). Toffolo, Lazzaretto & Martegani (2003) followed these studies by investigating the flow field pattern inside of a CFF.

The number of the numerical studies on CFFs increased since commercial Computational Fluid Dynamics (CFD) programs advanced and became accepted in scientific investigations. One of the pioneers of this trend is Shih Y, Hou & Chiang's (2004, 2008) study, which investigates similarity laws for a CFF of a SAC. Afterwards, Toffolo (2005) studied the relationship between the design parameters of the geometrical configuration and fan performance.

In the early 1980s, Particle Image Velocimetry (PIV) was discovered to be an effective whole field, non-intrusive, quantitative visualisation technique (Adrian, 2005). After a decade of improvement, the PIV method began to be used in CFF flow field studies. Gabi et.al performed one of the first studies using PIV for investigating a CFF (Gabi, Dornstetter & Klemm, 2003). The study also showed that PIV is an effective tool for validating CFD data.

Kumlutaş et al. investigated CFFs inside of a SAC using a combination of CFD and Stereo PIV (SPIV) methods (Kumlutaş, Karadeniz & Kuru, 2013; Karadeniz, Kumlutaş & Özer, 2013). In the CFD study, the SPIV method is used to validate the CFD results. In the experimental part of the studies, whole outflow area is investigated plane by plane with SPIV to produce a three dimensional (3D) average flow profile of the fan.

In 2011, Casarsa and Giannattasio studied the 3D flow field in CFFs experimentally (Casarsa & Giannattasio, 2011). Instead of using SPIV they used mono-cam PIV for their investigation, which did not include the out-of-plane velocity components of the flow. Contemporary studies on CFF continue; one example is the Sun, Ouyang, Tian, Wu & Du Z (2015) study on an eccentric vortex in a CFF from 2015.

Finally, a study of this thesis, consisting of sections on CFFs and SACs, was published (Özer & Kumlutaş, 2017).

1.1.2 Literature Search on Axial Fans and Split Air Conditioners

After 2005, an increase in scientific studies on the topic of SAC outdoor units was observed. These studies can be grouped into two groups.

The first group of these studies evaluates increasing the efficiency of the SAC outdoor units by water cooling. Hu and Huang's work is an example of this. In the study, it was tried to increase the system efficiency with the water taken from the city water main (Hu & Huang, 2005). This work was followed by two studies by Hua Chen et al. In one of these studies, the system was examined numerically (Lee, Chen & Yik, 2008a) and in another experimental application was conducted for the Hong Kong urban climate numerically (Lee, Chen & Yik, 2008b).

The second issue that has an increasing number of scientific study, is the improvement of the performance of SACs. These works also can be divided into studies on the indoor unit and studies on the outdoor unit.

Studies on indoor units are more popular because they have more interaction with the users. They must be smaller, silent and esthetic. The design of the indoor units also effect the sales of the devices more. Therefore, while the technical parameters such as air velocity, volumetric flow rate, sound and heat transfer are preliminary design condition in the design of both the outdoor and indoor units, the space coverage and appearance also important for the indoor unit design.

However, the indoor and the outdoor units are inseparable parts of the SAC system and they need to be developed together in order to maximize system performance.

Wu et al. conducted studies to improve the aerodynamic and aero-acoustic performance of the SAC unit (Wu, Liu, & Pan, 2012). Following this work, Zhao and colleagues studied the estimation and measurement of aerodynamic and aero-acoustic performance of an axial fan in a SAC outdoor unit (Zhao, Sun & Zhang, 2013).

Wang and colleagues have tried to improve the aerodynamic performance of the output flow of the SAC exterior with the development of the nozzle design (Wang, Tian, Ouyang, Wu, & Du, 2014). This study was conducted both experimentally and numerically. Finally, Canepa and colleagues experimentally studied the effect of the distance between the rotor and the stator (Canepa, Cattanei & Zecchin, 2015).

Although acoustics are not directly covered by this thesis, the studies for reducing the energy consumption and vorticities has also reduced the sound levels of the devices.

1.1.3 Literature Search on Centrifugal Fans and Drier Washing Machines

As the literature is reviewed, it is seen that there are no publishing with the direct subject of washing machines and especially the washing machines with drier feature.

In the design of washing machine with drier feature, one of the critical components that influence the drying performance is the centrifugal fans that route the damp air to the condenser and then blowing the drying air to the drum through the resistances. No articles were found regarding the centrifugal fans within the washing machine with drying feature, however there are experimental and numerical studies that review the centrifugal fans independent from the system.

Younsi et al. have conducted numerical and experimental studies that investigate the forward oblique, non-uniform flow centrifugal fans and the acoustic behavior of the fans (Younsi, Bakır, Kouidri & Rey, 2007a; Younsi, Bakır, Kouidri & Rey, 2007b). Figure 1.2 shows the obtained velocity fields and the geometry of the fan that is used in these studies. In these studies it is determined that the blade sizes, the number of fan blades, the perimeter of the fan and the radial distance with the fan housing influence the noise and the performance of the fan. At the end of the study, a correlation between the fluctuation of pressure at the wall and the noise signals at the far section is found.

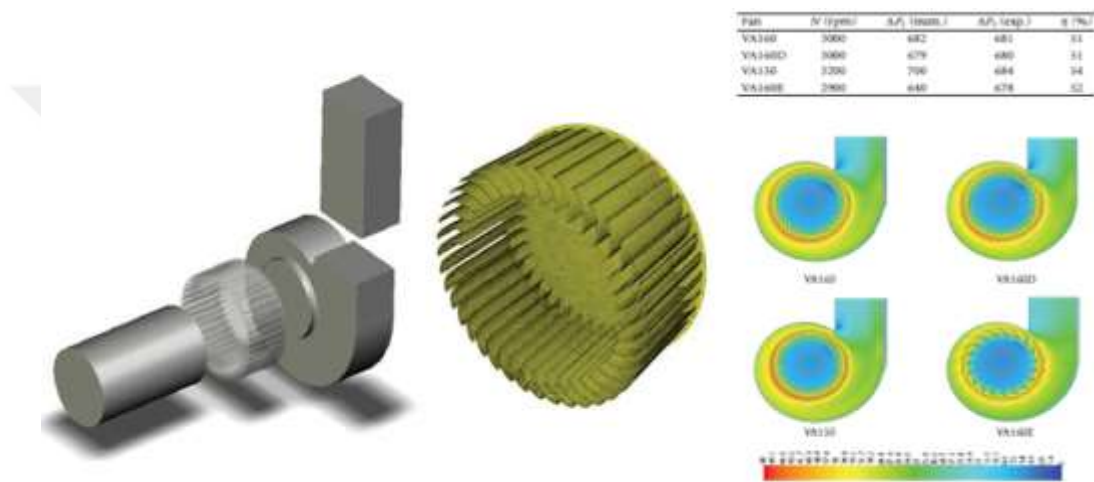


Figure 1.2 The forward oblique blade centrifugal fan geometry and the velocity field taken from the central plane of the fans with varying amount and size of fans (Younsi, Bakır, Kouidri & Rey, 2007a)

In the study conducted by Velarde-Suarez, Ballesteros-Tajadura, Hurtado-Cruz, Santolaria-Morros (2006) experimentally investigating the aerodynamic noise sources on centrifugal fans with backward oblique flap, acoustic pressure readings at the output section of the fan and pressure drop rates at the points on the fan housing surfaces specified in Figure 1.3 were measured. It is determined that the strongest source of noise is generated during the interaction between the fan housing routing tongue.

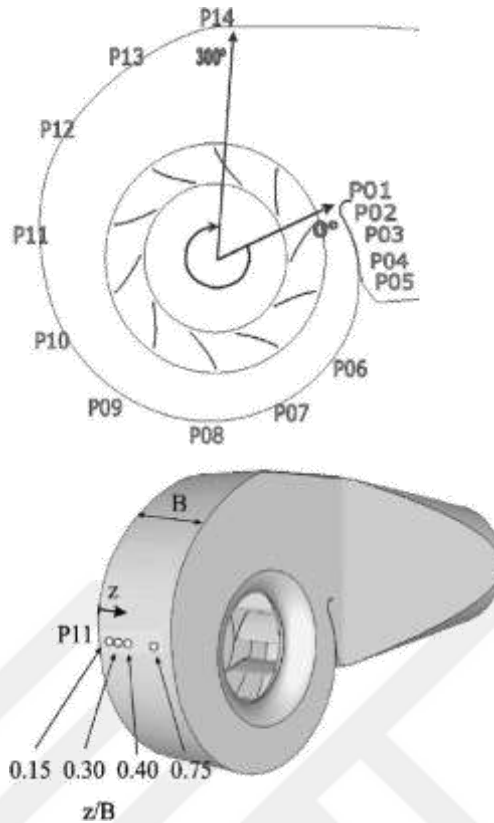


Figure 1.3 The measurement points in the centrifugal fan and at the output section that are used for acoustic pressure measurements in the study conducted by Velarde-Suarez, Ballesteros-Tajadura, Hurtado-Cruz, Santolaria-Morros (2006)

In another similar study conducted by Datong, Yijun, Xiaoliang, Minjian (2009) in order to lower the noise level on centrifugal fans, the performance and noise characteristics of the forward oblique centrifugal fans were collected and compared to determine the similarities and differences between the backward and forward oblique centrifugal fans, as specified in literature.

Then Bricaud, Richter, Dullenkopf & Bauer (2005) designed an stereo PIV setup which can determine the three-dimensional velocity field in the enclosed rotor–stator gap, in order to validate CFD calculations. The measurements result which are also given in Figure 1.4, showed the spreading of the jet inside the wheel space and the unsteady aspect of the flow, confirming that stereo PIV can successfully be applied in an enclosed rotor–stator system.

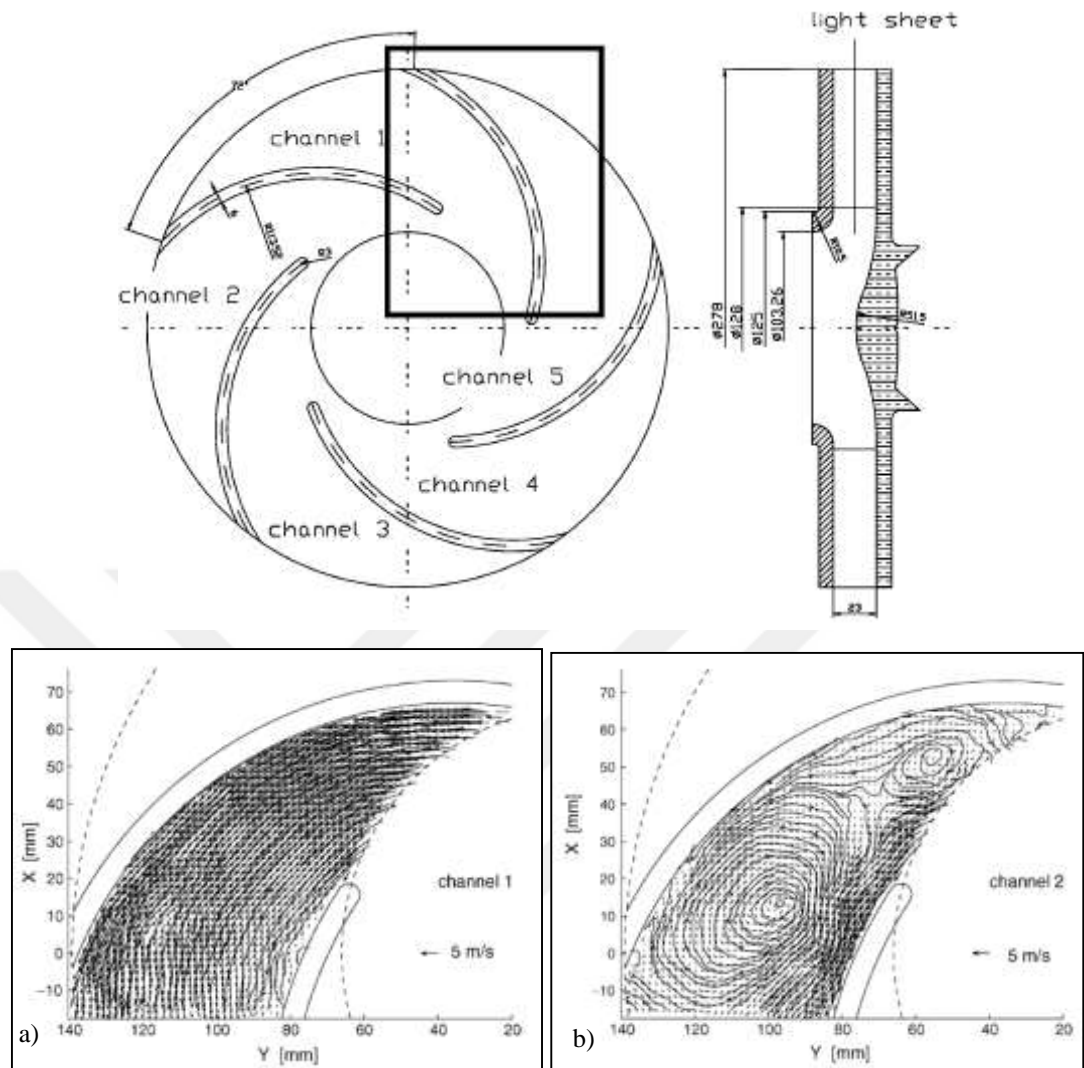


Figure 1.4 a) Flow area channel $Q/Q_0=1$, b) Flow area channel $Q/Q_0=0.5$ (Bricaud, Richter, Dullenkopf & Bauer, 2005)

1.1.4 Literature Search on Pyrolytic Ovens

In the design of domestic ovens, one of the most important parameters is outer glass temperature, especially in pyrolytic-type domestic ovens. Pyrolytic ovens have a self-cleaning function during which the temperature inside of the oven is increased over 500 °C. When the temperature inside the oven reaches these values, any food residue and grime adhered to the walls is simply burned off. This feature provides great convenience for users. However, this high-temperature increase should be considered with regards to safety. The outer surface temperature of the oven should be reduced to a safe level not harmful to the environment and living beings. An aspirating cooling

system (ACS) has been designed to reduce the temperature of the outer surface of the oven door. This system circulates air between panes through the door, thereby reducing the external surface temperature of the door by convective cooling. Here, the velocity of the suctioned air and the design of oven door are very important. If excessive cooling takes place, the temperature within the oven could decrease and affect the self-cleaning function. This would lead to low energy efficiency and performance of the door.

Rek et al. (2012) examined a newer generation, multifunctional oven and modeled radiative, conductive, natural and forced convective heat transfer mechanisms. They investigated many parameters that influence conditions inside an oven, such as the shape and power capacity of heaters, fan rotor rotational speeds, the thickness and quality of insulation and the design of the oven doors. Abraham et al. (2004) developed an algebraic method for predicting the time-based temperature variation of a thermal load situated in an electrically heated oven. Mistry et al. (2006) studied transient, natural convective heat transfer in ovens. A computer-aided design using computational fluid dynamics and heat transfer (CFDHT) modeling of an electric oven involves a three dimensional, unsteady, natural convective flow-thermal field coupled with radiative heat transfer. Mistry et al. (2011) developed a CFDHT-based methodology to evaluate the performance of a domestic gas oven. Fahey et al. (2008) studied cooling on circuit of the door of a pyrolytic oven. They used CFD and experimental techniques to understand the flow behavior of the oven. The CFD results were validated with experimental hot-wire velocity measurements. The study established an understanding on oven door's cooling circuit but they did not determine the effect of it or determine the design parameters. Verboven et al. (2000) investigated forced convection in an oven using CFDHT methods. They compared their numerical results with experimental results. Smolka et al. (2009) investigated forced convection inside a drying oven by using experimentally validated three dimensional CFDHT analyses. To improve the temperature uniformity within the oven cavity, they changed parameters, such as the rotational speed of the device fan, the effectiveness of the distribution gaps and the rate of heat generated by the electric heaters. Smolka et al. also changed configurations, such as the locations of the heaters, the fan and the fan

baffle. Overall, they improved the temperature uniformity and validated the results with an experimental test of the modified prototype.

As mentioned in the literature, the CFDHT method has been successfully applied for revealing and understanding complex flow characteristics. The three dimensional modelling of an oven is essential for determining the air-side flow and heat transfer characteristics. For the first time in the literature, an oven door and an ACS are modelled together as a whole three dimensional system. Therefore, in this study, an oven door, a CFF and an ACS were simultaneously introduced in a heat transfer and fluid flow analysis to determine the outer surface temperature distribution of the oven door. Before investigating the oven door and ACS together, the ACS was first independently modelled. The mechanical structures of the ACS were developed based on parametric studies. Then, the oven door and ACS were modelled together, and the flow field and the temperature distribution were investigated. The numerical results were validated by comparison with results obtained from experimental studies. To reduce the temperature on the oven door outer surface, the influence of the fan rotational speed was numerically investigated. The results of the parametric studies showed that the rotational speed of the CFF played an important role in regulating the outer surface temperature of the oven door.

1.1.5 Literature Search on Particle Image Velocimetry

PIV that will be utilized in order to monitor the flow and determine the velocity distribution, was first seen in the literature with the mentioned name in 1984, which is an optic method that is fairly new and progressing (Adrian, 2005). It is based on the principle of imaging the oscillating the particles within the flow as they pass through a light plane two times simultaneously and obtaining the velocity vector area by utilizing the obtained particle orientations. This method, primarily used for outbound flow issues, have progressed in tandem with the technological advancements and today it is utilized for resolving complex flow issues such as outbound and inbound flows with high turbulence density, jet streams. The study investigating the flow structure

between the centrifugal fan flaps by Bricaud, Richter, Dullenkopf & Bauer (2005) in Figure 1.4 is a fundamental example for similar studies.

Another study where PIV is utilized to investigate the fan flow structures is the 3D investigation of the axial fan that is utilized in an AC external unit with PIV and determination of the vortex formed around the flaps by J. H. Yoon & S. j. Lee (2004). It is also determined that the results obtained can be utilized in verification of the numerical resolution in the design phase. However, in this study the heat transfer is not investigated.

PIV should be viewed as an experiment apparatus instead of a measuring tool. As the system that is required to be measured change, two PIV systems may vary at a significant level although their essential components are the same.

Endoscopic PIV (EPIV) method is an important example. The method is developed in order to reach sections that are out of reach or unreachable for varying reasons. In this system a hole is drilled and laser or a camera is inserted within the system. Dierkshiede, Meyer, Hovestadt & Hentschel (2002) have investigated the performance of EPIV in their study. As a result of the study, it is specified that the endoscopic camera and endoscopic laser provide successful results. Although not being used industrially at a large scale, the system consisting both the endoscopic camera and laser have been successful. In another study by Auteri, Belan, Ceccon, Gibertini, Quadrio (2006) is the utilization of EPIV for investigating the flow inside helical pipes and the flow characteristics.

EPIV experiment systems continue to progress. European Union have formed a project to develop this system and the aim is to develop an enhanced EPIV system (both laser and camera in one endoscope). Various workshops are initiated with the support from the European Union. One of the subjects at the second workshop, is the utilization of EPIV in household appliances.

Two studies were conducted involving ovens. In oven designs, the hot air flow profile at the cooking section that is fundamental for a good cooking performance is investigated with this study (Alava, Onederra, Marin & Laresgoiti, 2003; Araneo, Coghe & Solero, 2003). In the conclusion section of the studies, the PIV results are compared with CFD (FLUENT program) and a good match is maintained. Due to the power of the laser and spatial resolution of the camera being low, PIV images were only obtained on one twelfth of the whole volume. In spite of this situation, the results being parallel indicates that PIV can be utilized to investigate a section of a system.

Furthermore, in these workshops stove hoods (Paone, Marassi & Santonicola, 2003) and lamps (Rita & Guzzini, 2003) are investigated. Their respective influence on the air flow of the kitchen or the room during their utilization are determined. In a study conducted by Lazzarato, Meneghin & Scattolin (2003) involving the AC units, the section between the fan of the AC and the heat exchanger is studied. In the study by Kim (2003), the air mix section of an AC unit is investigated and the specified sections are determined.

Other projects outside this studies were individually supported. One of these studies is the large scale PIV study (Kühn, Bosbach & Wagner, 2009). In this study, the air flow inside the passenger cabin of a plane is investigated (Figure 1.5). Here, it is investigated to determine how the air intakes to the cabin should be. Furthermore, the external elements that significantly influence the air flow inside the cabin are determined.

PIV is not solely utilized in engineering but also being used in medicine. From the book "Particle Image Velocimetry New Developments and Recent Applications", information can be found regarding the utilization of PIV in medicine, ranging from the blood flow in artificial hearts with PIV to studying air flows in respiratory systems (Schroeder & Willert, 2008).

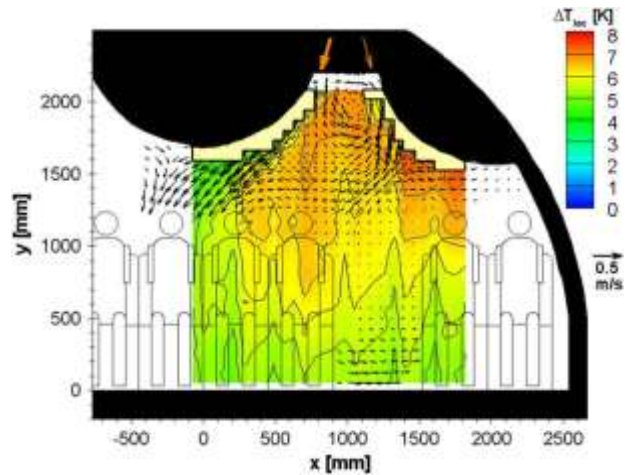


Figure 1.5 The average heat and velocity areas on cooling inside the passenger cabin of a plane (Kühn, Bosbach & Wagner, 2009)

This method, primarily used for outbound flow issues, have progressed in tandem with the technological advancements and today it is utilized for resolving complex flow issues such as outbound and inbound flows with high turbulence density, jet streams (Krause, Zahringer, Pap, 2005; Bricaud, Richter, Dullenkopf, Bauer, 2005).

In Wernet's (2000) study consisting centrifugal fans that is a turbo machine, the flow areas formed on the fans based on permanent conditions and conditions based on time are investigated with the PIV. With this method, the flow between the turbo machine flaps where complex flow is formed is visualized, compared with the CFD and this allowed the turbulence severity of the flow to be determined.

As the literature is reviewed, there are no known direct applications that is used in the centrifugal and similar fans that are utilized in the drier section of the washing machines with drier feature. The example studies investigating the performance and characteristics of the fan separate from the system referring to the CFD resolutions and the utilization of the PIV method are summarized above.

1.1.6 Literature Search on Meshed Infrared Thermography and Measurement Screens

Infrared imaging is being used to determine the temperature of the solid materials which are opaque in infrared wavelengths and radiate with definitive emissivity coefficient. However due to the fact that gases being transparent at infrared wavelength (7-13 μm), infrared cameras cannot determine the temperature of the gases directly. In literature, measurement screens are being used in order to solve this problem.

Measurement screen is a solid target that positioned in gas media which allows to determine the temperature of the gas via convection. The temperature distribution of measurement screen is obtained by imaging with infrared thermography. It must be noted that this method measures gases temperature indirectly therefore the success of the measurement depends on the heat transfer mechanism between the measurement screen and the gas. In this sense, there are different types of measurement screen targets in the literature.

These measurement screens are generally sheets or papers about a millimeter thickness with low thermal conductivity. These screens are placed inside the stream and a temperature distribution occurs on the surface with convective heat transfer. As the sheet or paper is thin, the temperature distribution detected by the infrared camera reflects the temperature distribution of the stream. However, as these sheets with vast surface area exchange heat via radiation with surrounding surfaces, the environmental impact shall be calculated and differentiated from the obtained results. In addition, as the measurement screen provides a barrier within the stream, it can only be applied to low velocity flow not to disrupt the general nature of the stream.

The first examples of the measurement screen method are Anderson, Hassani, & Kirkpatrick (1991) and later on by Burch, Hassani, & Penney (1992) is used to determine the temperature distribution in the aeration streams in a car. A 0.25 mm thickness fiberglass sheet (plane target) with a porosity of %70 was used as measurement screen. Comparison between the results of measurement screen and the

results of the calibrated thermocouple showed that the distribution of the temperature can be determined with ± 1.3 °C accuracy. Furthermore, the time response of measurement screen is set to 0.3 seconds.

Cehlin, Moshfegh, & Sandberg (2002) used a similarity of the method proposed by Anderson, Hassani, & Kirkpatrick (1991) to determine the temperature distribution over a large area at the outlet of the low-velocity diffuser used for in-room ventilation. In this method where the planar temperature distribution may be obtained; a sufficiently thin plane (plate or paper) manufactured from a low thermal conductivity. However, as a result of the flow area to be divided in two, the flow is distorted and the obtained heat distribution is not representative of the actual heat distribution of the air. Furthermore, due to the large surface area of the measurement screen conducting heat transfer with the environment and internal heat transfer of the measurement screen, the heat distribution on the target is altered and may lead the results to not to match with the heat distribution of the air. For this reason, Cehlin, Moshfegh, & Sandberg (2002) conducted a detailed analysis of the measurement uncertainty and error calculation.

Another application of the measurement screen method is Neto, Gamberio, & Costa (2006) was used to visualize the outflow of air curtain devices and to determine the temperature distribution. Unlike the work of Cehlin, Moshfegh, & Sandberg (2002), the air velocity was increased to 8 m / s at the exit of the air field instead of the lower flow velocities. Although the results that obtained were useful for determining the flow structure and the temperature distribution, Neto, Gamberio, & Costa (2006) stated that the nonporous measurement screen has disruptive effect on the flow due to barrier structure and also stated that the results of the experiments are not the same the analysis results.

In another study using a measurement screen, Elvsén, & Sandberg (2009) investigated the floating jet in a ventilated room. The instantaneous velocity and temperature distributions near the diffuser were visualized using different flow visualization method like Particle Streak Velocimetry (PSV), PIV and infrared thermography methods. They intended to reduce the radiation to the backside by using

a double layer measurement screen as suggested by Cehlin, Moshfegh, & Sandberg (2002). However, the aluminum foil used as the second layer in this method may increase the heat transfer inside the measuring screen which can cause measurement errors to increase.

Another study that the measurement screen is porous was made by Neely (2008). It was aimed to increase the visibility of the screen and reduce the effects on the flow by using net measurement screens with high porosity and spreading coefficient. The wires forming the measurement screen must be enough thin to reach the gas temperature to be measured, the net of the net target must be tight enough to ensure proper data in every pixel of the camera and the net material must be had a low reflection coefficient to reduce reflection from surrounding to the minimum. For this reason, different parameters (material type, flow characteristics, placement of the measurement screen, etc.) were measured in the flow at different temperatures to see the effect of the method on performance in Neely [6] study. As a result, although a measurement screen placed perpendicular to the flow created small effect on the flow, the background flow behind the screen was influenced by the presence of the screen and turbulence levels of the flow increased.

Gallo, Kunsch, & Rösger (2010) proposed a new measurement method based on infrared temperature measurement to determine the temperature distribution in hot gas flows. They calculated the local convection coefficient and fluid temperature by visualizing the temperature distribution on a high porosity net of electrically conductive thin wires with an infrared camera.

The natural convection on the heated plate was investigated by Vinnichenko, Plaksina, Yakimchuk, Soldatenkova, & Uvarov (2016). The temperature distribution was obtained with a measurement screen that was composed by rectangular targets. The results obtained from the measurement screen were compared with the results obtained with the BOS method and numeric study.

Beside these, another measurement screen method that is established as the “Meshed Infrared Thermography” (MIT) by the current study group (Karadeniz, Kumlutaş, & Özer, 2013). The temperature distribution at the outlet of the SAC indoor unit was visualized by this method. In this method; the temperature is measured by the spheres that are placed with pre-determined intervals on the nylon threads that are stretched between the two edges of a frame that is placed in the flow to have minimum effect on the flow. The benefits of the MIT method are minimal disruption on the flow that is ignorable and convenient measurement of the planar heat distribution with the utilized spheres.

Besides this method, Laser Induced Fluorescence (LIF) method that can measure the air temperature, is being used (Dabiri, 2009). In LIF method, the particles that fluorescence when illuminated with powerful laser beams shall be added to the flow. By illuminating the area to be reviewed, the particles are imaged with a high speed camera. The temperature is measured based on the fluorescence wavelength of the particles. This method is fairly expensive due to the high costs of the components such as high speed camera and laser. Furthermore, since the particles applied to the air is toxic to human health, the required precautions shall be in place of experiment.

Rayleigh Thermometry method takes place in literature in order to determine the air temperature (Miles, & Lempert, 1990). In this method, the flow is seeded with tracer particles and the stream is visualized by laser illumination. Rayleigh method differs from LIF method in that the added particles wavelength is smaller than transmitted laser wavelength. Therefore, this method can only be applied in clean laboratory. Moreover, Rayleigh method can only be used at high temperature. This method is expensive in terms of a component cost like LIF method. In addition, temperature can be measured from a thin plane in Rayleigh method. Therefore, it is not suitable for volumetric temperature measurement.

Furthermore, another method to determine the air temperature (and similar gasses) is to use a probe. Although this method is effective in determining the temperature at a given area, it can only perform point measurement. Thus, in order to determine the

heat dispersion in an area, the use of many point measurement devices is required. This leads to forming of quite complicated systems. In an event that a measurement is carried out via thermocouple or a probe scanning, temporal differences are observed and a traverse system is required.

In the current study, the simultaneous volumetric temperature distribution of infrared transparent flows (air, gases etc.) was obtained with minimum distortion on the flow structure by newly developed “3D Meshed Infrared Thermography (3DMIT)” method. In this method, the volumetric temperature measurement target design is imaged by utilizing an infrared camera and the obtained images are processed in electronic environment to form the volumetric temperature distribution. The results that are obtained by 3DMIT method are compared with Stereo Particle Image Velocimetry (SPIV) method. The major benefit of 3DMIT method compared to the other measurement methods is the ability to obtain the temperature distribution simultaneously in three-dimensional form.

1.2 Aim and Motivation

The greatest threat to humanity in the coming period will be itself, the population growth. Yuval Harari summarizes the history of humanity and tells its growth, in his book sapiens:

Over the past five hundred years, we have witnessed an unprecedented rise in human domination. In the year 1500 there were some 500 million homo sapiens in the world. Today, this number is exactly 7 billion. The total value of goods and services produced by people in the year 1500 was about 250 billion dollars today, today the annual production is about 60 trillion dollars. In 1500, people consume 13 trillion calories per day, today's energy consumption is 1500 trillion calories per day. (Be aware of these figures, although the population of people has increased 14 times, production has increased 240 times and energy consumption has increased 115 times.)(Harari, 2016, s. 247).

As these numbers taken in the consideration, the productivity of humanity increased nearly 17 times, although energy consumption for the unit production is decreased 42.92 %. In this point of view we can say the energy efficiency of human kind increased. However, this is not enough because the population and the consumption also increases.

The Global Foot Print organization declared that by August 2, 2017, world population have consumed more from nature than our planet can renew in the whole year. This date is called “Earth Overshoot Date” and it was December 21 at 1971 (<http://www.overshootday.org/>). These data show that we are quickly consuming our planet which is the only place we can survive in the whole universe yet.

Therefore, we must find ways to design less energy consuming high performance systems.

In this study, visual experimental methods enhanced and used for investigation for the fan driven flow fields. By the use of these techniques, the flow characteristics of the devices were revealed in detail. Then the data obtained from these experiments were used to improve the design of the related system.

CHAPTER TWO

METHODOLOGY

“Without data you’re just another person with an opinion.”

These words of Dr. W. Edwards Deming show the importance of gathering data for investigation of all the subjects related to engineering, medicine, physics, economics and even social sciences.

The quality and the dimension of the gathered data is also important. In conventional experimental methods on aerodynamic and thermal engineering focuses on measuring data at a pointwise single location. These approaches give general understanding of systems. However, sometimes they are not sufficient for optimizing complex systems. Whole field investigation methods have advantages in this sense.

In this chapter, the experimental methods which used for gathering multi-dimensional data for investigation of the fan driven flow fields were explained in detail.

2.1 Particle Image Velocimetry

PIV is a flow visualisation method which can be used for both qualitative and quantitative measurements, unlike conventional visualisation techniques. For this purpose, the flow is seeded with tracer particles that can move coherently with the flow and can reflect light.

When these particles pass the area of interest, they are illuminated with a high power light source, generally a laser, by creating a light sheet for imaging with PIV cameras. Although recently, high power Light-Emitting Diodes (LEDs) are used for this illumination, lasers are still most commonly used for this purpose due to their ability to create light sheets more practically. Figure 2.1 shows the positions of the laser, the prototype and the cameras.

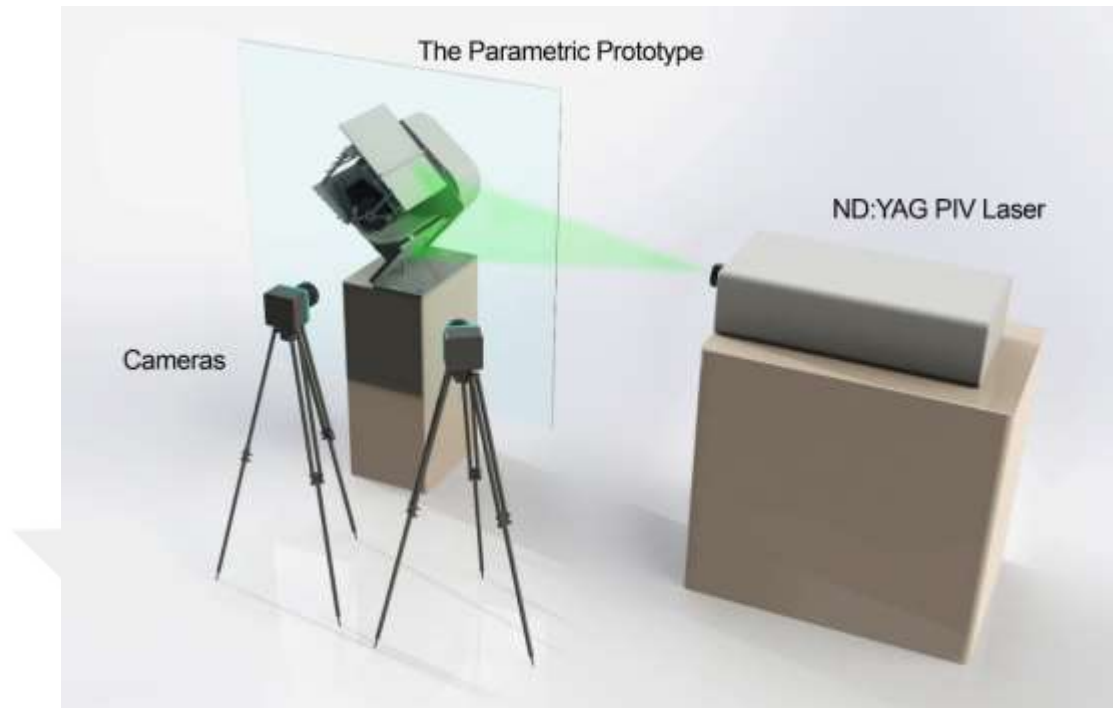


Figure 2.1 The 3D model of the orientation of cameras, laser and prototype

Light sheets are needed because the cameras capture two dimensional projections of three dimensional spaces. Therefore, conventional PIV measurements are performed on a plane (which is created by light sheet), which makes it easier to locate the positions of the particles. This can also be explained mathematically in that a camera creates two dimensional data, therefore, three dimensional data cannot be measured with one camera. For measuring a third component of the velocity, an extra camera can be placed at a different angle to gain two more inputs so that three dimensional data can be obtained. The PIV method that utilises two cameras with separate viewing angles to extract the z-axis displacement called SPIV. In this method, two cameras must be focused on the same plane in the flow area. Therefore, a calibration target is placed at the investigation plane and both cameras focused at this target. Then, images of the target are taken by both cameras as part of the calibration process. These images are used to create a relationship between the 2D pixel dimension of the cameras and the 3D real dimensions. This process also has the advantage of correcting any geometric distortions associated with the imaging processes.

After completing calibration, the experiment can take place. During the experiment, two images are taken rapidly as a couple. The positions of the particles in these images are compared using cross correlation. The cross correlation provides the pixel displacement of the particles in two images. Next, the calibration data are used to obtain real displacements from the pixel displacements. The real displacement is divided by the time between the two images to determine the velocity data.

2.1.1 Particle Image Velocimetry Experiment System Components

PIV is an experiment system consisting a couple of sub systems. The components of the system are: Particle generator and particles, high speed camera, laser, synchronizer, software required to process the data and a computer. An example of PIV system is provided in Figure 2.2.

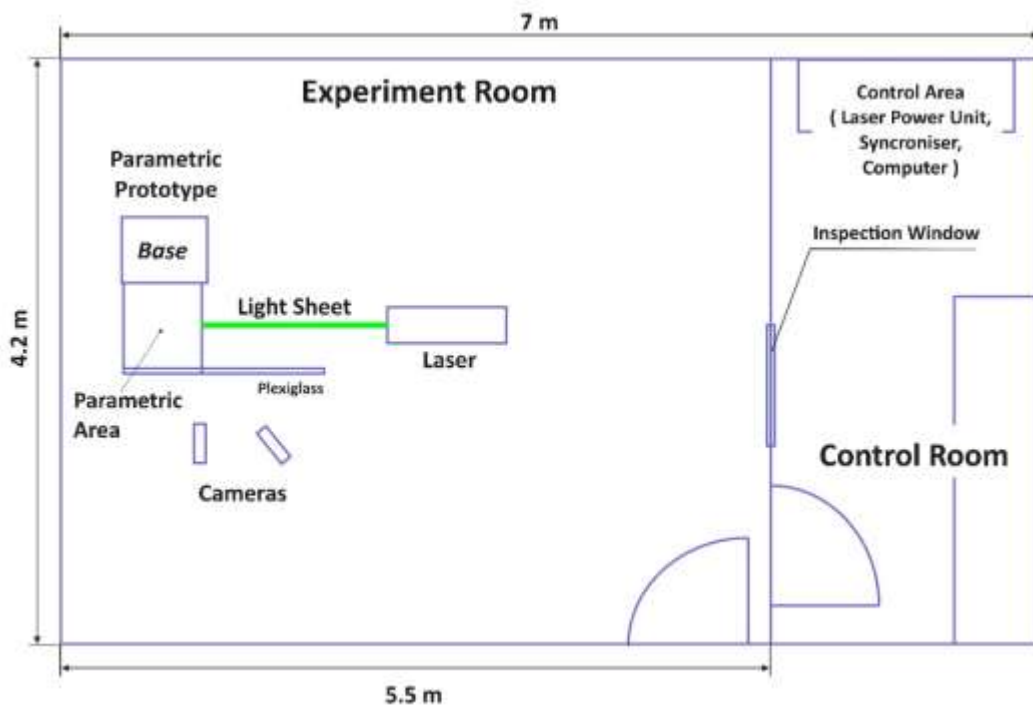


Figure 2.2 The schematic of the experiment room

In many PIV methods, the flow is being "seeded" for investigation. These particles shall be small not to impede the flow characteristics. A fume that consists small particles (one tenth of μm) named as mist or oil sprays with similar size is used for

seeding. Due having a better reflection rate to the mist, oil provides better results and can be used with weaker lasers, however oil can contaminate the work area and can damage the system that is investigated. Rarely, the particles naturally consisted within the flow may be used in PIV.

The flow with the added particles are routed through the experiment apparatus and through the monitoring section. The monitoring section is imaged by illuminating twice in very short intermissions by utilizing Nd:YAG laser. The time frame between the illuminations are related to the velocity of the particle and the area being viewed by the camera. The reason for utilizing laser is to enable an illumination that is strong enough to illuminate the particles at μm size. As the particles get smaller by size and the area being viewed increase, a stronger laser is required.

The particles illuminated by the laser can be imaged on one frame or two separate frames of a high resolution camera. The particles, due to "cross-correlation" process that is applied on the images on the image or if there are two images, on the images, are identified and their displacement between the two illumination moments is observed.

The imaging is done on the whole viewing area. Thanks to CCDs (Charge Couple Device) of today, it is possible to obtain up to a thousand images at 15 MPx and even higher resolutions. If CMOS (Complementary Metal Oxide Semiconductor) is utilized, that is faster than CCD, may provide a lower resolution, however an increased speed.

Following a PIV experiment, a high amount of data (image) is obtained. In order to evaluate mentioned data a thorough investigation (Post Processing) shall be done.

2.1.1.1 Two pulse ND:YAG Laser

Laser provides the high intensity illumination that is required for the camera to capture an image in PIV applications. In close up shots, in order the particles that have a very small reflection surface on the cross sections where the high speed flow is,

adequate amount of light must be provided to the camera sensor. This can only be done with a high amount of light.

Laser means Light Amplification by Stimulated Emission of Radiation. Electrons that are stimulated to a high energy level radiate a photon to discharge the energy difference as they go down from a high level of energy to a lower level of energy, and this normally occurs with radiation. However during this change in energy level, if an electron interacts with a photon, the radiation of the electron (i.e. other photons) shall be at the same orientation and phase of the photon collided with the electron. This is named as "Stimulated Emission" and lasers work with this principle (Figure 2.3).

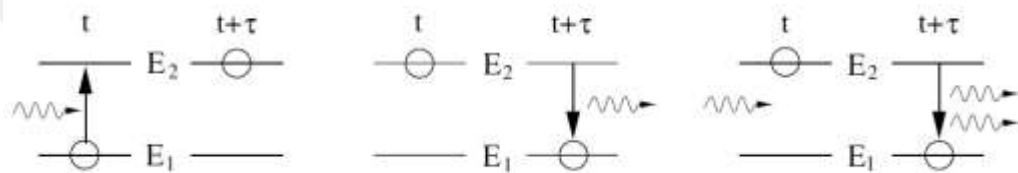


Figure 2.3 Elementary kinds of interactions between atoms and electromagnetic radiation, a) Absorbing, b) Spontaneous Emission, c) Stimulated Emission (Raffel, Willert, Wereley, & Kompenhans, 2007)

Lasers generally are named after their medium that allow the radiation. The laser that is used as a radiation material in our study is "Neodymium-Doped Yttrium Aluminum Garnet" and is named as ND:YAG (Figure 2.4). Due to the fact that the material that allows laser radiation (yttrium aluminum garnet) is solid, this is classified as solid state laser. During utilization the change in the temperature or chemical composition of the laser crystal may deteriorate the quality of the beam. In applications such as PIV that requires a high frequency and high energy laser, the reason for utilizing this particular laser is having a good thermal and chemical properties.

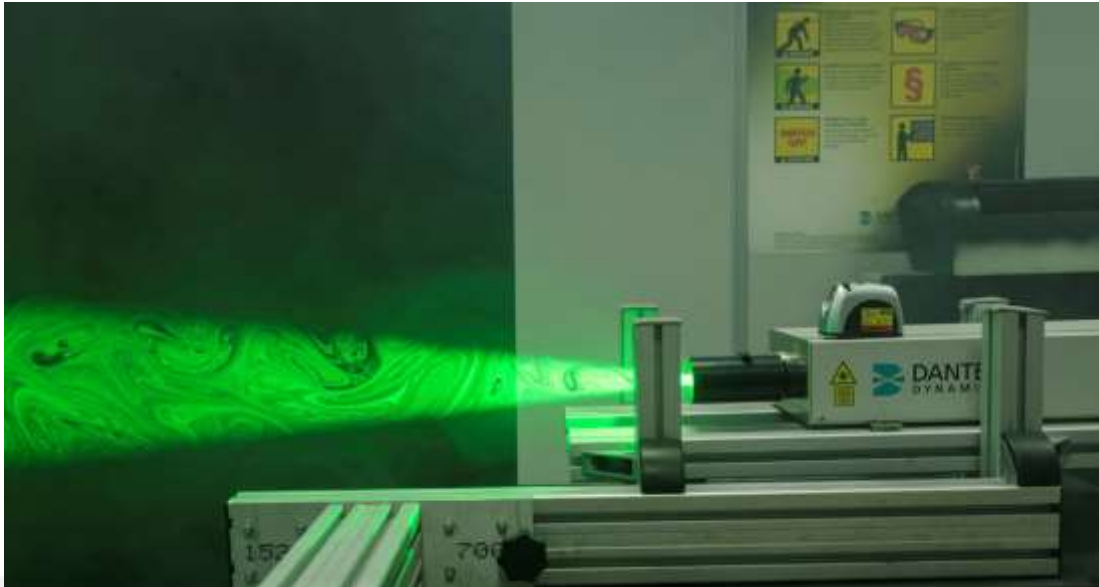


Figure 2.4 Photo of the current laser (Personal archive, 2017)

The wavelength of the light generated by ND:YAG laser is 1064 nm. This light is in the infrared range and cannot be seen. However, by the use of double oscillator system, the wavelength is sent as two separate 532 nm waves and turned visible. This property is critical in order to obtain an image couple in cross sections with high velocity flow. PIV applications can be utilized with the continuous illumination lasers that do not include this double pulse feature, however due to high illumination (and in relation high energy) requirements, the continuous laser energy consumption can go up to mega-watts and results in very high operation costs. Furthermore, it is harder to cool down the laser during operation. The double pulse of the lasers and the progress in computer technologies are the fundamental driving reasons behind the progress and widespread usage of PIV systems.

2.1.1.2 Particle Image Velocimetry Camera

PIV Cameras are devices that when a lens that allows the light to beam through in a uniform manner, record the image via a sensor, CCD (Charge Couple Device) or CMOS (Complementary Metal Oxide Semi Conductor) within the device. This device works with a similar principle of the standard cameras that are used daily, however PIV cameras include superior features such as snapshot or sequential shots (Figure 2.5).



Figure 2.5 Photo of the current cameras (Personal archive, 2017)

Exposure time in photography is the duration that the sensor (Film or a Sensor) being exposed to the light. This timeframe influences the photograph in two aspects. The timeframe adjusts the amount of light that falls on the sensor based on the space where the light goes through (aperture), furthermore during the timeframe where the light falls on the film, the fixed items are seen clearly, the moving particles are seen with a Motion Blur. The exposure is also referred as "snapshot".

The snapshot and the timeframe between two exposures are critical for PIV image recording. In an event that the photograph is captured with a longer exposure duration in relation to the velocity of the particles (i.e. with a slower snapshot), the particles will be viewed as moving (not clear- blurry). This would result in incorrect vectors in resolving the image.

Another important point is the timeframe between two exposures. For images captured sequentially that is faster than required, the particles would not be able to move at required distance and due to the fact that the difference between two images would not be clear, the velocity vectors would not be able to be calculated. On the other hand if the interval between two exposures is too long, some of the particles in

the first photograph (in extreme cases all of them) will be out of the exposure area and would not be able to be captured in the second photograph. If this is the case, in cross correlation the computer would not be able to process the particles in two photographs or would process them incorrectly.

Based on this information, in order to capture images of the particles in high flow velocities in align with the PIV system, image capturing at a very high speed is required. Furthermore, to successfully conduct the Cross Correlation, an additional image should be captured within a very short timeframe. A standard camera can only capture images with 1/8000 s exposure duration and 1/20 s intervals. PIV cameras on the other hand are capable to capture images on very fast instances (very short exposure durations) such as 1/6,250,000 s and able to save an additional frame within nano seconds. Therefore in PIV systems where the flow reaches very high speeds, the image pairs used for processing can be obtained.

2.1.1.3 Synchronizer

This equipment is utilized in order to ensure the synchronized initiation of the camera and the laser. This system is specifically required at high speeds. In an event that the image capturing at nano seconds and illumination is not synchronized, the images will be black without any illumination.

2.1.1.4 Particles and Mist Generator (Seeder)

Seeding is the process that adds particles with high light reflection features to the flow. These particles move within the flow and allows the imaging of the flow components and processing. Particles' ability to adapt to the flow and having a high light reflection ability are the two features that the selected particles should provide for adequate seeding of the experiment apparatus.

The ability of the particles for light reflection is closely related to the choice of laser that will be utilized. If an image is captured where the seeded flow is not adequately

illuminated, changing the particles instead of the laser will be a more affordable solution. The reflection ability of the particles are the function of the size of the particles, shape orientation and the rate of refraction index of the particles to the environment refraction index.

When the difference of refraction indices of the liquids and gases are reviewed, it is seen that illuminating a particle in a gas is relatively easy and illuminating a particle in a liquid is relatively harder, for this reason, by utilizing particles with a larger size (10-1000 μm) and compensating the loss in refraction index by gaining in reflection surface, on the other hand since the gases have a suitable refraction index, particles with a smaller size (0.5 - 10 μm) may be used. In certain cases utilizing larger particles in gases and smaller particles in liquids may be preferred.

The light reflection feature is not solely enough. In an event where the size or the density of the particles are more than required, the particles would not be able to move in align with the flow and since the velocity of the particles are measured in PIV, inaccurate velocity data would be obtained. This phenomenon is referred as velocity delay. For this reason, even though there are issues regarding the refraction index in liquids, due to the density and the size of large particles are more suited to be used in liquids, it is relatively easy to experiment on liquids. Although in investigating gas flows there is an advantage regarding the refraction index, due to the fact that the particles that are in align with the gas flow are too small, better results are obtained with a stronger laser and cameras with higher image density. At this point the size and the density of the particles are relatively more important than the ability to reflect light. As a result, a particle that has an inferior reflection ability may be made visible by stronger illumination, however measurements with particles that are not compatible with the flow, the measurements will be inaccurate.

Another problem resulting from selection of a particle with unsuitable density is the conglomeration of the particles at a certain section of the flow in environments with circular flow due to centrifuge effect. If this is the case, investigation would not be possible due to having no particles at a certain section of the flow and having a higher

conglomeration of particles at a certain section of the flow. There are three different particle imaging densities and each has a niche utilization (Figure 2.6).

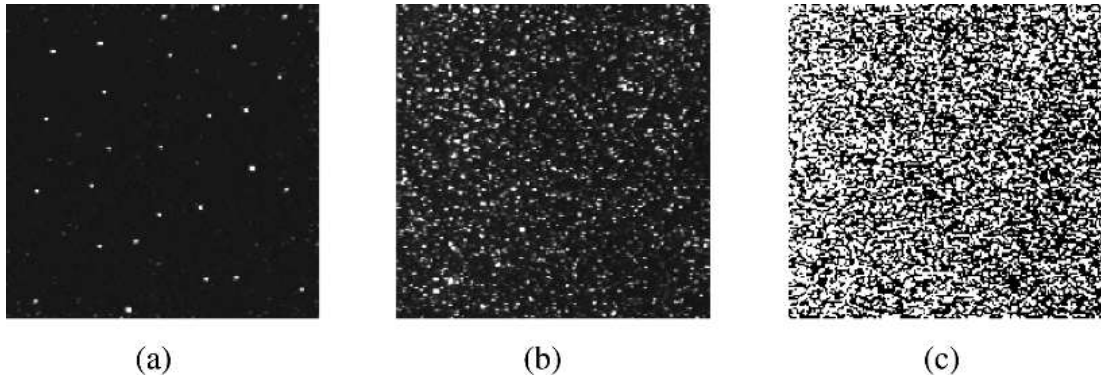


Figure 2.6 Particle distribution images (Raffel, Willert, Wereley, & Kompenhans, 2007)

a) Low imaging density: This is used in "Particle Tracing Velocimetry" method. In this method the identification of the particles in two images are easy. For this reason it is a suitable method for determining the particle velocity. However due to the lower density translates to covering a smaller section of the flow area and as a result the measurement will not be able to identify the flow.

b) Medium imaging density: This rate of density is the most suitable for utilizing the PIV system. Matching the particles in the first image to the particles in the second image are estimated via correlation methods. On the other hand the frequency of the particles are adequate for investigating the flow.

c) High Imaging Density: This system was utilized in the beginning of the 19th century. Due to the fact that identification of the particles were not possible, it is successful up to a limited level for determining the flow areas, however the determination of the particle velocity is not possible. Can only provide qualitative data.

In addition to accurate selection of the particle, by including adequate amount of particle in the flow and establishing the adequate density of particles is required. In our current study, mist is being used as particles and seed generator is being used, as shown in Figure 2.7.



Figure 2.7 Photo of the current seed generator (Personal archive, 2017)

2.1.1.5 Computer and Software

Following capturing the images, the last phase of the process is obtaining the velocity vectors by comparing the images on the computer.

In order to obtain the velocity vectors, the first image is divided into investigation areas. Following this phase, cross correlation is conducted with the second image. The maximum value of the cross correlation would show on which section of the second image the particles in the first image best match and therefore the section where the particles are most likely to be. The vector between the section in the first image where the particles are and the location of the particles in the second image is the displacement vector of the fluid. The exposure interval between the two frames is known, therefore the speed vector is calculated by dividing the displacement vector with the mentioned interval.

2.1.2 Obtaining Volumetric Average Flow Data by Stereo Particle Image Velocimetry

As mentioned in previous chapters, in the PIV method, the experimental setup has to be designed according to the system and flow area to be investigated. Studies in the literature show that a plane of symmetry, which is assumed to best describe the system, is examined. However, in engineering-aerodynamic applications, only a part of the flow field may not be sufficient in terms of system development. Basically the advantage of PIV is that the entire flow cross section can be examined at the same time. In order to better appreciate this present advantage, a method for creating "volumetric three-dimensional average velocity vectors" has been developed by the current project group in previous studies.

An application of this method on SAC Outdoor unit is given as an example.

In order to obtain "volumetric three-dimensional average velocity vectors", the system needs to be examined at certain intervals. The device is placed in a traverse system so that the device can be properly traversed at these intervals. One of the cameras is positioned vertically so that the flow generated by the device can be viewed. The second camera positioned angled to the light sheet so that the third flow component can be investigated. The laser is positioned to vertically to the device so the light sheet is vertical to the first camera. The mentioned test setup is given in Figure 2.8.

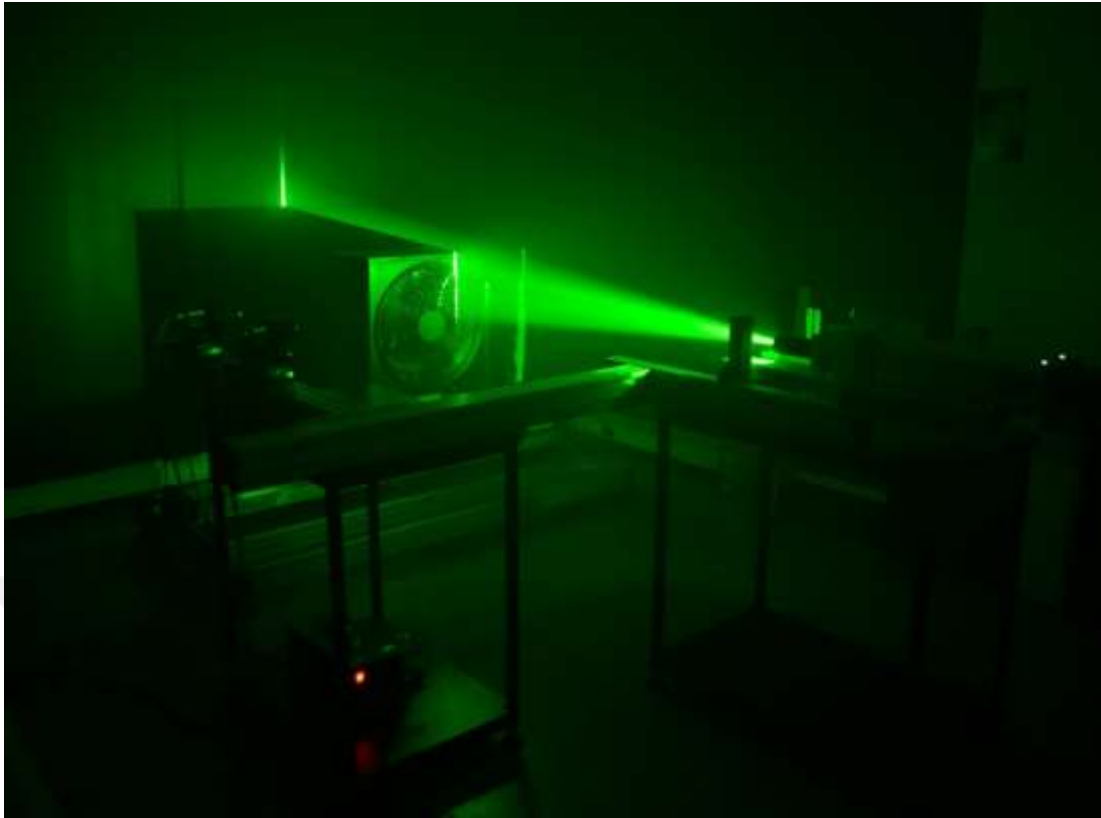


Figure 2.8 Outdoor unit SPIV setup (Personal archive, 2014)

Another consideration when looking at Figure 2.8 is that the height of the outer unit is considerably larger than the inner unit. This causes both the laser to not illuminate the whole system at the same time and not to see the entire system in terms of the cameras angle of view. In terms of resolution of this situation, the cameras and laser can be retracted further. In this case, however, both the reason for the diminished light flux and the particles not being sufficiently illuminated may arise, and the examination area is more roughly examined by the reason for the decrease in the number of pixels per unit area.

As a solution to this situation, it has been decided to carry out scanning in two axes. Therefore, the lower part of the fan is scanned with 30 planes, then the same planes are scanned in the upper part of the fan. In order to avoid errors in position, a traverse system with a precision of one-tenth of a millimeter is used. The locations of the scanned regions are shown in Figure 2.9.

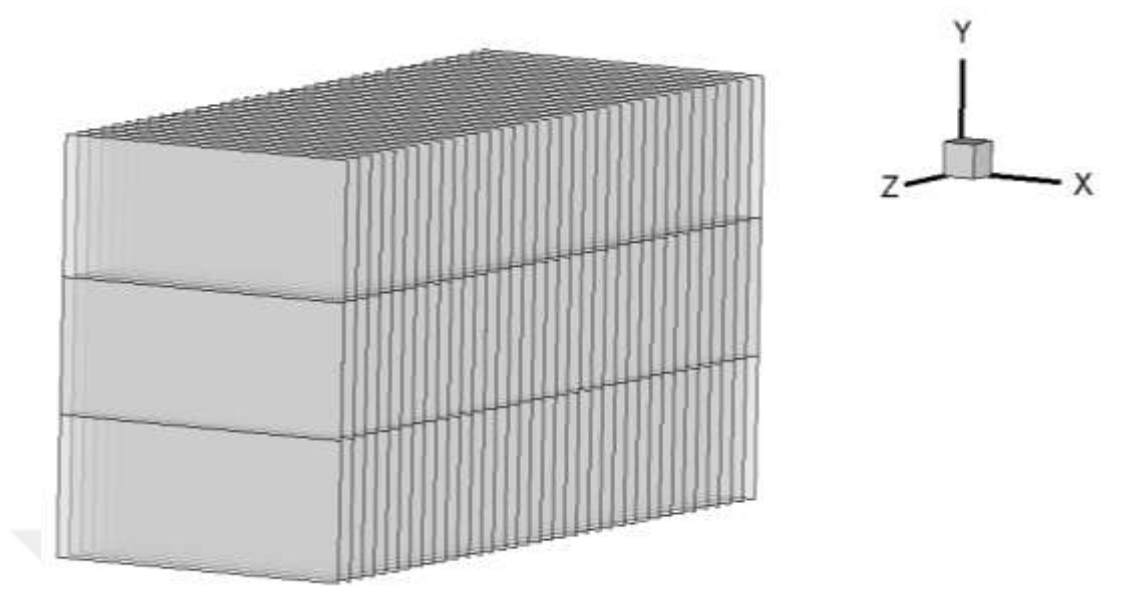


Figure 2.9 Positions of the examination planes measured in the PIV experiments for examining the volumetric flow distributions of the external units

Each of these locations was examined using a stereo PIV with a dual camera. Images were taken to form 200 vector mappings from each plane. Then, the mean velocity vectors were obtained by the mean of these instantaneous distribution vectors. An example of the obtained average velocity vector map is given in Figure 2.10.

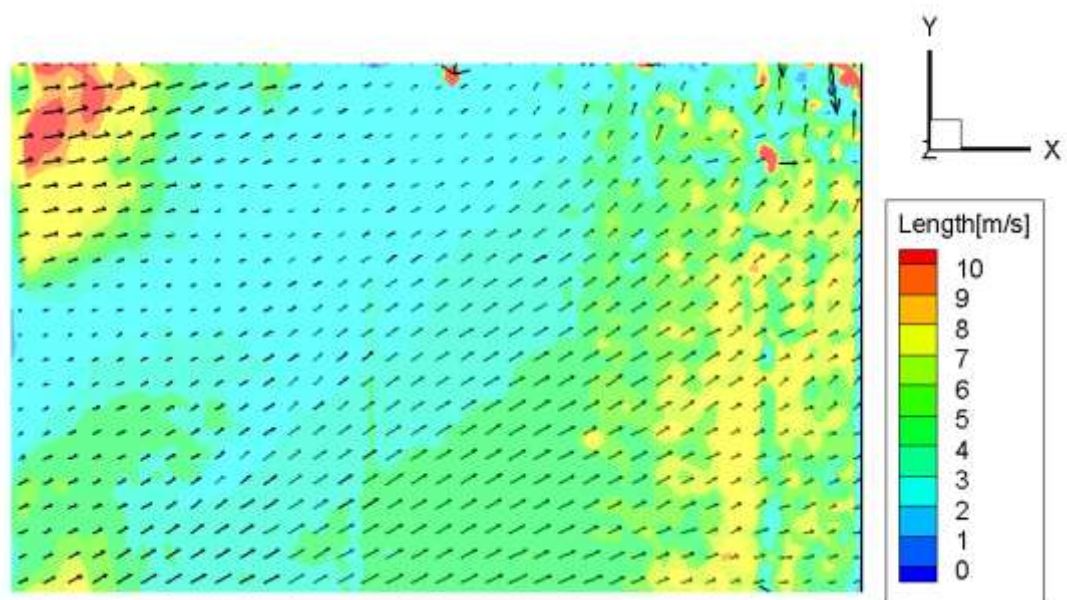


Figure 2.10 Planar mean velocity distribution map obtained from the stereo PIV of the upper scan area of the axial fan of the SAC outdoor unit

The visual in Figure 2.10 is obtained from the top of the air conditioner outdoor unit. Colors are used to express the size of speeds, and vectors are used to express direction. It has been observed that the resultant flow is again directed upward after passing through the nozzle. This orientation is symmetrical about the axis of the fan. In order to better understand these flow structures, the volumetric data from the planar data within obtained.

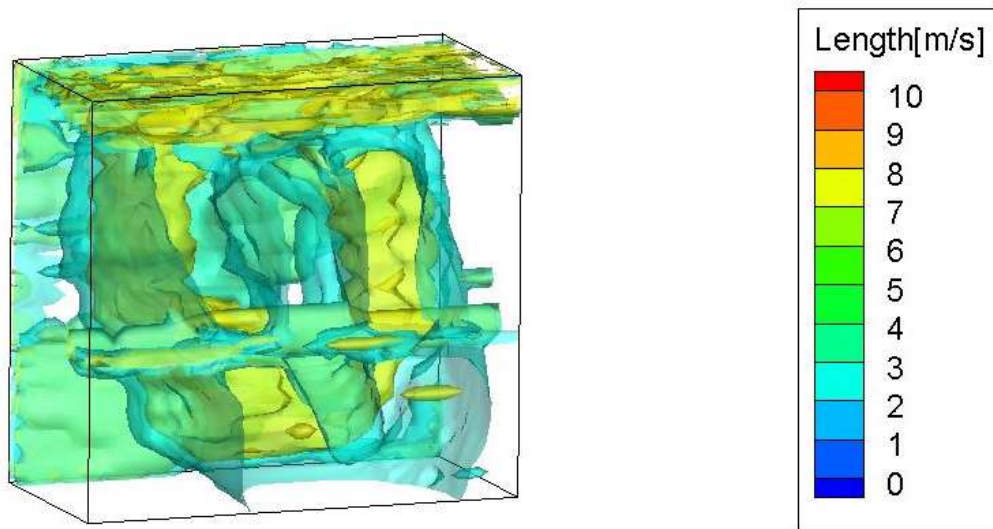


Figure 2.11 Velocity iso-surfaces of the split air conditioning outdoor unit at the blowing zones (3-8 m/s)

The three-dimensional volumetric average flow structure in the obtained blowing zone of the SAC outdoor unit is given in Figure 2.11 as velocity iso-surfaces. The velocity iso-surface at the center represents the jet core that the fan creates (8 m/s). When the map of speed distribution given in Figure 2.12 is examined, it is seen that the jet stream flow over 10 m/s is wrapped with a thin 8 m/s layer. The outer velocity iso-surface (3 m/s) represents the part encountered with static air. Lower velocities appear to fill the edges of the flow field completely, indicating that these velocities are the flow of the environmental air.

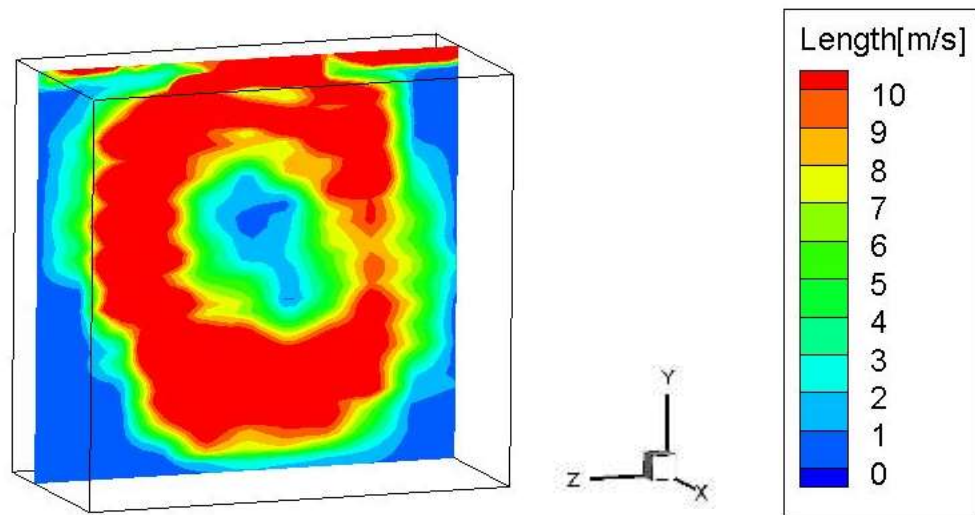


Figure 2.12 Average scalar velocity distribution map of the split air conditioning outdoor unit at the blowing zones

2.2 Three Dimensional Meshed Infrared Thermography

In general, measurement screen methods based on visualizing a solid target by infrared thermography for measuring temperature distribution in gaseous media due to the fact that gas are transparent at infrared wavelength (7-13 μm). Therefore, measurement screen methods are indirect measurement methods and the precision of the measurement is strongly based on the relation between target and flow structure. For a successful measurement, the target should show as similar as temperature distribution with air and it must create minimum distortion on the flow.

Convection is the dominant heat transfer mechanism between the target and the gas. So the target must be designed to enhanced this mechanism and reduce the other heat transfer mechanisms. For example, plane measurement screens have wide surface area which has radiative heat transfer with surrounding. These screens also have conductive heat transfer among itself. So the temperature distribution obtained from a plane measurement screen is function of convection with investigated gas, radiation with surrounding, conduction among screen. Therefore, obtained temperature distribution from plane screen does not directly represent the temperature distribution of investigated gas. This effect is studied in Chapter 7.

Measurement screens' distortion effects on the flow structure is another important phenomenon that leads deformation on temperature measurement. Naturally, measurement screen that is installed in the flow area would change the flow structure. However, the amount of deformation is critical. If the deformation is too high, it may lead to measure an irrelevant flow structure instead of the aimed one. The measurement screens effects on flow also studied in Chapter 7.

In the current study, a measurement screen with the capability of handling all these effects is designed. This called "Three Dimensional Meshed Infrared Thermography (3D MIT)" method.

In 3D MIT method, there are spheres that are placed on the carrier ropes that are stretched between two parallel plates connected to one another with foot stands. The complete structure formed by these components is named the volumetric temperature measurement target (Figure 2.13).

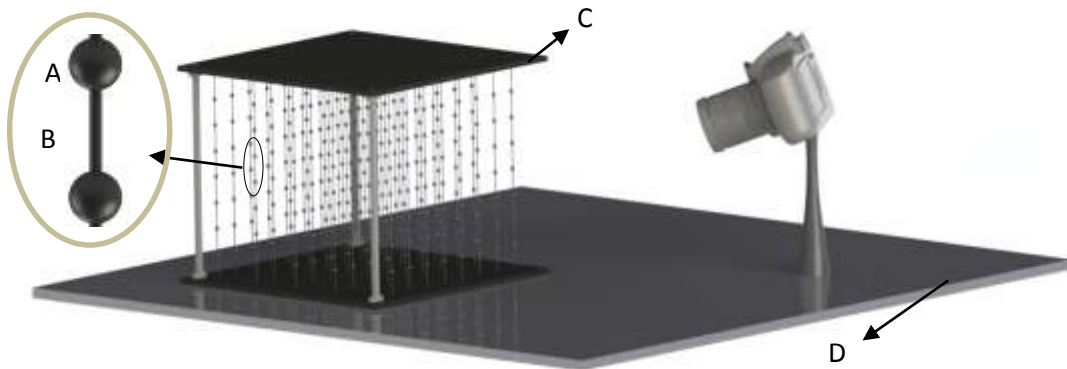


Figure 2.13 Three dimensional meshed infrared thermography setup

Spheres (Area A in Figure 2.13) are positioned on the carrier ropes (Area B in Figure 2.13) which oriented between two parallel plates (Area C in Figure 2.13). As it mentioned earlier, the ropes position is related with the size of the spheres and the velocity of the flow. The important parameters of the carrier ropes are thermal conductivity and diameter of the rope. The thermal conductivity must be as low as possible for preventing conductive heat transfer between the spheres. The diameter

also must be small for reducing flow distortion. However, it must be rigid enough to hold the spheres at a fixed position. Having fixed positions of the spheres will prevent them from flickering while they are exposed to stream and it will also ensure that the image is taken clearly. Additionally, when the spheres locations are fixed and known, the measurement mesh locations at three-dimensional space are also known. So that, the image obtained from the thermal camera is only used for matching and temperature measurement. Thus, 3D measurement can be performed with a single camera.

The plates (Area C in Figure 2.13) and the supporting beams (Area D in Figure 2.13) are the mechanical carriers of the spheres and the ropes. These are skeleton of the system. Their positioning is important in the means of not disturbing of the flow and not visually block the camera.

The most important parameter of the system is the geometry size and location of spheres. The spheres geometry has the advantage of symmetry. The area projected perpendicular to the free stream velocity parameter (A_f) in drag coefficient formula (Equation 2.1) (Incropera, & DeWitt, 1996) does not change for different attack angles. This also means the flow deformation in every attack angle will not be effected by target geometry. The symmetric geometry also has advantage on thermal imaging. Spheres has same view area in all angle of view. Therefore, the spheres are more suitable than plane and porous targets for three dimensional flows and volumetric measurements. All the other parameters used in MIT study is listed at Table 2.1.

$$C_d = \frac{F_d}{A_f(\rho V^2 / 2)} \quad (2.1)$$

Table 2.1 Parameter list of MIT study

C_D = Drag Coefficient CFF
F_D = Drag Force [m]
A_f = Frontal Area [m^2]
ρ = Density of the fluid [kg/m^3]
V = Fluid Velocity [m/s]
L_R = The Displayed Length in the Corresponding Axis in the Image Plane
L_S = Sensor Size at Related Axis
d = The Distance Between Lens and Object Plane
f = Focal Length of Camera Lens [m]
S_f = Scale Factor
$P\#$ = Pixel Number of Camera at Related Axis
$P\#_{sphere}$ = The Number of Pixels Filled with the Spheres at Related Axis
D_{sphere} = Sphere Diameter
N = Aperture number
c = Circle of confusion
s = Focusing distance
D_N = Near focus distance
D_F = Far focus distance
H = Hyper focal Distance
DOF = Depth of field
n = The Minimum Number of Pixels at Related Axis That Should Be Covered by the Measurement Sphere in the Image

The diameter of the spheres is critical parameter for 3D MIT. As the size increase the flow deformation also increases. This affect the location of the following sphere. In an ideal application, it is expected that the flow deformation created by a sphere will damp out before reaching the other sphere. So if the flow deformation increases by the diameter of the spheres or by an increase of the velocity, the spheres must be positioned less frequently. So decreasing diameter of the spheres has an advantage in flow effects. However, it makes the temperature measurement harder. In Figure 2.14, the phenomenon is shown.

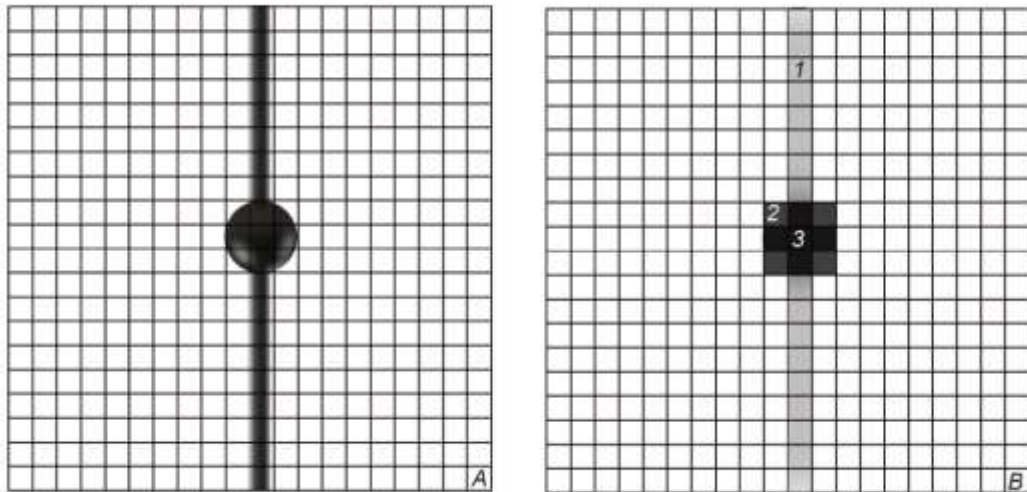


Figure 2.14 a) Target projection on sensor, b) Simulated temperature map

Like normal digital images, infrared images also consist of pixels. The difference is infrared image pixels represent temperature instead of light intensity or color data. Figure 2.14-a shows the projection of the image on the sensor. Figure 2.14-b shows simulated temperature map. For a precise temperature measurement, a pixel must be filled by the target surface like the pixel-3 shown in Figure 2.14-b. The pixel-3 only gathers data from target surface. Otherwise, the pixel would measure area weighted average of the target and the background. The pixel-1 and pixel-2 in Figure 2.14-b can be examples of this phenomena. For obtaining the target temperature, subpixel algorithms must be used in these situations. “n” is the minimum number of pixels at related axis that should be covered by the measurement sphere in the image. The number n must be chosen that at least one pixel in the image is filled by the sphere. It is advisable that this number is 3 or greater when it is considered that in a real thermal image all spheres are not centered by pixels. This creates a relation among the sphere size, the resolution of the image, the sensor size and the focal length of the lens. The geometrical relations of these parameters are shown in Figure 2.15 and the mathematical relations of these parameters are given in Equation 2.2, 2.3 and 2.4.

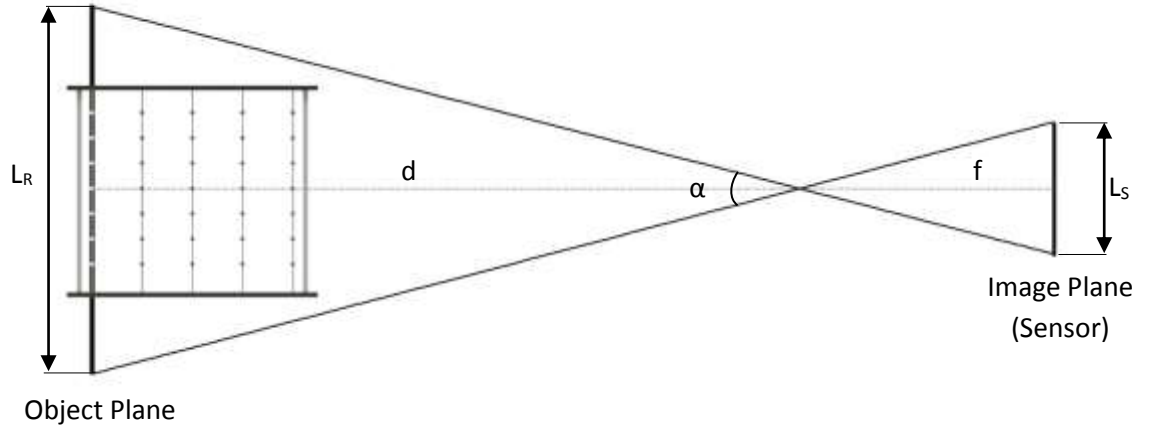


Figure 2.15 Optical schematic of 3D MIT setup

$$\frac{L_R}{d} = \frac{L_S}{f} \quad (2.2)$$

$$S_f = \frac{L_R}{P\#} = \frac{D_{sphere}}{P\#_{sphere}} \quad (2.3)$$

$$d = \frac{D_{sphere} P\#}{P\#_{sphere} L_S} f \quad (P\#_{sphere} \geq n) \quad (2.4)$$

The area of a pixel that correspond in the object plane is defined as scale factor (S_f) and it depends on the focal length of the lens (f), the size of the sensor (L_S), pixel number of camera at related axis ($P\#$) and the distance between the camera and the object plane (d). The focal length of the lens and the size of the sensor also determine the angle of view (AOV) (α) of the lens.

These equations can be used for determining the size of the investigation volume, size of the investigations spheres according to the camera and lens specifications. However, the distance between the camera and the object plane is also related with depth of field.

The lenses focus the light that comes from a certain distance due to their working principle. This is called focusing distance (s) and the objects at these distances are imaged at the maximum sharpness which allowed by the lens. As the objects move away (or closer) from this distance, the area scattered in the image plane of the light

coming from a single point expands. The diameter of this scatter area which does not allow to be visually observed or does not harm the technical process is called the permissible diameter of the circle of confusion (COC). To sum up, the region which is close enough to the focusing distances that the diameter of the point source light's scattered area is smaller than COC are considered as focused and this region is called the depth of field. Formulas related to the depth of field are given in Equations 2.5, 2.6, 2.7 and 2.8.

$$H = \frac{f^2}{N \cdot c} + f \quad (2.5)$$

$$D_N = \frac{H \cdot s}{H + s} \quad (2.6)$$

$$D_F = \frac{H \cdot s}{H - s} \quad (2.7)$$

$$DOF = \frac{2H \cdot s^2}{H^2 - s^2} \quad (2.8)$$

Lack of focusing (blurriness) in terms of thermal imaging means that temperature information from different points intermingle and cause the measured temperature to be incorrect. So, COC should be as small as possible from a pixel size of the sensor in order to minimize this situation.

The aperture number (N) and focal length (f) parameters are not configurable in most of the thermal cameras. Therefore, the focusing distance (s) is the main adjustable parameter for arranging the depth of field which the 3D MIT target must fit in. As a result, it is checked whether the distance between lens and object plane (d) obtained from Equation 4 is compatible with the calculation of the depth of field (DOF) in Equation 8.

As the final result of these, the spheres shall be at a size small enough to minimize the flow distortion and large enough to be captured by the infrared camera. The location and the size of the spheres selected to satisfy both needs.

2.2.1 Validation

A comparison experiment was performed using thermocouples to validate the temperatures obtained by the 3D MIT method. In this experiment, 3D MIT target was placed at an exit of a CFF that drives hot air. The exit dimensions of the CFF were 185x40 mm. Thermocouples were placed beside 5 of measurement spheres. Validation points were positioned on a straight line which goes through the center of the fan exit area perpendicularly. The distance between the validation points was 30 mm. Temperature measurement was performed with thermocouples and 3D MIT method simultaneously. The linear regression fitting between the 3D MIT and thermocouple measurement were given in Figure 2.16.

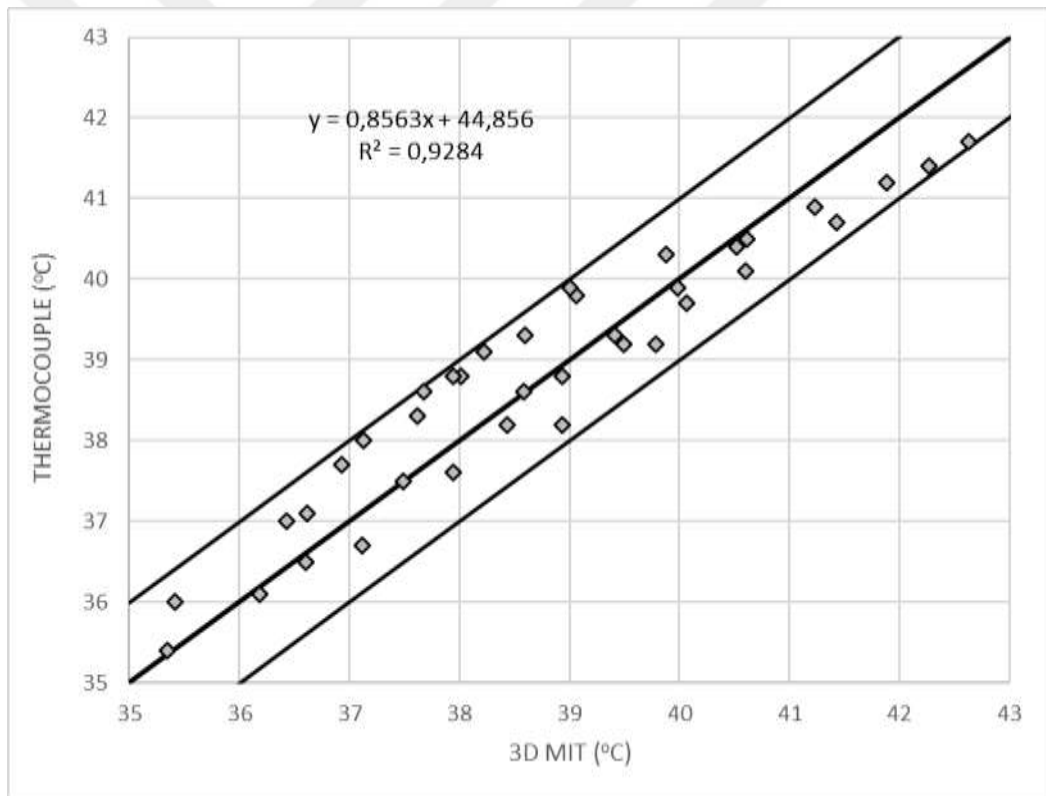


Figure 2.16 Linear regression fitting between validation experiments

When all data in Figure 2.15 were examined, it was determined that the maximum error is less than 1 K. The absolute difference values between thermocouples and 3D MIT vary between 0.01-0.93 °C. The average difference between two experiments is

0.06 °C. The standard deviation of the absolute differences for whole measurement nodes is 0.3 °C.

When the results were evaluated, it was seen that 3D MIT results are coherent with the thermocouple measurements. This shows 3D MIT method is useful for both measuring and visualizing the temperature distribution. The comparison of this method with alternative methods is given in the chapter 7 and the advantage of measurement is revealed once more.



CHAPTER THREE
EXPERIMENTAL INVESTIGATION ON CROSS FLOW FAN'S CASING
PARAMETERS INSIDE OF A SPLIT AIR CONDITIONER INDOOR UNIT
BY STEREO PARTICLE IMAGE VELOCIMETRY

The methodology applied in this part of the study consists of three main phases. In the first phase, the investigation parameters of CFF were decided according to the literature survey which was shared in the previous section. For this investigation an experimental air conditioner prototype which is called parametric prototype was built which has the capability of changing orientations of the components. Detailed information on the parametric prototype is given in Section 3.1.

In the second phase of the study, the parametric prototype was studied by SPIV method. In these experiments, two dimensional three component (2D3C) velocity maps of 480 different design combinations were obtained at the outlet of the device. Detailed information on the SPIV method is given in Section 3.2.

When the number of experiments is taken in to consideration, it is very difficult to visually evaluate all the obtained velocity maps. For this reason, PIV data were transformed into dimensionless parameters that were previously determined in the third phase of the study. Detailed information on these parameters and their transformation is presented in Section 3.3.

In addition to all these, validation tests (Section 3.4) were carried out to check the reproducibility of the experiments. In addition, the full prototype of the design point that have the best performance has been produced and compared with a full prototype of a design point with average performance (Section 3.3).

The parameters used in this part of the study is given as table 3.1.

Table 3.1 The parameters list of chapter three

D_1 = Internal diameter of the CFF [m]
D_2 = External diameter of the CFF [m]
L = Length of the fan [m]
n = Number of rotation per minute
s = Maximum blade thickness [m]
β_1 = Internal blade angle of CFF [$^\circ$]
β_2 = External blade angle of CFF [$^\circ$]
γ = Blade stagger angle [$^\circ$]
e_R = radial distance between impeller and rear wall [m]
e_V = radial distance between impeller and vortex wall [m]
α_0 = angle between the beginning of the casing rear wall and the horizontal axis of the impeller [$^\circ$]
Ω = Exit angle [$^\circ$]
H = Height of the outlet [m]
S = Length of the vortex wall [m]
ρ = Density of the fluid [kg/m^3]
P_t = Total Pressure of the fluid [Pa]
u_2 = Linear velocity of the outer tip of the fan blade [m/s]
Φ = Flow coefficient
Ψ_t = Total pressure coefficient
q_v = Air flow rate
$q_{\text{projected}}$ = Projected air flow rate
RE_{Blade} = Reynolds number of the blade

3.1 The Parametric Prototype of the Split Air Conditioner Indoor Unit and Investigated Parameters

As stated, part unlike axial fans, the CFF's ability to drive air is strongly based on its casing. However, all these components are inside the closed cavity of the SAC. This is not suitable for a regular PIV measurement, which needs optical access. Therefore, in this study, a cut off parametric prototype was designed to grant the required optical

access. The prototype has the ability to change the casing parameters for investigating the effects on the flow characteristics. A 3D model of the parametric prototype is given in Figure 3.1.

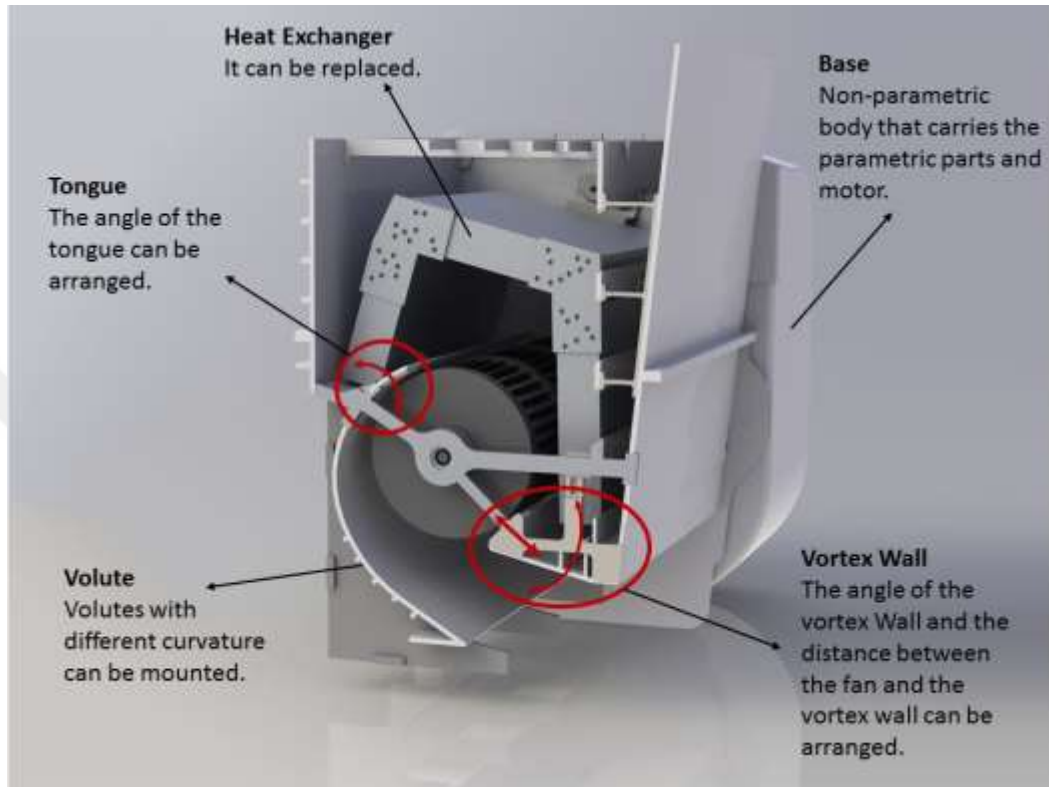


Figure 3.1 The parametric prototype of the SAC indoor unit

The parametric prototype consists of two main parts: the base and the parametric part. The base is a strong rigid component on which the replaceable parts of the prototype are mounted. The base includes the motor and the driver card for rotating the fan at the desired frequency. The fan is connected to the motor by the drive shaft. The bearing on the other side of the fan shaft is chosen as a parametric part of the prototype. The parametric part also consists of the tongue, the vortex wall and the rear wall, which are parametrically adjustable.

In Figure 3.1 shows the tongue area. The tongue is an extension of the volute that can be angled to alter the flow structure. The parametric prototype was designed to test five different tongue angles. The tongue angle that is positioned as a natural extension of the volute curve is accepted as the angle of origin and is referenced as 0. By

increasing and decreasing the angle of the tongue by 7.5 degree increments, four different tongue positions are created. The tongue position with + 15 degrees represents the closest point to the heat exchanger, whereas the tongue position with - 15 degrees represents the closest point to the fan. The tongue cannot be increased or decreased past these limits due to geometric constrictions of the components, i.e., if the tongue angle is increased further than 15 degrees from its natural position, it would come into contact with the heat exchanger. However, if the negative tongue angle exceeds -15 degrees, the tongue will come into contact fan, restricting the fan rotation.

Two separate parameters of the vortex wall were reviewed, which is shown in figure 3.1 and in Figure 3.2, area C. The first parameter reviewed is the vortex wall angle. The angle shifts in 5 degree increments at four different positions, +5, 0, -5 and -10 degrees, respectively. The second parameter of the vortex wall represents the distance between the fan and the vortex wall, namely the vortex wall – fan difference, which are 0.02 D, 0.04 D and 0.06 D. The variable D is the diameter of the fan.

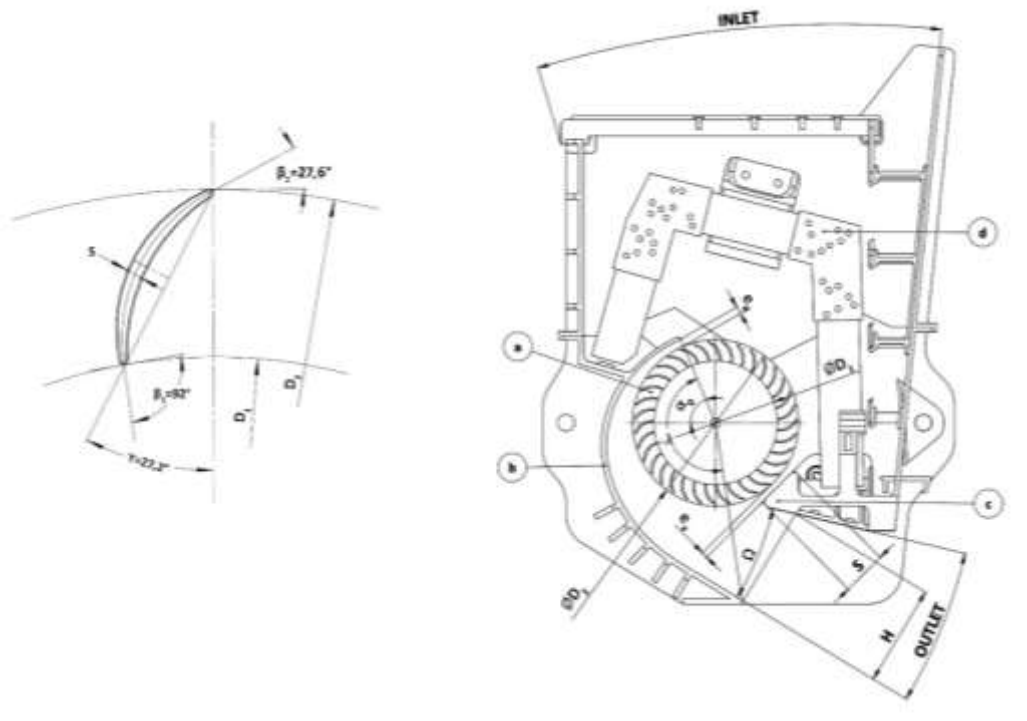


Figure 3.2 The schematic the blade parameter and the SAC

The third and the last area shown in the Figures 3.1 and 3.2 (Area b) is the volute. Four different volute curvatures were investigated in this study. The first curvature, which is widely implemented in commercial applications, is included as a reference design. The remaining three curvatures are specifically designed for this study.

The volutes can be designed with different curvatures, such as sections of hyperboles, parabolas, ellipse and spirals. In this study, different derivatives of logarithmic spirals were implemented for designing the volute curvatures. The progression ratios used in creating these spirals are 1.4, 1.618 and 1.8. The value of 1.618 is selected specifically instead of 1.6 to implement the golden ratio. The reason behind implementing the golden ratio, which was widely preferred by selected artists, engineers and scientists throughout history, is to observe its effects on the flow structure. This also highlights another unique aspect of this study.

The last parameter investigated in this study is the heat exchanger. The heat exchanger itself comprises of many different design parameters, such as the number and position of pipes, the distance between the fins, the fin thickness, component materials, etc. For the purposes of this study, the varying parameters of the heat exchanger were not included, as the amount of experiments required would increase significantly. However, to observe the heat exchanger's influence on the flow field, we impose a binary variable: existent and non-existent heat exchangers.

The complete parameter list with design points is provided in Table 3.2. In total, 480 different experiments were conducted using the design points and parameters.

Table 3.2 List of the investigated parameters and the total number of experiments

Parameter Name	Number of Design Points	
Tongue Angle	5 Positions	$-15^{\circ} \sim +15^{\circ}$
Vortex Wall - Fan Distance	3 Positions	$0.02D \sim 0.06D$
Vortex Wall Angle	4 Positions	$-10^{\circ} \sim +5^{\circ}$
Volute Curve	4 Designs	
Heat Exchanger	Exist/Not Exist	
Total Number of Experiments	480	

The rotor parameters were fixed. These are direct design parameters of the rotating part of the fan, such as number of blades, diameter of the fan, blade cord length and curvature of the blades, etc. The blade parameters are shown in Figure 3.2 and the values of these parameters for the selected fan are given in Table 3.3.

Table 3.3 The rotor parameters

The Name Of The Parameter	Value
Number of blades	35
Blade cord length (c)	14 mm
Fan outer diameter (D_2)	100 mm
Blade stagger angle (γ)	27.2°
Blade angles	$\beta_1 = 92^{\circ}, \beta_2 = 27.6^{\circ}$

The rotation frequency of the fan was also accepted as a rotor parameter and it was excluded from the investigated parameter. 1100 rpm was used for all the experiments. The rotation frequency was checked by a laser tachometer.

The blade Reynolds number is calculated using Equation 3.1. The variable u_2 is the linear velocity of the outer tip of the fan blade, which can be calculated from Equation 3.2. Using both equations, we see that all the parameters that affect the Reynolds number are constant. Therefore, the Reynolds number used for all the experiments in this study is 5075.

$$Re_{Blade} = \frac{u_2 c}{\nu} \quad (3.1)$$

$$u_2 = \frac{D_2 \pi n}{60} \quad (3.2)$$

3.2 Stereo Particle Image Velocimetry Parameters of the Study

In the current study, a 15 Hz, 135 mJ double pulse ND:YAG laser was used to illuminate the particles. Two 4 MP cameras are used for SPIV setup. The time between pulses for image couples was selected to be 40 μ s. For every prototype, 800 images were taken by two cameras to generate 200 two dimensional, three-component vector maps.

In the data processing stage, the Dynamic Studio Version 3.41.38 software is used on the complete experiment sets to determine average correlation and adaptive correlation methods. The interrogation areas were selected as 32x32 pixels with 50% overlap. Following this step, using vector maps from both cameras and the calibration data acquired prior the experimentation process, the SPIV results were obtained.

3.3 Output Parameters

Although PIV can generate great amounts of visual data, due to difficulties in providing each comprehensive visual experiment result in this paper, these results are reviewed via three numerical output parameters.

The first parameter is the total pressure coefficient (Ψ_t). This parameter significantly affects the jet penetration of the steady air volume and is a significant factor for the air conditioner blowing range. The formula for this parameter is given in Equation 3.3, where P_t is the total pressure of the fluid and ρ is the density of the fluid.

$$\Psi_t = \frac{P_t}{\frac{1}{2}\rho u_2^2} \quad (3.3)$$

The air volume channelled through the device may also influence its performance. Therefore, the flow coefficient (Φ) is used as the second parameter. The flow coefficient is calculated from Equation 3.4.

$$\phi = \frac{q_v}{LD_2 u_2} \quad (3.4)$$

In Equation 3.3, q_v is the flow rate of the device, and L is the length of the fan, which is determined by the manufacturer and is proportional to the device's size and capacity. However, as mentioned, the prototype designed for these experiments is a cut of model, which allows a measurement of velocity on a symmetrical plane. This means that it does not allow a measurement of the full air flow rate. Therefore, a projected air flow rate ($Q_{projected}$) is calculated from the measured velocity data using Equation 3.5, where L is maintained at 1 meter.

$$q_{Projected} = V_{Av} \times H \times L \times C_C \quad (3.5)$$

In equation 3.4, H [m] represents the height of the channel, which is the distance between the upper border and the volute at the selected section, as shown in figure 3.1, where V_{av} [m/s] is the average velocity at the selected section H . The correction factor is represented by C_C . As indicated, the PIV are measured on a symmetrical plane where the jet stream is strongest. However, the jet stream cannot be maintained for the entire length of the channel due to environmental air resistance. To generate a more accurate projection, C_C is applied to Equation 3.4 to account for the loss of the air flow rate, which is especially significant on the edges of the jet stream. For this reason, C_C cannot

have a value higher than 1. Because the value of C_C is unknown at the early stages of the study, this value was assumed to be 1. However, at the end of the study, a real life prototype was manufactured with an optimum design derived from the parametric prototype. A value for C_C was calculated by evaluating the both results.

The third and final output parameter is vorticity, which is defined as the degree of local spinning motion. A high vorticity is an indication of two outcomes: the first being that a certain amount of the mechanical energy transferred to the air by the fan is wasted in creating unwanted spinning motion, which also results an increase noise created by the device. The same cross section is used to calculate the aforementioned parameters.

3.4 Results

As indicated in methodology chapter, the flow fields in 480 design points were investigated by SPIV and the data processing stage accomplished. In Figure 3.3, in order to comparing four different parameters eight sample average correlations were shown. Design Point 160 is the prototype that have the best performance and was selected as the reference design. The other design points were given for comparison and only one parameter is different than the reference Design Point. In design point 326, the varying parameter is the volute design. The Design Points 140 and 150 shows change in the vortex wall angle, Design Points 157 and 158 compares tongue angle and Design Point 205 and 250 compares vortex wall distance. The input parameters of these experiments are given in table 3.4.

The vectors on Figure 3.3 represent the velocities in the measurement plane and black and white areas at the background represent the out of plane flows. White areas shows +z which is towards the reader and the black areas shows the opposite.

For more general consideration, Figure 3.4 shows the dimensionless results of all the design points. The expected huge effects of the heat exchanger on flow coefficient and the pressure coefficient can be seen in Figure 3.4-a.

Table 3.4 Input parameters of the experiments that are given at Figure 3.3

Investigated Parameters				
Experiment Index No. (Design Point)	160	326	140	150
Volute Progression Rate	1.618	1.4	1.618	1.618
Vortex Wall Angle [°]	-5	-5	5	-5
Vortex Wall-Fan Distance	0.04 D	0.04 D	0.04 D	0.04 D
Tongue Angle [°]	7.5	7.5	7.5	7.5
Investigated Parameters				
Experiment Index No. (Design Point)	157	158	205	250
Volute Progression Rate	1.618	1.618	1.618	1.618
Vortex Wall Angle [°]	-5	-5	-5	-5
Vortex Wall-Fan Distance	0.04 D	0.04 D	0.02 D	0.06 D
Tongue Angle [°]	-15	+15	7.5	7.5

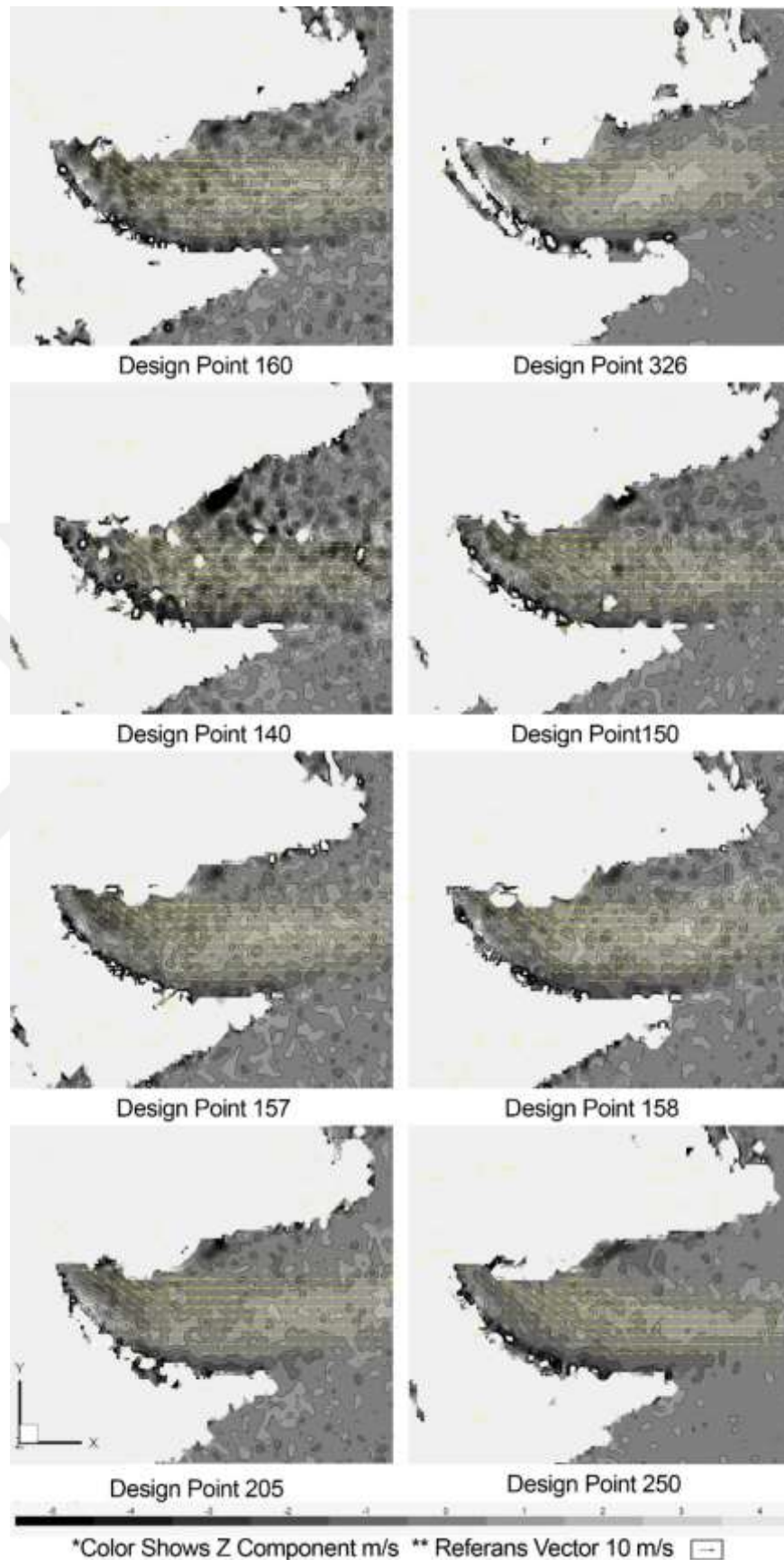


Figure 3.3 Averaged two dimensional three component flow structures of selected design points

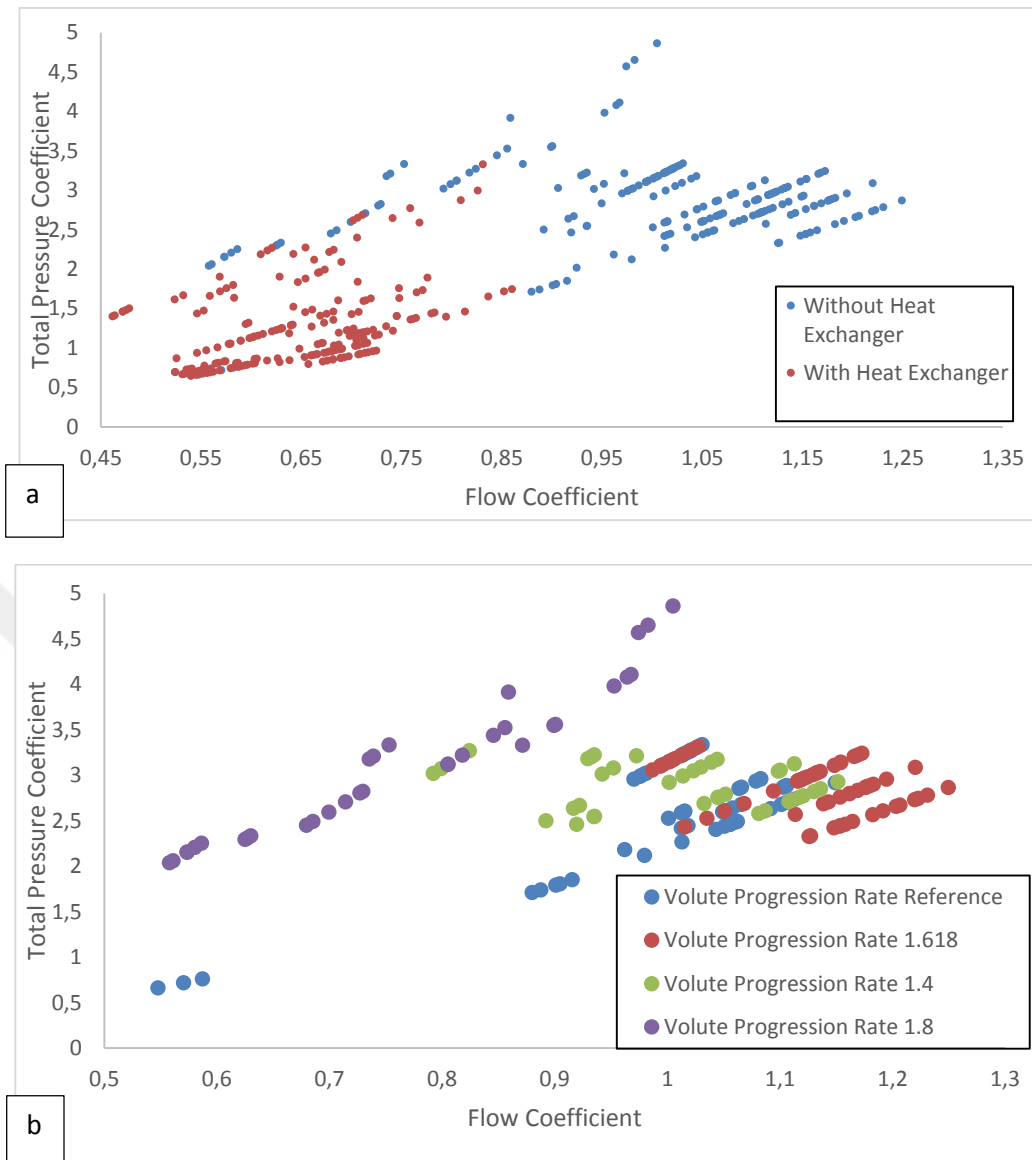


Figure 3.4 Total pressure coefficient-Flow coefficient graphs

a- Total pressure coefficient-Flow coefficient graph of all experiment, grouped according to heat exchanger.

b- Total pressure coefficient-Flow coefficient graph of experiments without heat exchanger grouped according volute curvature.

c- Total pressure coefficient-Flow coefficient graph of experiments without heat exchanger grouped according tongue angle.

d- Total pressure coefficient-Flow coefficient graph of experiments without heat exchanger grouped according vortex wall distance.

e- Total pressure coefficient-Flow coefficient graph of experiments without heat exchanger grouped according vortex wall angle.

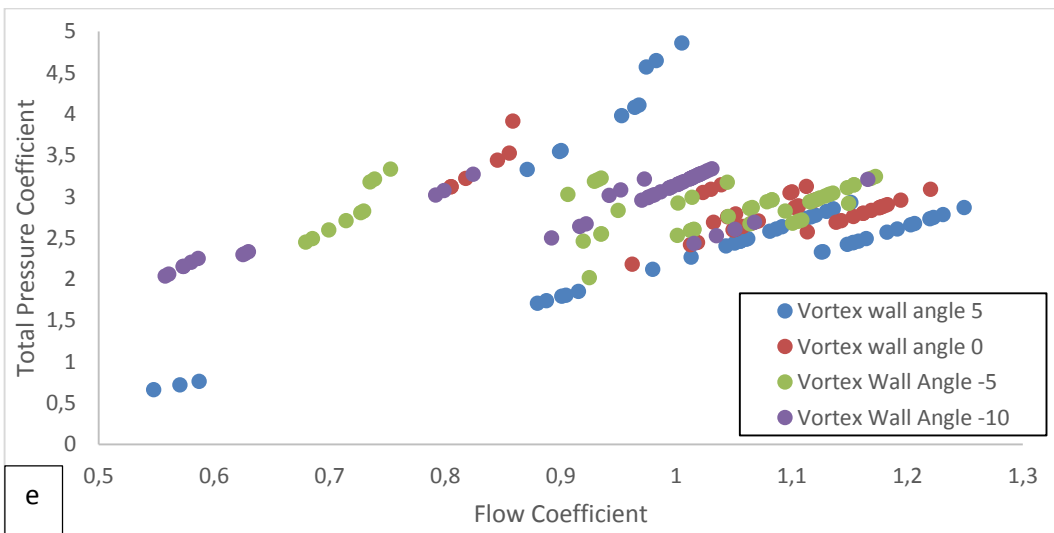
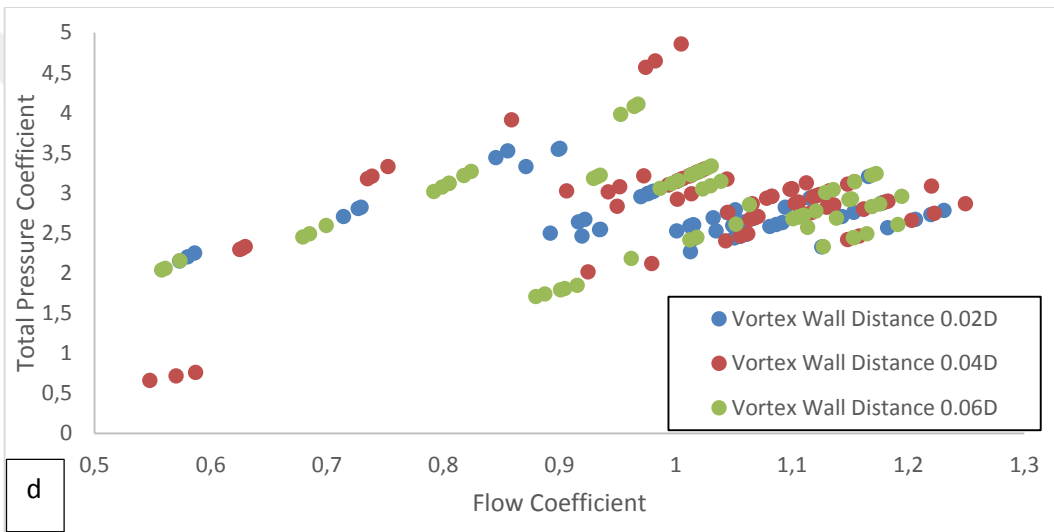
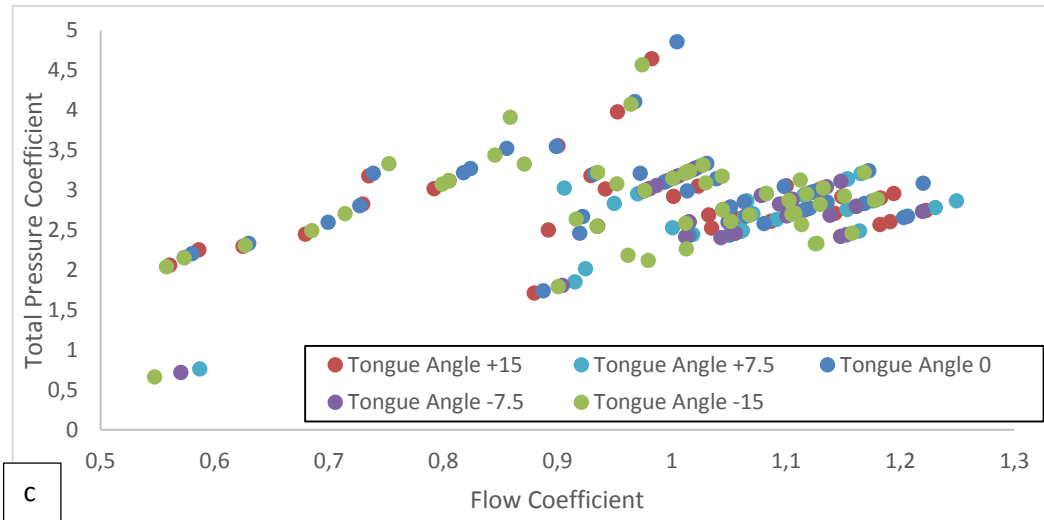


Figure 3.4 continues

When Figure 3.4 is examined in general, it is seen that while the strong parameters are trending (Figures 3.4-b and 3.4-e), the less effective parameters are distributed to fit these trends (Figures 3.4-c and 3.4-d). As an example, the volute curvature parameter (volute progression rate) shown in Figure 3.4-b is very similar to the curve of the system characteristic curve. All the data related to this parameter is not on the same curve because of the effects of flow coefficient and total pressure coefficient of other effective parameters. The individual effects of the parameters discussed at the following parts of this study.

3.4.1 Individual Parameter Effect on Split Air Conditioners Flow Structure

At the beginning of the evaluation stage, the effects of the individual parameters on the SAC flow structure were reviewed to determine if a single parameter has any effect on the performance. To achieve this, the experiments were categorised and averaged based on the investigated parameter, as shown in Table 3.5. The values given in Table 3.5 are the averages of the same parameter. As an example, the Average Flow coefficient of a Tongue angle of -15 degrees is the average of all the experiments for the same tongue angle.

Table 3.5 Averaged results of the parametric experiments

Parameter Name	Parameter Value	Average Flow coefficient of Total Experiments	Average Pressure Coefficient of Total Experiments	Average Vorticity of Total Experiments
Tongue Angle (°)	-15	0.990	2.849	0.9317
	-7.5	0.976	2.874	0.9240
	0	0.972	2.905	0.9173
	7.5	0.971	2.850	0.9084
	15	0.971	2.800	0.8996
Vortex Wall Angle (°)	5	1.039	2.579	0.9467
	0	1.040	2.863	0.8975
	-5	0.997	2.858	0.9345
	-10	0.919	2.899	0.8719
Vortex Wall Distance To The Fan	0.02 D	1.003	2,730	1.0010
	0.04 D	1,016	2,863	0.8823
	0.06 D	1,016	2,805	0.8562
Volute Curvature *	**	1.011	2.602	0.8801
	1.4	0.766	3.341	1.007
	1.618	1.127	2.858	0.888
	1.8	1.006	2.891	0.937

* The progression ratios of logarithmic spirals

** The volute curvature of a commercial SAC. The data is gathered for the comparison.

3.4.1.1 The Effect of Tongue Angle

The first parameter investigated is the tongue angle, as shown in Figure 3.3 and Table 3.4. As the tongue converges to -15 degrees, the flow and total pressure coefficients converge to their minimum values due to the tongue narrowing in the suction area of the fan. However, as the tongue position converges to the natural position from -15 degrees, the fan operates in a less restricted manner, which in turn causes the air velocity to increase slightly. Nevertheless, the projected air flow rate does not increase significantly due to the tongue still blocking the air flow area to a certain extent.

As the tongue is positioned towards +15 degrees, the fact that the tongue does not obstruct the fan suction causes the air flow coefficient to increase slightly. Table 3.5 shows that the overall vorticity does not fluctuate significantly. Therefore, as Table 3.4 and Figure 3.4-c are reviewed, we see that the tongue position itself does not significantly influence the overall performance.

3.4.1.2 The Effect of Vortex Wall Angle

The second parameter investigated is the vortex wall angle (Figure 3.4-e and Table 3.5). As specified, as the vortex wall angle is altered from – to + degrees, the channel height increases. Therefore, at -10 degrees when the channel height is at its minimum, the velocity is high. However, due to pressure losses, both the flow and total pressure coefficients are relatively low. As the angle of the vortex wall increases, the channel height is increases. As a result, the pressure loss decreases and the flow rate increases. When the vortex wall is positioned at 0 degrees, the flow coefficient converges to its maximum value. However, the total pressure coefficient slightly decreases. As the angle continues to increase (+5) due to the channel height exceeding the optimum height, the total pressure greatly decreases and the vorticity increases. In the final analysis of the parameter, we see that an optimum angle of the vortex wall exists that can provide a maximum velocity and flow rate. These effects also can be seen by comparing design point 140,150 and 160 in Figure 3.3.

3.4.1.3 The Effect of Vortex Wall Distance

The third parameter is the vortex wall distance and is provided in Table 3.5 & Figure 3.4-d. As the data shows within the given investigation range, the distance between the vortex wall and the fan does not influence the overall output parameters at a significant level. However, we note that as the distance between the vortex wall and the fan decreases, the vorticity increases significantly, as seen in Table 3.5, which is an indication that the air noise has increased. This phenomenon was also observed during the experiments. Some noise level measurements were conducted.

3.4.1.4 The Effect of Volute Curvature

The fourth parameter is the volute curvature. As the jet stream follows the volute, it influences the performance output parameters to a high degree. It effects the flow rate coefficient by 32.03% (Table 3.5). As mentioned, three different progression ratios were used to design the volutes that were formed via the logarithmic spirals.

Among the three, 1.4 is the first ratio investigated. As the progression rate converges to 1, the channel height decreases. Therefore, the 1.4 progression rate creates the narrowest flow channel, which results an increase in the velocity and vorticity, whereas the projected flow rate decreases due to the pressure loss.

The second investigated volute was designed using the golden spiral form. The projected air flow rate increased significantly, but a relatively small decrease was observed in the velocity. The vorticity also decreased, which is an indication that a steady air flow was maintained.

When the 1.8 ratio was observed, the velocity was maintained at a steady level compared to the golden ratio. However, the projected air flow rate decreased at a relatively high level, whereas an approximately 10% increase in vorticity was observed.

When these three ratios were compared, we see that the golden ratio provides superior results in terms of the overall performance parameters. These effects also can be seen by comparing design point 160 and 326 in Figure 3.3.

3.4.1.5 The Effect of Heat Exchanger

The last individual parameter observed is the presence of the heat exchanger.

During the design process of SACs, a common method utilised is to design a CFF that has a high performance and then integrating the fan into the SAC unit. It is a widely accepted assumption that a high performing CFF without a heat exchanger installed will maintain its high performance in a design including a heat exchanger. To investigate this, as a parameter, the inclusion of a heat exchanger was added to the scope of this study.

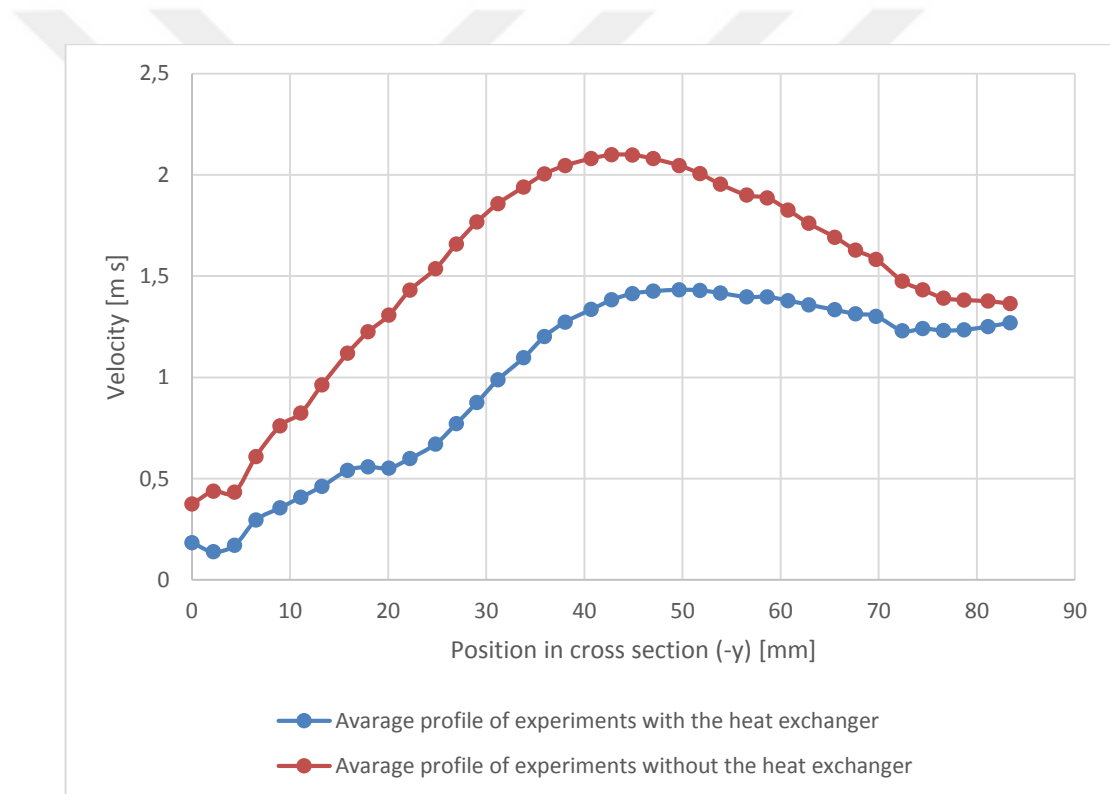


Figure 3.5 Comparison of the average flow profiles in scenarios with and without the heat exchanger

However, as indicated, the heat exchanger inherits a high number of design parameters. For this reason, the effects of the heat exchanger individual parameters on the flow structure are not investigated in this study. Figure 3.5 shows the average flow profiles with and without the inclusion of the heat exchanger. Figure 3.2 shows the reference point of the profile selected at the top side of the cross section. Over the first condition where the heat exchanger is installed within the SAC, the jet stream follows

the volute closely and the average velocity is 50% less compared to the other scenario due to regulation and pressure loss effects associated with the heat exchanger. This result shows that the heat exchanger not only influences the average velocity but also influences the flow profile.

Another factor to consider is the condensate that forms between the fins when the heat exchanger is operating in cooling mode. In classical design methods, the condensation is regarded as an additional pressure drop to the pressure drop created by the heat exchanger. However, the inhomogeneous occurrence of this condensate in certain regions of the heat exchanger can also affect the flow profile. Therefore, designing casing parameters according to this phenomenon may lead to better performing SACs. The present experimental setup does not allow to investigate this situation. However, this effect is planned to be examined in further studies.

3.4.2 The Overall Effect of Investigated Parameters on Split Air Conditioner's Flow Structure

Previously, the parameters' effects on the overall performance were investigated individually. To this end, the average of all the experiments for an individual parameter was taken into consideration.

In this study, the overall effects of the aforementioned parameters were investigated as a whole in an individual experiment. To this end, the experiments that provide the best projected air flow rate were selected for comparison. For the selected experiments, the results including the best case scenarios with a heat exchanger and a best case scenario without a heat exchanger are compared. This also created an opportunity to test the assumption provided in the previous chapter that states that “a high performing CFF without a heat exchanger installed, will maintain its high performance in a design that a heat exchanger is included”. The results of the selected experiments are provided in Table 3.6.

Table 3.6 The comparison of the best case scenarios with and without the heat exchanger

Investigated Parameters				
Experiment Index No. (Design Point)	135	140	155	160
Volute Progression Rate	1.618	1.618	1.618	1.618
Vortex Wall Angle [°]	5	5	-5	-5
Vortex Wall-Fan Distance	0.04 D	0.04 D	0.04 D	0.04 D
Tongue Angle [°]	7.5	7.5	7.5	7.5
Heat Exchanger	0	1	0	1
Output Parameters				
Average Velocity [m/s]	9.737	5.651	10.192	6.616
Projected Air Flow Rate [m³/hr]	2586.242	1500.885	2388.565	1620.832
Vorticity	1.211423	0.712994	0.827988	0.772473

Experiment Index No. 135 represents the best projected air flow rate without a heat exchanger installed, whereas experiment Index No. 140 is the comparison experiment with a heat exchanger installed. Naturally, if the assumption stated before was correct, Experiment No. 140 should provide the best results among the experimental set with a heat exchanger installed. However, we observe that experiment No. 160 provides the best results among the experimental sets with a heat exchanger installed. Experiment

No. 155 includes the same parameter set as Experiment No. 160 without a heat exchanger installed to prove that Experiment No. 135 provides the best results among the experimental sets that does not include a heat exchanger.

Another differing parameter, besides the presence of the heat exchanger, is the vortex wall angle. Among the compared sets, for scenarios without a heat exchanger, the flow rate increases since there is no additional pressure drop due to the heat exchanger. Therefore, at its highest vortex wall position, better results are observed.

For the scenarios with a heat exchanger installed, the air flow rate decreases. Therefore, at a vortex wall angle of +5 degrees, the channel that is created is too wide to drive the jet stream. In order to compensate, the vortex wall angle is positioned at -5 degrees to obtain the best results when using a heat exchanger.

In an event that a conventional test was used instead of the current parametric prototype and PIV method to determine the optimum design, the heat exchanger version from Experiment No. 135, which is Experiment No. 140, would be selected for mass production. However, this approach would result in an inferior product with an 18.29% loss in velocity and a 7.5% loss in projected air flow rate compared to Experiment No. 160. This also indicates that the aforementioned assumption may not be applicable to all design variants in the recent state of the industry.

3.4.3 Investigation and Experimental Validation on Full Model

Following the completion of the parametric tests, Experiment No. 160 is selected as the design that provides the best flow rate with the highest velocity and lowest vorticity for manufacturing the full prototype. The manufactured prototype went through a full scale PIV test. In this test, 36 equal spaced measurement planes were selected throughout the SAC outflow channel and two dimensional three component velocity maps were obtained for each measurement plane via the SPIV method. The gathered data planes are placed sequentially within a three dimensional space in a virtual environment and interpolated to form the average three dimensional flow field

of the SAC. Figure 3.6 shows the gathered flow profiles as velocity iso-surfaces. The innermost iso-surface represents a velocity of 7 m/s, indicating the jet core, the outermost iso-surface (with a velocity of 3 m/s), which is the contact surface of the jet and the stationary air, and the iso-surface between them, which represents a velocity of 5 m/s. As seen in Figure 3.6, a two peak flow structure is observed at the jet core, which was also observed in preceding studies. We also observed that the overall flow structure is persistent and stable. For details regarding the applied method and the flow structure, see the Chapter 2.

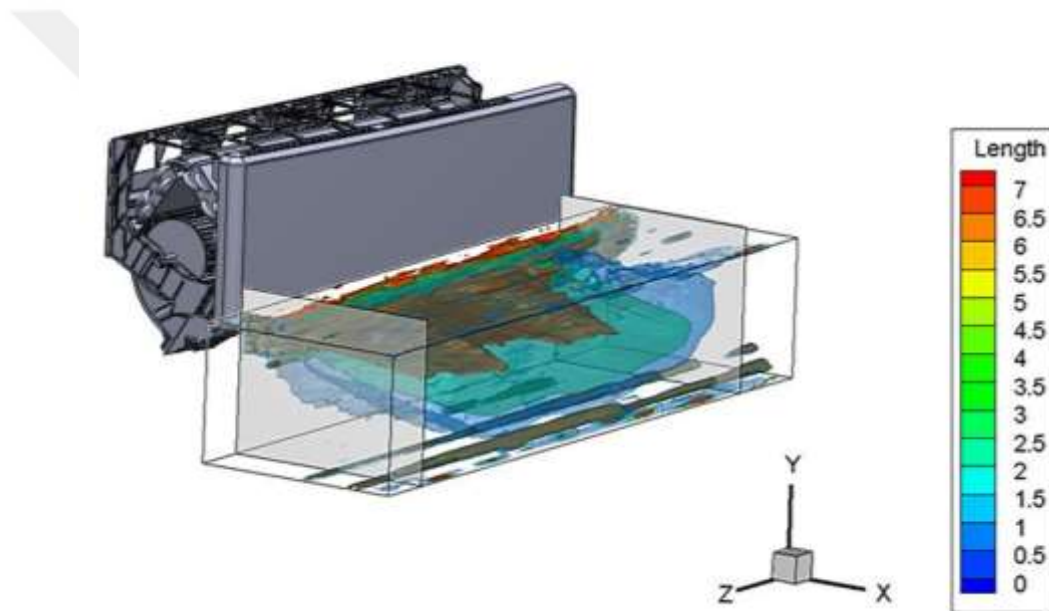


Figure 3.6 Average volumetric velocity iso-surfaces at the outflow area of the SAC prototype, selected based on the results of the parametric study

In addition to the PIV experiments performed, the device was subjected to flow rate and sound tests. The obtained data were used in the calculation of the correction factor and in the verification of the sound predictions.

3.4.3.1 Calculation of the Correction Factor

To calculate the Correction Factor, we used Equation 5 and measured the flow rate in a standard test room with the full prototype to arrive at 1195 m³/h. To this end, the

projected air flow rate calculated in Experiment No. 160 was recalculated as 1337,19 m³/h, according to the manufactured prototype channel length of 0.825 m, which was assumed to be 1 m in the initial stages of the study. From this result, the Correction Factor (C_c) is calculated to be 0.894.

3.4.3.2 The Effects on Noise

The noise sources of SACs, can be examined in two groups. These are mechanical noises which are caused by the motor, shaft, bearing... etc. and aeroacoustics noises that are caused by the turbulent fluid motion or aerodynamic forces interacting with surfaces. There is also two ways to prevent the aeroacoustics noise which also partially subject of current study. One of these is to prevent the sound from spreading by methods such as coating and texturing done on the surfaces, and the other one is to prevent the formation of sound by reducing the irregularities and vorticity in the flow.

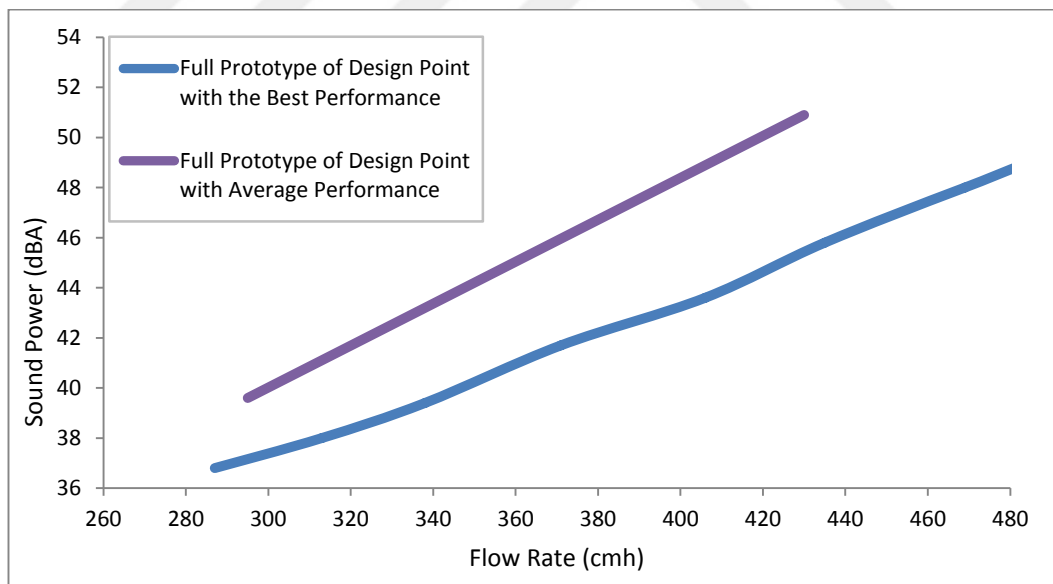


Figure 3.7 Sound power level - flow rate graphs

In the present study, the main research theme was to improve the flow structure by parametrically examining the CFF casing in the SAC. In this effort the vorticity that caused energy losses was reduced which also caused reduce in the aeroacoustics noise.

In Figure 3.7, the full prototype unit with the best performance and a full prototype unit average performance were compared for noise generated per flow rate. The tests are done in an anechoic chamber. As the results examined, it can be seen that average sound power level decreased 3.63 dBA and maximum sound power level decreased 5.94 dBA. As mentioned above, it is confirmed that when the irregularities in the flow are reduced, the noise also decreases.

3.4.4 Repeatability Experiments and Validation

The parametric nature of the prototype results in the inclusion of many interchangeable components, which are mounted and unmounted on a regular basis to achieve different design configurations. This process may result in deformation to these components, which are commonly manufactured via rapid prototyping and, in turn, may affect the outcome of the experiments. Therefore, certain experiments were repeated on a regular basis to review if the outcome of the experiments was affected by any component deformation. The results of the experimental validation process were reviewed, and the influence of used components on the experiment results was determined to be less than 1%.

Figure 3.8 shows a comparison between the experiment and its validation. Between the initial experiment and the validation experiment, 184 different experiments were conducted. As seen in Figure 3.8, following the 184 subsequent experiments, the flow structure and air velocity were not affected during the parametric experimentation process.

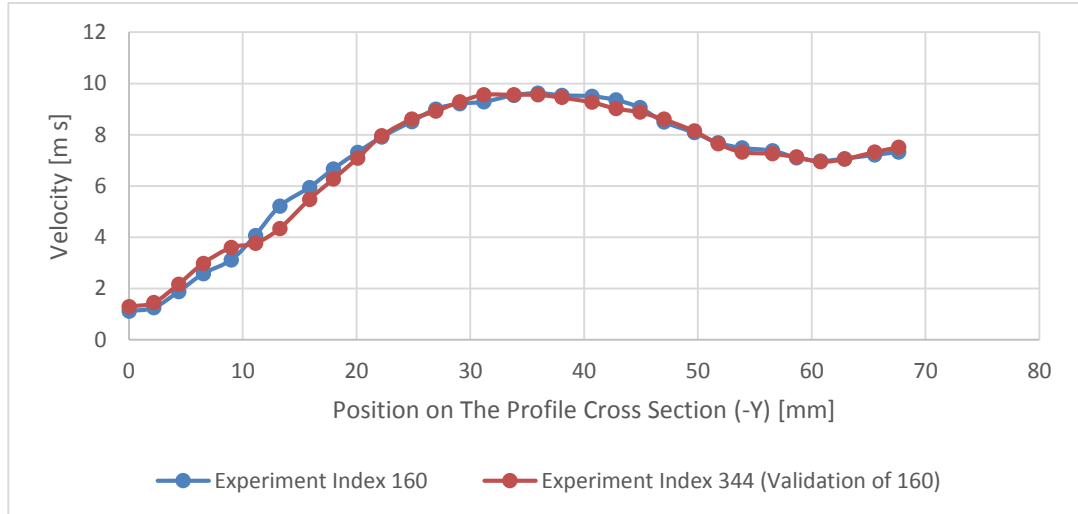


Figure 3.8 Velocity profile comparison between experiment and the validation experiment at design point 160

The uncertainty analysis of PIV measurement is widely different than conversational velocity measurement devices. An anemometry or a hot wire probe measures velocity at an area which is small enough to assume as a single point. Therefore, only one velocity data can be obtained and only one uncertainty exists related to this data. However, in PIV method, velocity data is gathered from areas and obtained velocity maps include several hundred vectors. Therefore, the uncertainty analysis also must be done for every vector. The details of error analysis are given by Raffel et al. (Raffel, M., Willert, C., Wereley, S., & Kompenhans, J., 2007) and Lazar et al. (Lazar, E., De Blauw, B., Glumac, N., Dutton, C., & Elliott, G., 2010).

In this study, the maximum uncertainty at the measurement section is calculated as 2.2% for a single SPIV measurement. It must be noted that in the evaluation process, the average data of 200 measurements were used to decrease the measurement error.

CHAPTER FOUR
INVESTIGATION OF THE CROSS-FLOW FAN INSIDE OF AN
ASPIRATING COOLING SYSTEM FOR REGULATING TEMPERATURE
OF PYROLYTIC OVEN GLASS

The aim of this part of the study is to investigate the design parameter effects of an aspirating cooling system on the outer surface temperature of a household pyrolytic oven glass. Pyrolytic ovens include complicated components, such as an oven door, a CFF and an aspirating cooling system, and their complex interactions should be investigated in detail. In this study, the oven door and CFF and aspirating cooling systems were modeled as a three dimensional system using a computational fluid dynamics and heat transfer method to investigate the fluid flow and temperature distribution of outer surface of the oven door. The simulation model predicted the temperature distribution based on the CFF speed, CFF position and channel design of the aspirating cooling system. The numerical results were validated against results obtained from an experimental study. The computational results show that the rotational speed of the CFF, the CFF position and the channel design of the aspirating cooling system play important roles in affecting the outer surface temperature distribution of the oven glass of a pyrolytic oven.

This part of the thesis consists of the works done on the TUBİTAK (The Scientific and Technological Research Council of Turkey) TEYDEB project encoded 3130615.

4.1 Numerical Study

A computer-aided design (CAD) model of an oven was taken from a white goods company for the numerical study. The CAD model of a pyrolytic oven assembly is shown in Figure 4.1-b. The oven has an ACS for decreasing the outer surface temperature of the oven door. Details of the ACS and oven door are shown in Figure 4.1-b and Figure 4.1-c, respectively. The top view of the system is given at Figure 1d which also shows that the CFF is positioned symmetry plane of the oven.

As mentioned, the main purpose of the ACS is to actively cool the oven door by drawing air between glass panes. The air suction power was provided by the CFF, which was part of the ACS. The oven door consisted of a quadruple glass layer as shown in Figure 4.1-c. Air from the chimney of the oven could be circulated between these glass layers, and a plastic profile was used to hold the glass pane together.

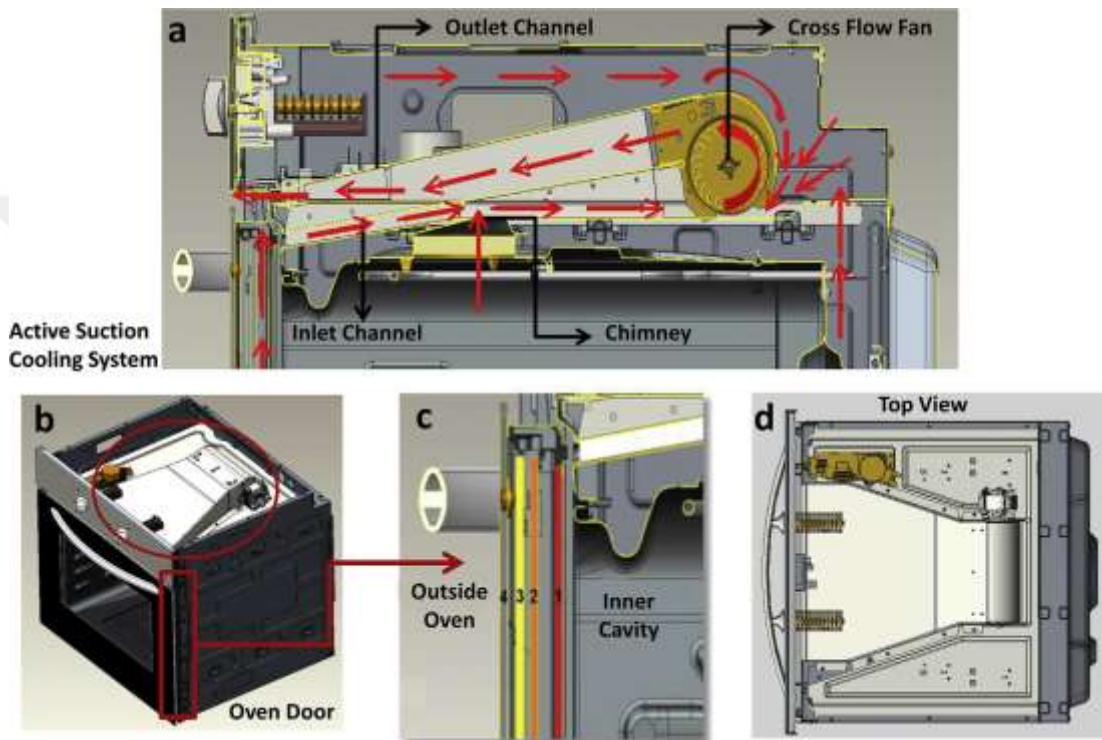


Figure 4.1 Pyrolytic oven views a) aspirating cooling system, b) pyrolytic oven assembly, c) oven door, d) top view of oven

The air volume model of the oven door and the ACS is shown in Figure 4.2-a. The “A” side shown in Figure 4.2-c is the inner cavity of the oven and the “B” side is the outside of the oven.

In the regular ovens without the ACS, the heat transfer from the outdoor surface occurs via natural convection and radiation. However in the ovens with ACS with suction, air suctioned reverse direction of the natural convection and this effects the heat transfer. The outdoor air volume is added to the analysis for investigating this phenomena. The height and the width of the air volume is selected equal to the ovens

size. The depth of the out air volume is related with the diameter of CFF as Shih et. al. (2008) suggested in their study. After some analysis were done to see appropriate size, the depth of outside air volume was determined to be three times the diameter of the CFF.

Glass number 1 (i.e., the eight inner glass panes) is the surface that contacts the oven inner cavity and glass number 4 (i.e., the outer glass pane) contacts the ambient atmosphere surrounding the oven. The structure of the ACS was prepared using a modeling program according to the CAD model of the oven with necessary simplifications and is shown in Figure 4.2-a. To prepare the ACS, the inlet and outlet channels, the chimney area and the fan were modeled. The system has two main bodies, which are the fan and the air cavity. A model of the CFF is shown in Figure 4.2-b. As seen from Figure 4.2-a, only half of the full oven door and ACS CAD were modeled because the air flow in the door was symmetrical.

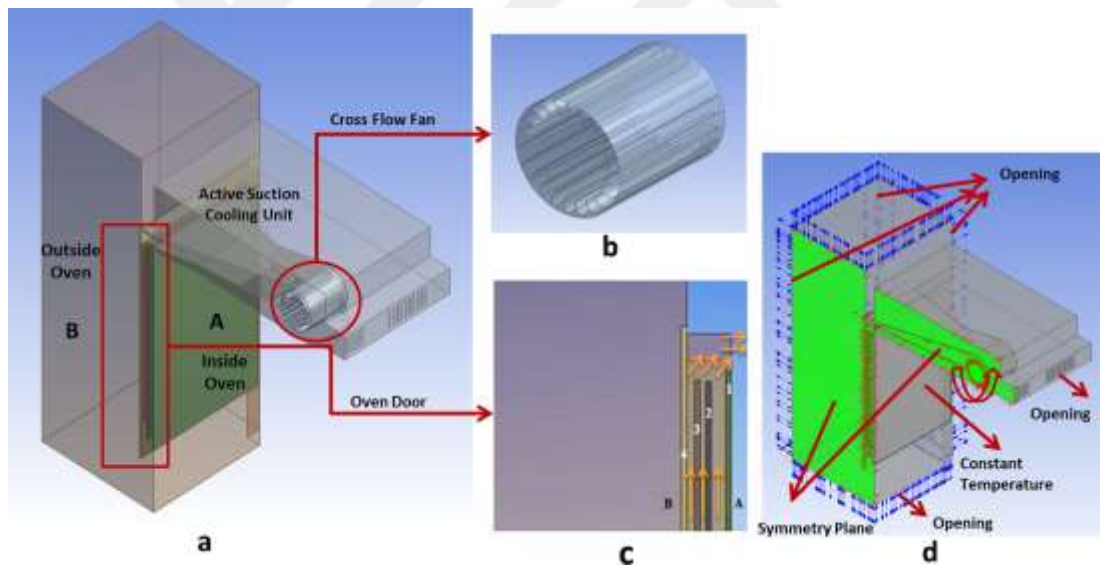


Figure 4.2 Three dimensional air volume model a) model of oven door and aspirating cooling system, b) model of CFF air, c) model of oven door and air circulation of the oven, d) boundary conditions of model

To provide a realistic simulation, the CFDHT analysis generated a proper numerical grid model. The mesh structure of the system is shown in Figure 4.3-a. Because the thickness of the glass panes and the air gaps between the glass panes were small, the mesh element sizes were small for these regions. The body of the ambient air volume

of the rest of door was meshed normally as shown in Figure 4.3-b. Fins of the CFF were very small compared with the air cavity. Overall, different domains meshed with different element sizes. The mesh details of fan are shown in Figure 4.3-c and Figure 4.3-d.

Different sizes of mesh elements was applied to the model and tried to find optimal number of elements for the final model. As it seen from Table 4.1 different number of mesh was applied to the CAD model. For comparing the cases average temperature of the outer surface of fourth glass were noted. Four models were prepared to see the effect of the number of elements. Even the model, which has the minimum number of elements and nodes (Case 1) having 1 degree accuracy. If the number of elements increases solver needs more time to get results but if number of elements is not enough model cannot validate the experimental results. If the other parameters that affect the CFD results are done properly, to get best converging results meshing process needs more time to spend on. Case 2 was chosen for this study as a final model. The final mesh structures of the oven door and ACS and is shown in Figure 4.3.

Table 4.1 The study of determining optimum mesh model

Case	Number of Elements	Temperature at Outer Surface [K]
Case 1	3,436,288	324.31
Case 2	5,273,651	322.25
Case 3	10,285,361	322.31
Case 4	30,224,854	322.66

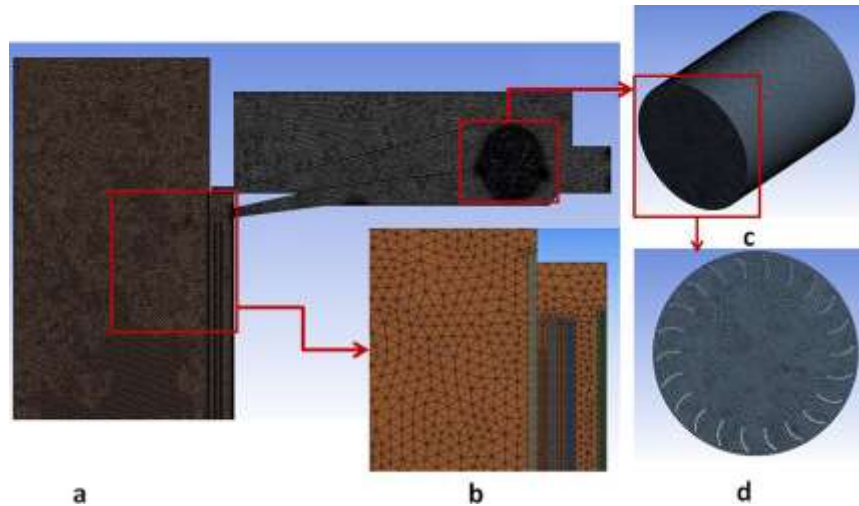


Figure 4.3 Mesh details of the air volume model a) mesh detail of oven door and aspirating cooling system, b) mesh detail of oven door, c) mesh detail of fan, d) front view of fans' mesh detail

After preparing the mesh, the boundary conditions of the model were defined. The air in the oven door and the ACS, the glass panes and the plastic profile were set as stationary domains whereas the fan was set as a rotating domain. The rotating speed of the CFF was set at 2,400 rpm (which was further investigated in the parametric part of this study). The entrance and exit of the inlet and outlet channels, respectively, of the ACS and the chimney surface were defined as openings.

The outer surfaces of the air model exposed to the ambient atmosphere were defined as open boundary conditions. The necessary symmetry planes of all bodies were also set at the required boundaries. The remaining faces which were not openings or symmetry planes were assigned as no slip boundaries. The ambient, opening temperature was defined at 25 °C. The main heat transfer mechanism on the outside of the oven door was set as natural convection. As mentioned earlier, previous studies have compared different radiation models (Mistry et al., 2006). However, no major differences in calculated temperatures have been reported based on these different models. Therefore, a surface-to-surface radiation model was selected for this study due to more rapid model convergence. Furthermore, k-epsilon turbulence model was selected for this study. Temperature values obtained from these previous experiments were used to define the first glass inner surface that intersected with the inner cavity of the oven. The previous experimental studies were performed when the systems were in thermal balance. Therefore, the numerical modeling of the current study were

performed at steady state. The boundary conditions of model were shown in Figure 4.2-d.

4.2 Validation of Computational Fluid Dynamics Results

4.2.1 Fluid Flow Verification

To validate the velocity field of the ACS, velocity measurement tests were performed and compared with the CFD analysis. In the experiments, eleven of sixteen hot wire anemometers were placed on the air flow inlet of the ACS. The remaining anemometers were placed on the air flow outlet. The positions of the anemometers for the velocity measurements of the ACS are shown in Figure 4.4. When the system reached a steady state, air flow data were recorded every 0.3 seconds over the duration of approximately five minutes. After completing the experiments, the average flow data over the entire inlet and over the entire outlet were obtained to validate the numerical results.



Figure 4.4 Arrangement of anemometers in experimental study (Personal archive, 2014)

The CFD results are shown in Figure 4.5. The fluid flow velocities of the ACS and the oven door are shown in Figure 4.5-a and Figure 4.5-b.

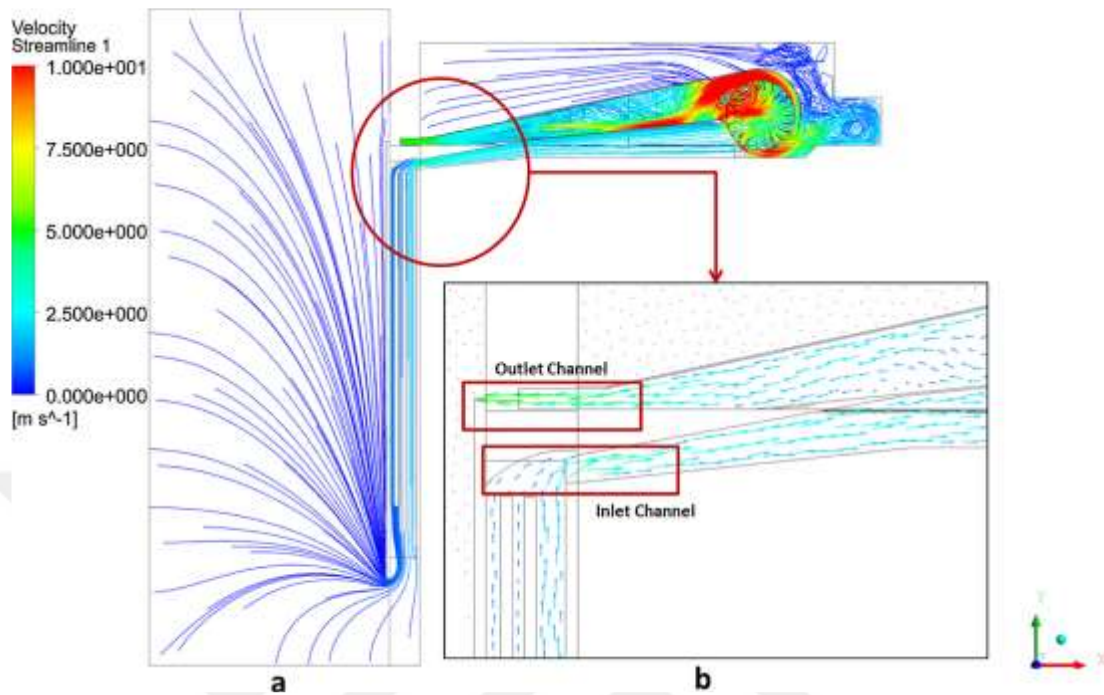


Figure 4.5 Fluid flow of CFD study a) ACS and oven door, b) details of the inlet and outlet ACS

The average velocity of the air at the suction opening in the ACS was 2.98 m s⁻¹. The average velocity at the outlet of ACS was 6.92 m s⁻¹. The differences between the experimental and numerical studies are shown in Table 4.2. The numerical results are similar to the experimental results, i.e., the CFD model was validated by the experimental study for these simulated conditions.

Table 4.2 Comparison of the computational and the experimental study for the inlet and outlet channel of ACS unit

Average velocity (m/s)	Experimental study	Numerical study	Absolute Difference
Inlet	3.07	2.98	0.09
Outlet	7.78	6.92	0.86

4.2.2 Temperature Distribution Verification

The CFDHT results were validated and compared with experimental results. A temperature experiment was performed during the pyrolytic cycle of 1.5 hours. For all experiments, the ambient temperature was set at 25°C. The surface temperature of the outer glass door was measured by a digital infrared thermometer which has 0.5% accuracy three minutes prior to the completion of the cycle. In addition, the surface temperature distribution was obtained via the thermal camera which has Thermal sensitivity < 30 mK. The temperature data obtained by the thermal camera and digital thermometer were used to validate the numerical study.

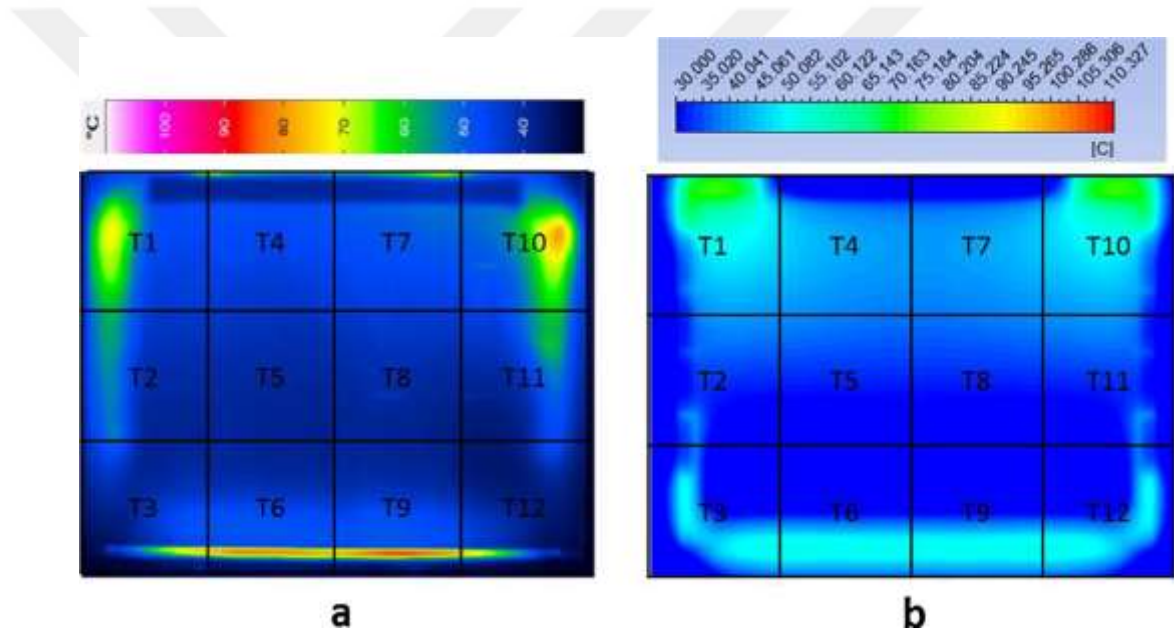


Figure 4.6 The temperature distribution of the outer surface of oven door a) experimental results, b) computational results

Figure 4.6-a shows the temperature distribution of the outer surface of the oven door in the experimental study. The measured temperature values (i.e., T1, T2, ..., T12) were reported as the maximum temperatures values of the area (Figure 4.6-a). In the numerical study, the temperature distribution of the outer surface of the oven door is shown in Figure 4.6-b.

Table 4.3 shows a comparison of the experimental and numerical results. The maximum error in the analysis is noted as 15 K which is a point wise error. The maximum relative error between the temperature and analysis data was 4.42 %. The relative error values ranged from 0-4.42 %.

Table 4.3 Temperature comparison between experimental and computational results

Temperature of test data	Experimental Results (°K)	Numerical Results (°K)	Error (%)
T1	343	358	4.37
T2	330	334	1.21
T3	325	338	4.00
T4	317	321	1.26
T5	312	312	0.00
T6	320	331	3.44
T7	321	321	0.00
T8	311	312	0.32
T9	317	331	4.42
T10	352	358	1.70
T11	332	334	0.60
T12	324	338	4.32

A scatter plot comparing the numerical and experimental temperature data is shown in Figure 4.7. Both data sets were similar. This shows that the oven door and ACS can be modeled using the numerical study to estimate parametric values.

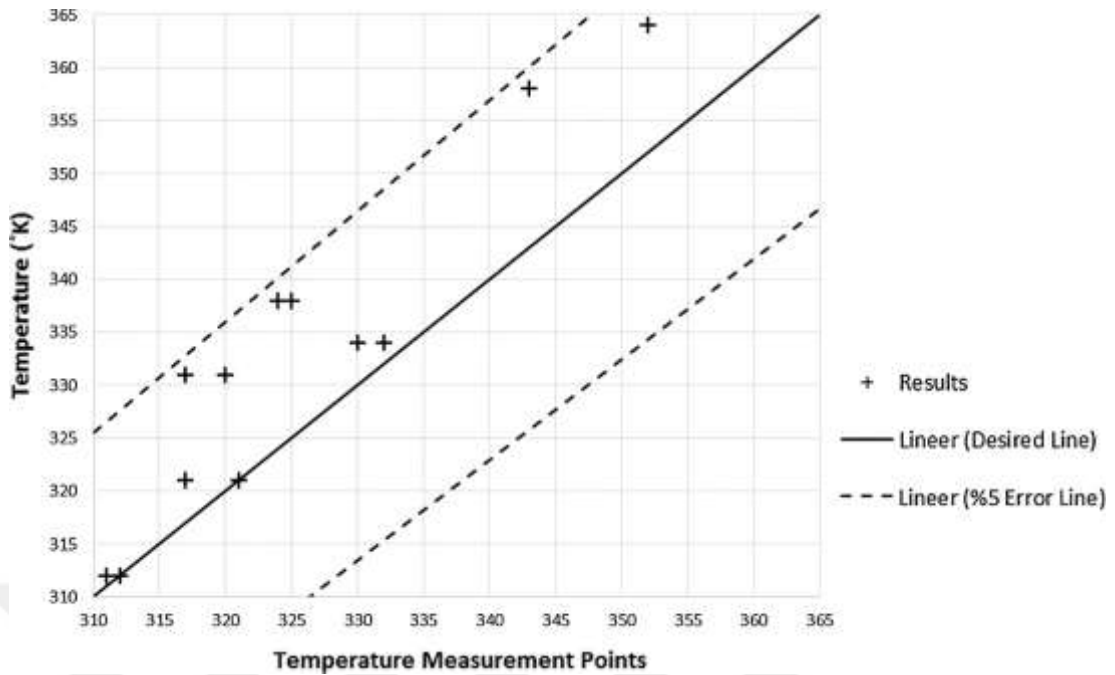


Figure 4.7 Scatter plot comparing the numerical and experimental temperature data

4.3 Parametric Study

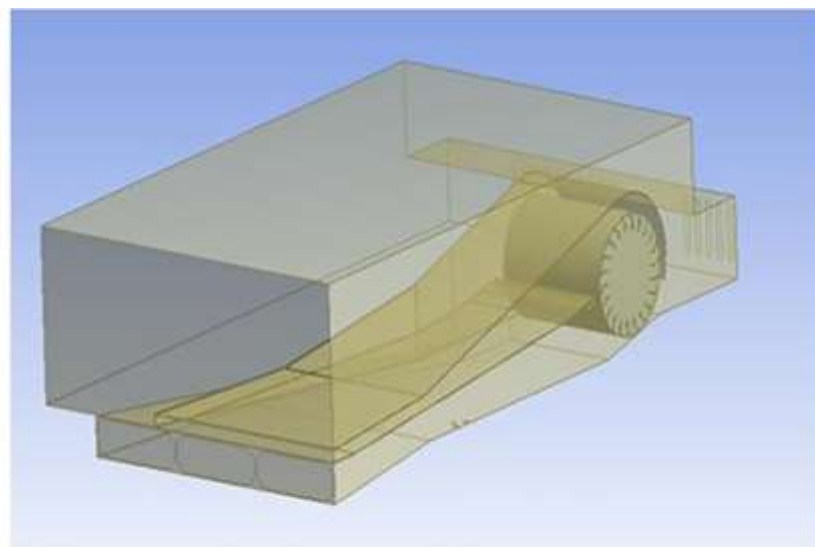
4.3.1 Effects of Position of the Cross-Flow Fan

The structure of the CFF with an impeller, a back wall, a vortex wall and a motor is shown in Figure 4.8.

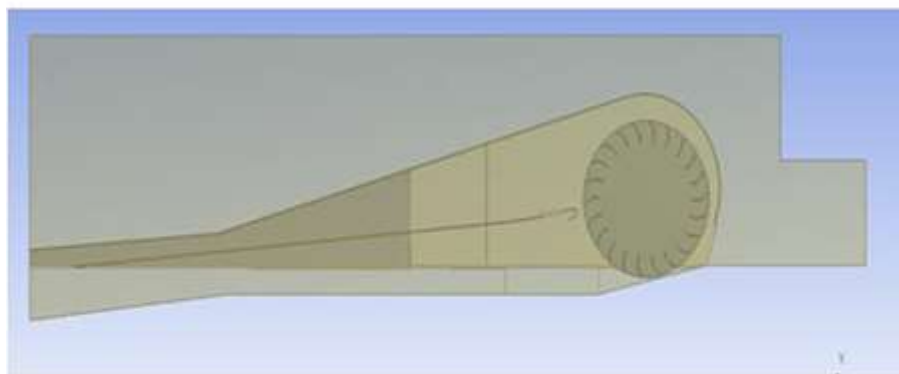


Figure 4.8 Mechanical construction of CFF

As a priority in the numerical study of ACS, the optimum position of the CFF was determined based on operational principles. Depending on this position, the design parameters and positions of the inlet and outlet channels of the ACS were determined according to the literature and the limits of mechanical construction. The three dimensional air volume model of the ACS was prepared for CFD analyses. An air volume model of a first ACS design is shown in Figure 4.9-a and Figure 4.9-b. The first model examined whether a lower suction inlet channel design was effective, depending on the location of the CFF.



a



b

Figure 4.9 a) Air volume model of ACS, b) Cross-sectional view of ACS air volume model

Three different CFF locations were investigated. The simulation results of the different locations of the CFF are shown in Figure 4.10-a, Figure 4.10-b and Figure 4.10-c.

As shown in Figure 4.10-a, Figure 4.10-b and Figure 4.10-c, the optimal velocity distribution was observed for the CFF location represented in Figure 4.10-c. Based on these numerical studies, the position of the inlet channel was located 5 mm from a tangent to the CFF blades.

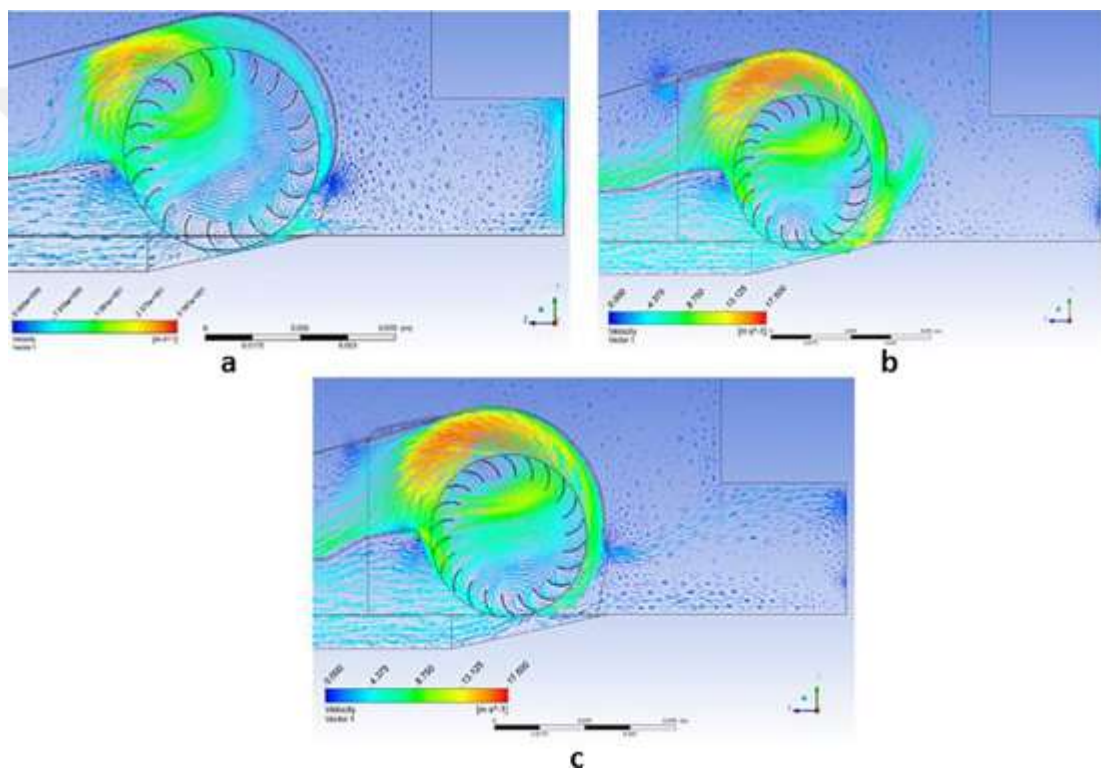


Figure 4.10 Velocity vectors of ACS a) Inlet channel and CFF tangent, b) Back wall 2.5 mm from CFF, c) Back wall move away 5 mm from CFF

In addition to this improvement, to maintain an airflow balance, which is suctioned from behind the CFF and from the oven door, the back wall design was studied. To determine the optimum angle (θ) and sizes of the back wall (P1, P2) parametric studies were performed. Figure 4.11-a shows pressure contours of the ACS around the CFF. Figure 4.11-b shows a schematic view of the working principle of the CFF.

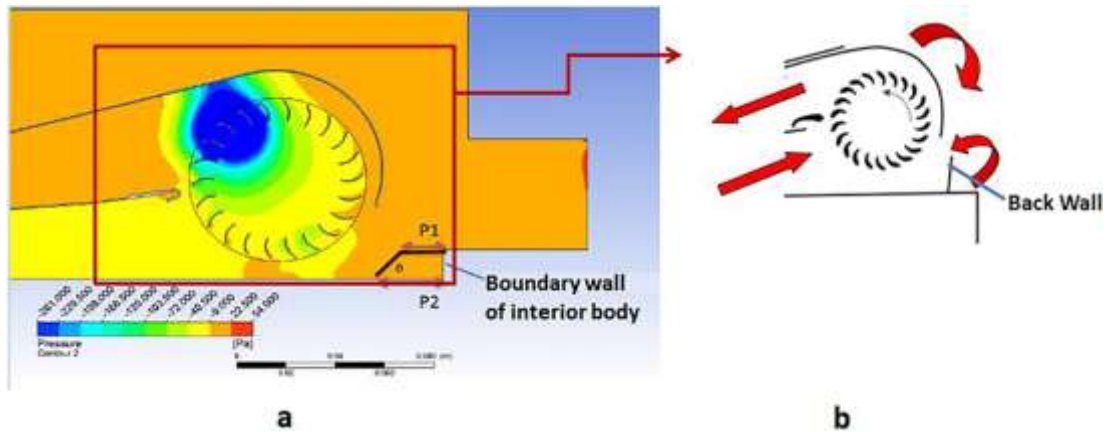


Figure 4.11 The optimum positioning of the inlet channel depending on the boundary wall of interior body a) pressure contours of ACS, b) schematic view of CFF

As a result of the numerical studies, the optimum angle and size of the back wall were determined. The design input parameters (P1, P2 and \emptyset) and corresponding suction channel inlet velocity are shown in Table 4.4.

Table 4.4 Variations of velocity due to sizes and angle of back wall

	P1 (mm)	P2 (mm)	\emptyset ($^{\circ}$)	Inlet velocity of the suction channel (m/s)
DP 0	10	20	53.67	2.88
DP 1	15	25	52.27	1.95
DP 2	10	15	68.85	2.49
DP 3	10	25	40.73	2.44
DP 4	5	10	68.85	2.77
DP 5	7.5	15	59.88	2.79
DP 6	7.5	20	45.96	2.98
DP 7	7.5	25	36.46	2.74

As shown in Table 4.4, the maximum velocity of the suction channel was observed for DP 6. If the inlet velocity of the channel increased, the average temperature of the

outer surface of the oven door decreased. Thus, for the back wall design, the parameters that defined model DP 6 was selected.

4.3.2 Effects of Design of the Upper Blowing Channel

After determining optimum CFF position and the angle and size of the back wall adjacent to the CFF, the upper blowing outlet channel was investigated. The entry area (i.e., the CFF fan outlet) was fixed, and the output area (i.e., just outside the mouth opening of the outlet channel) was varied, as shown in Figures 4.12.

Depending on parametric studies, the optimum value of the outlet channel blowing area was determined. The parameters of the upper blowing channel are shown in Table 4.5.

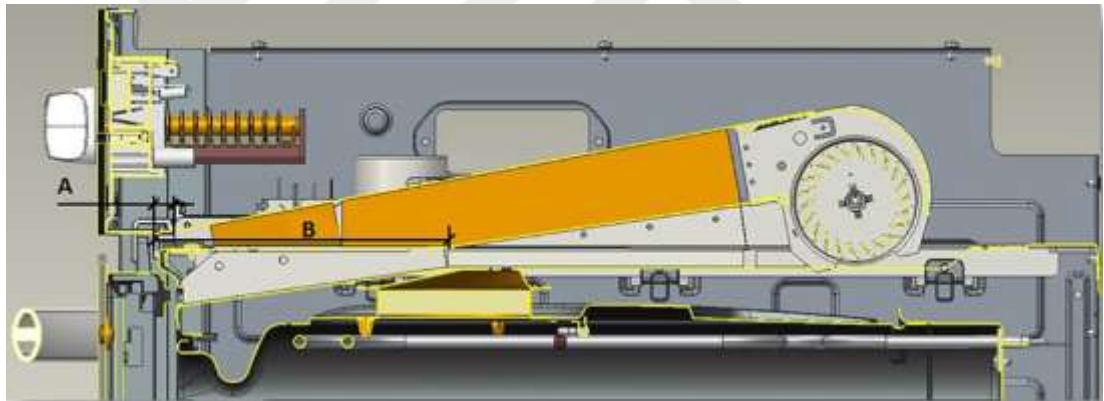


Figure 4.12. The structure of upper blowing channel

Table 4.5 Design data of upper blowing channel

Design Points	A (mm)	B (mm)	Pressure of	Design Points	A (mm)	B (mm)	Pressure of
			Outlet Channel (Pa)				Outlet Channel (Pa)
P1	100	20	0.00361700	P14	35	25	0.00292787
P2	90	100	0.00361645	P15	40	50	0.00289826
P3	100	100	0.00355916	P16	30	60	0.00288071
P4	80	90	0.00334849	P17	20	25	0.00285925
P5	60	100	0.00325768	P18	30	70	0.00283898
P6	70	80	0.00323822	P19	15	20	0.00278477
P7	60	70	0.00322628	P20	20	10	0.00275407
P8	60	60	0.00322119	P21	10	20	0.00274435
P9	100	60	0.00318347	P22	20	20	0.00274428
P10	50	60	0.00312891	P23	20	60	0.00273204
P11	60	20	0.00309237	P24	20	50	0.00270971
P12	25	15	0.00303135	P25	20	70	0.00261756
P13	25	35	0.00295115	P26	10	60	0.00234585

There was no noticeable pressure difference between the different designs as shown in Figure 4.13. When horizontal dimension A was 10 mm and horizontal dimension B was increased from 60 mm, the resulting differences in pressure values were negligibly small. Due to the physical constraints of the channel, dimension A was set at 10 mm and dimension B was set at 150 mm.

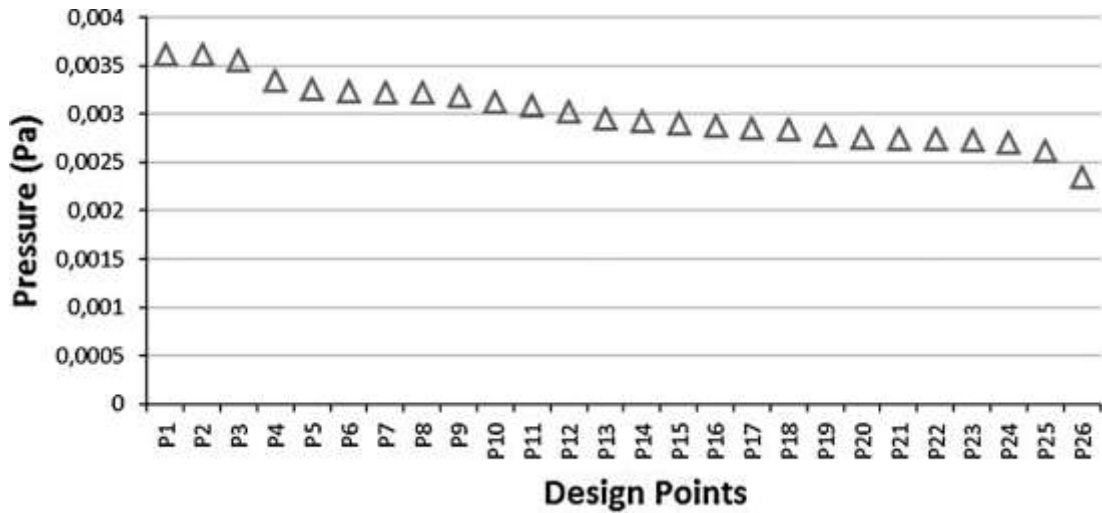


Figure 4.13 Pressure comparison between design points of upper blowing channel

After the parametric studies, validation experiments were performed and compared with the CFD analysis. An initial model was verified by an experimental study before continuing with the parametric numerical studies. A final ACS prototype was developed, and the experimental studies were repeated. The results of the numerical studies of the initial and final models are shown in Table 4.6.

Table 4.6 Velocity comparison between first and final model of ACS system

	Outlet	Inlet
First model	5.91 m/s	2.18 m/s
Final model	6.92 m/s	3.07 m/s
The rate of increase	17.02 %	40.8 %

Following these parametric studies, the ACS and the fluid flow of the system were improved. The average velocities of the airflow at the inlet (suction) and the outlet (discharge) of the ACS were increased by 40.8 % and 17.02 %, respectively. As the velocity increased, the outer surface temperature of the oven door decreased.

4.3.3 Effect of Rotational Speed of Cross-Flow Fan

At the oven door, heat is transferred by conduction, convection and radiation. In the oven cavity, the air is heated by heaters and circulates in the oven. In pyrolytic ovens,

radiation is the dominant heat transfer mechanism because of the high temperatures. Radiation emitted by the heaters causes the door air cavity to heat up. The active suction system cools down the door cavity by convection. To determine the effect of the CFF rotational speed, the Reynolds number of the airflow was calculated according to Equations 4.1 and 4.2. The Reynolds number was based on the rotational speed of fan (n ; rpm), the impeller external diameter (D ; mm), the length of the blade chord (c_p ; mm) and the kinematic viscosity (ν ; $\text{m}^2 \text{s}^{-1}$).

$$Re = \frac{U_L \cdot c_p}{\nu} \quad (4.1)$$

$$U_L = \frac{2 \cdot \pi \cdot n}{60} \cdot \frac{D}{2} \quad (4.2)$$

Figure 4.14 shows the effect of the Reynolds number (Re) on the surface temperature of the oven door. The first vertical axis shows the average outer surface temperature (Kelvin) of the oven door, and the second vertical axis shows the average velocities (m/s) of the inlet and outlet channels. The horizontal axis shows the Reynolds number.

The increase of the Reynolds number depends on the fan rotational speed. As shown in Figure 4.14, a minimum temperature was acquired when Re was 8,540. Above a Re of 4,880, there were no noticeable effects on the outer surface temperature of the oven door. However it must be noted that the Reynolds Number also related other parameters such as fan cord length. These parameters may have an additional effects on the flow characteristics.

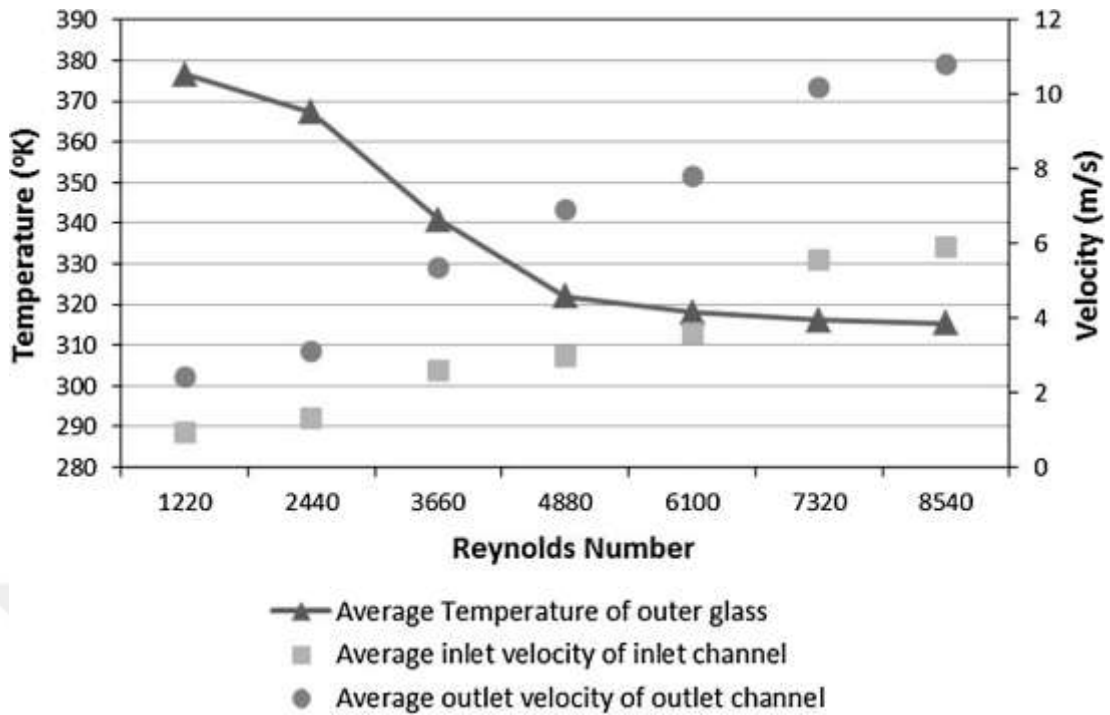


Figure 4.14 The effect of speed of the CFF on the outer surface of oven door

4.3.4 The Cumulative Effects of Parametric Studies on Aspirating Cooling System to the Surface Temperatures

As a final evaluation of this study, 3 prototype oven compared experimentally. The first model was the oven without ACS, the second one was the early prototype with ACS before CFD study and the last one was the oven design with ACS enhanced with the parametric study on this paper. The half of the oven door separated in to 12 areas and the maximum temperatures in these areas are noted both with infrared camera infrared thermometer. “L” represents the total width of the oven door and X=0 represents the mid area. The half oven doors surface temperature distributions at the pyrolytic stage are given in Table 4.7.

Table 4.7. Surface temperatures ($^{\circ}\text{C}$) obtained from the comparison experiments

Prototype 1 (without ACS)			Prototype 2 (with ACS, before optimization)			Prototype 3 (with ACS, after optimization)		
X=0	X=L/4	X=L/2	X=0	X=L/4	X=L/2	X=0	X=L/4	X=L/2
92	130	82	81	77	71	61	60	47
70	75	86	49	52	82	40	43	65
52	57	72	44	45	80	38	37	52
53	50	48	37	37	53	45	40	42
Average		72,25	Average		59	Average		47
Maximum		130	Maximum		82	Maximum		65

The results show that even the ACS without design optimization reduces the average surface temperature of the oven 13.25 K. Also the maximum temperature of the oven door decreased 48 K. As the temperature distributions of the prototype 1 and prototype 2 inspected, it can be noted that the major reduction takes place at the center areas. The reason of this situation is the CFF length is shorter than the oven door (Can be seen in figure 1d.) and air suctioned from the CFF is not enough to effect the sides.

After the parametric study, the suctioned air average velocity increased 40.8 % as mentioned. This caused an extra 12 K reduction on the average temperature of the oven door in respect to Prototype 2 and 25.25 K reduction in respect to Prototype 1. The maximum temperature of the prototype 3 is 65 K less than Prototype 1. The temperature distribution of the prototype 3 is also more homogeneous due better use of the air channel between the oven door glasses.

CHAPTER FIVE
IMPROVEMENT OF FLOW STRUCTURE. HEAT TRANSFER AND
PERFORMANCE OF SPLIT AIRCONDITIONER OUTDOOR UNITS AND
DESIGN PROCESS OF NOVEL CROSS-FLOW FAN OUTDOOR UNIT

This part of the thesis consists of the works done on the TUBİTAK (The Scientific and Technological Research Council of Turkey) 1505 project with the 5140039 encoded.

The project aimed at designing a high performance inverter split air conditioner outdoor unit (SACOU) and plans to improve the flow structure and heat transfer in the inverter units with axial fan SACs. Within this scope; the flow structure of the devices will be examined using SPIV and three-dimensional average velocity distributions was obtained. EPIV technique was used to display closed volumes of the system. Thus, an axial fan with a higher flux than the present system was designed with a suitable air flow geometry and heat exchanger. In addition, CFD analyses will be utilized.

On the other hand, a prototype of a unique outdoor unit with a crossflow fan will also be developed. Although the crossflow fan is applied to the outer unit and patent studies are found at the prototype level, serial production has not yet passed. At this point, CFFs can be used for making quieter, more compact and more efficient outdoor units than axial fans.

The prototype of the outdoor unit with CFF was obtained as a result of the study and it was compared with the conventional axial fan prototype produced in the other part of the research. Their advantages were evaluated. Thus, the SACUO developed as a result of the progeny was emerged as a new product.

5.1 Design and Comparison of Alternative Axial Fan Designs With Numerical and Experimental Methods

In this part of the study Fanpal program is used for designing a new fan. Fanpal is a parametric fan analysis program that can be used both for the design and for the improvement of the fan to the desired conditions. In this sense, the design consists of three main stages.

At first stage; Fan type, flow rate, number of revolutions, fan diameter ...etc are given as input to the program. It automatically presents a preliminary design by querying the parameters. However, this preliminary design presented provides an infrastructure that can be modified much more than reflect the desired fan.

With the acquisition of this infrastructure, the second phase of design begins. In this process, the engineer who designed the fan, arrange the parameters such as the blade inlet angle, the blade length, the axial blade length, the blade thickness, the blade diameter...etc. By setting these parameters, the fan was made more efficient and suitable for the desired conditions. One of the important points in the axial fan design is that all of these parameters are variable through the diameter of the fan blade. Therefore, when a parameter was examined in the wing design, the values of the blade tip, the blade center and the blade hub were examined separately. The screen image taken at this stage is shown in Figure 5.1. Figure 5.1 shows the visual wing cut at the bottom right. Graphic sections can be adjusted according to the parameter to be examined.

After this work is completed, the third and last stage started. In this phase, the AxCent program, a subprogram of the Fanpal program, is used. In this program, both the Blade entrance angle, exit angle and blade form are fine-tuned and the three-dimensional geometry of the fan is created. Figure 5.2 shows a screenshot taken at this stage.

As shown in Figure 5.2. AxCent has a much wider and more complex interface because it is three-dimensional. The effects of these parameters on the other side of the blade are investigated in detail.

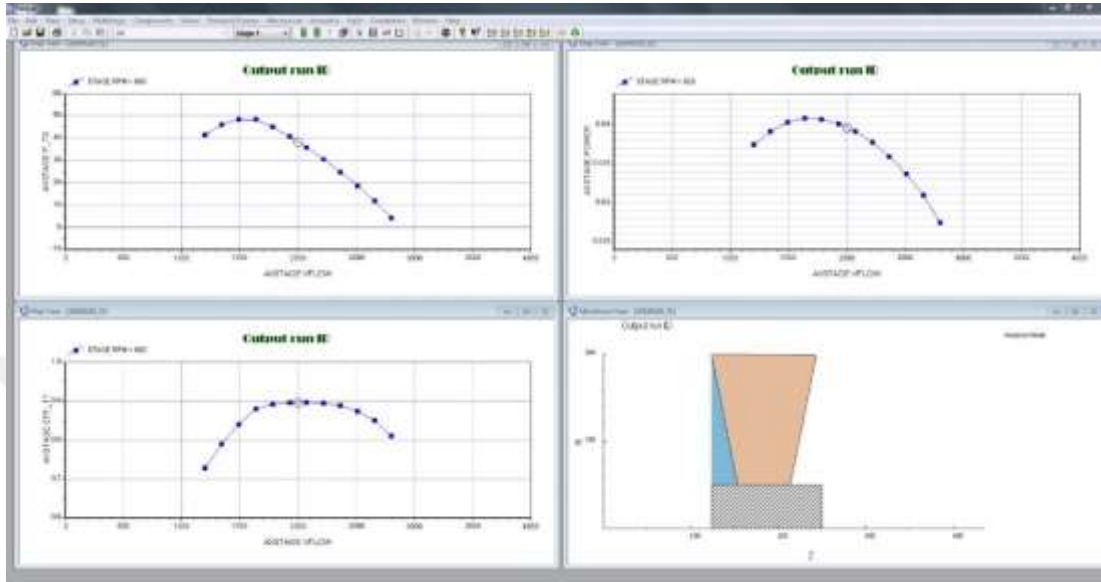


Figure 5.1 Screenshot taken in fanpal fan design process

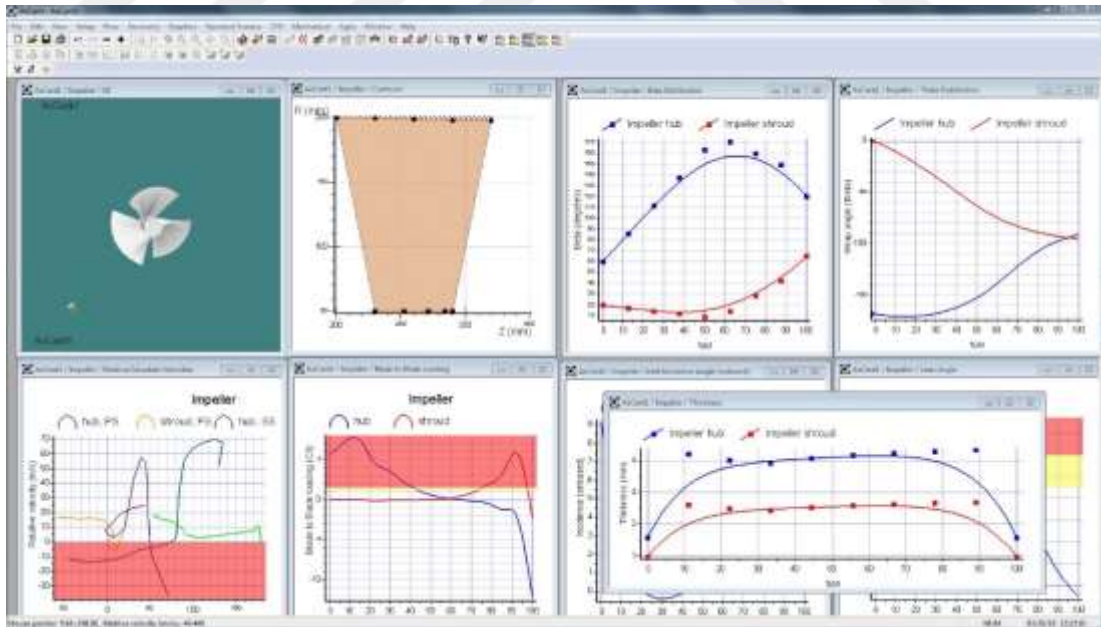


Figure 5.2 Screenshot taken in the fan design process in AxCent

When the process is briefly transferred; the first two prototypes produced did not deliver the desired performance and showed a lower performance than the company's existing fan. In the third prototype produced, the desired success was achieved and at 270 rpm the prototype fan drove the same air rate which the current fan achieved at 700 rpm. After achieving this result, it was directed towards alternative designs that were quieter and less space-saving so fan number four was created. There is also a version with a knot in the wing outlet area of fan number 4 to see whether better sound performance can be achieved. The basic goal in this design is to create less sound by breaking the vortex that the canvas air creates. The designed fans are shown in Figure 5.3 and the results obtained for these fans are presented in the next section.



Figure 5.3 Photographs of newly designed and produced fans (Personal archive, 2015)

5.1.1 Numerical and Experimental Methods of Designing Conventional Outdoor Unit with Alternative Axial Fan

As mentioned in the previous section, although the fans have to be designed separately, they have to be considered together with the outdoor unit. The main reason for this is that the fan is designed according to the pressure drop created by the outdoor unit.

The first improvement made with the outdoor unit geometry was made in the grid in front of the fan for security purposes. The main task of the grid is to prevent street animals, people and other objects from reaching the high-speed spinning fan. Grid is

an obstacle in the flow while providing this task. The reduction of the pressure drop caused by the grid will affect the efficiency of the system positively. To achieve this, a parametric study has been carried out on the wing form. The parameters examined in this study are shown in Figure 5.4.

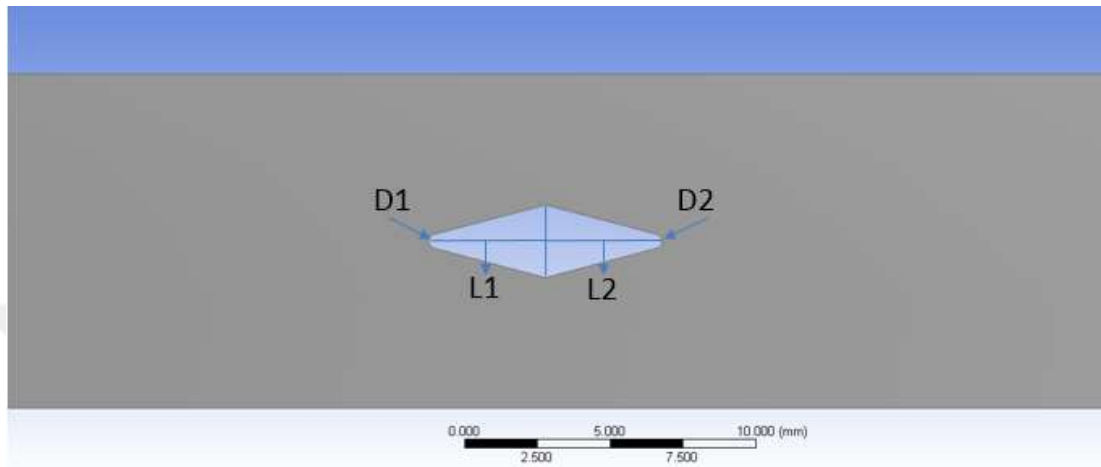


Figure 5.4 Parameters of the examined profile

When Figure 5.4 is examined, the parameters of the wing's form and variables are seen. The height of the profile has been chosen to be appropriate to the standard so that the product can be removed from the mold and the necessary main safety measures can be taken. The remaining parameters were tried to be improved to reduce pressure drop. D2 is the diameter of the wing tip at the rear end of the profile. L1 and L2 are the distance of the profile tips from the mold surface.

By changing these parameters, 200 different designs have been examined in numerical analysis. Table 5.1 presents the best 28 design results.

Table 5.1 Parametric study result shows the best 28-profile design

	A		B		C		D		E		F
1	Name		P11 - D1 (mm)		P14 - L2 (mm)		P15 - D2 (mm)		P21 - L1 (mm)		P8 - pres (Pa)
56	13	DP 599	1,1072		4,1896		1,9537		7,9703		-6,6381
57	77	DP 481	1,2947		5,1119		1,2697		5,3363		-6,6483
58	60	DP 507	1,0271		7,7676		1,4366		4,0523		-6,6563
59	198	DP 566	1,4852		6,0012		1,752		6,9672		-6,6709
60	29	DP 519	1,9882		6,1084		1,488		4,4525		-6,6745
61	104	DP 577	1,0913		7,8141		1,7856		6,7556		-6,6781
62	1	DP 524	1,5		6		1,5		6		-6,6849
63	195	DP 469	1,527		5,6924		1,2138		5,1807		-6,6859
64	185	DP 444	1,2977		5,6618		1,0219		5,0224		-6,6879
65	170	DP 563	1,1279		7,8135		1,7445		5,1266		-6,7066
66	197	DP 567	1,4565		6,0813		1,762		4,9424		-6,7285
67	69	DP 538	1,5897		7,9601		1,5824		6,1702		-6,7295
68	172	DP 542	1,0152		4,1396		1,631		5,0769		-6,7313
69	40	DP 440	1,6026		6,0534		1,0185		7,9656		-6,7405
70	17	DP 441	1,1681		4,4914		1,0206		7,8849		-6,7422
71	145	DP 555	1,2885		7,8315		1,7145		4,06		-6,7424
72	184	DP 526	1,5484		4,9689		1,5073		7,0618		-6,7536
73	53	DP 484	1,724		6,9422		1,2751		6,9491		-6,7705
74	94	DP 491	1,307		4,8248		1,2952		6,9167		-6,7739
75	92	DP 451	1,5583		4,541		1,0435		7,6845		-6,7754
76	75	DP 474	1,7438		4,9053		1,2412		4,9615		-6,7759
77	168	DP 565	1,3318		7,1711		1,7487		5,998		-6,7846
78	128	DP 432	1,483		6,7721		1,013		5,2285		-6,7888
79	101	DP 613	1,1792		5,0708		1,9812		4,8982		-6,7941
80	115	DP 620	1,2546		6,9716		1,9943		7,286		-6,7954
81	146	DP 508	1,6911		6,0376		1,4435		5,0829		-6,8053
82	20	DP 511	1,483		7,9419		1,4569		7,7009		-6,8081
83	23	DP 443	1,5248		5,8876		1,0218		4,3598		-6,8083

These results have been evaluated by the firm and the best design has been produced. As a result of the flow tests made, the new grid is provided with a flow rate increase of 3% compared to the old grid.

After the completion of this work, studies were started to test the newly designed fans in the outdoor unit. The obtained results are presented in Figure 5.5.

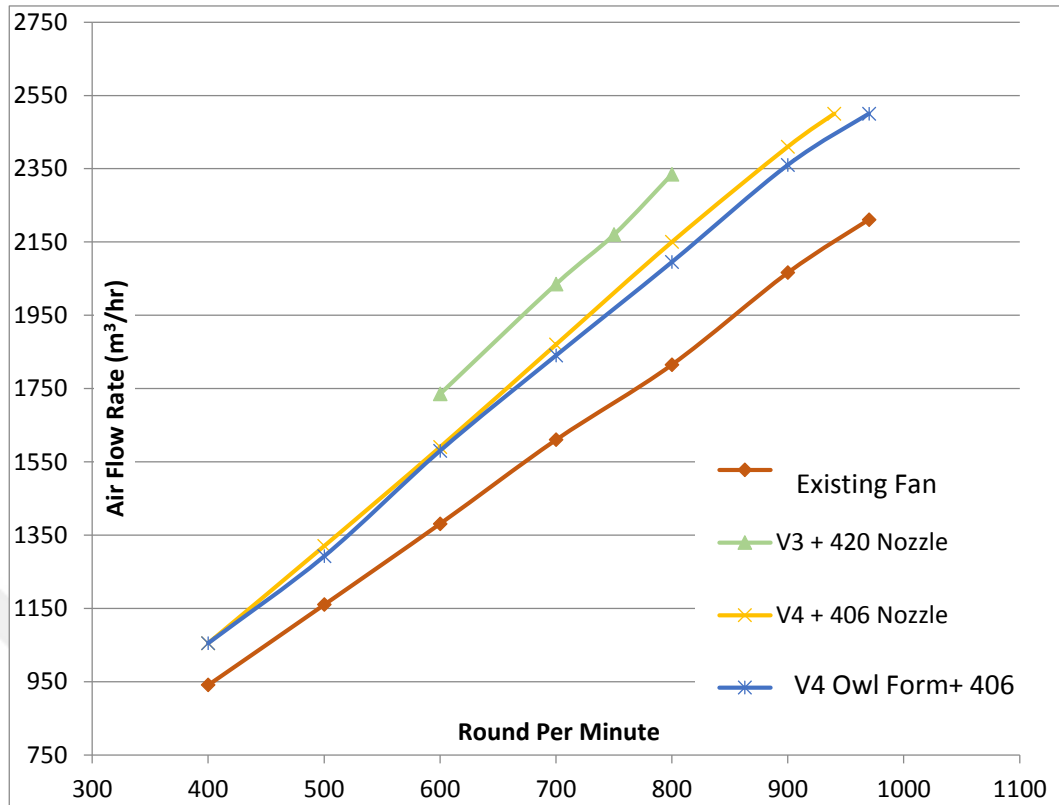


Figure 5.5 Air flow Rate-RPM of axial outdoor fan graph

Looking at Figure 5.5, it is seen that the V3 fan produces the highest flow rate per revolution. It can also be determined that the V4 fan with smaller dimensions is better than the existing one. Another innovation made for reduce the sound by adding an owl wing from at the end of the V4 fan. It has been observed that this innovation is not an effect on the negative or positive direction.

The fans have also been evaluated for sound. However, the increase of the influence directly affects the voice. For this reason, the fans in Figure 5.6 are evaluated from the sound they create according to their fans.

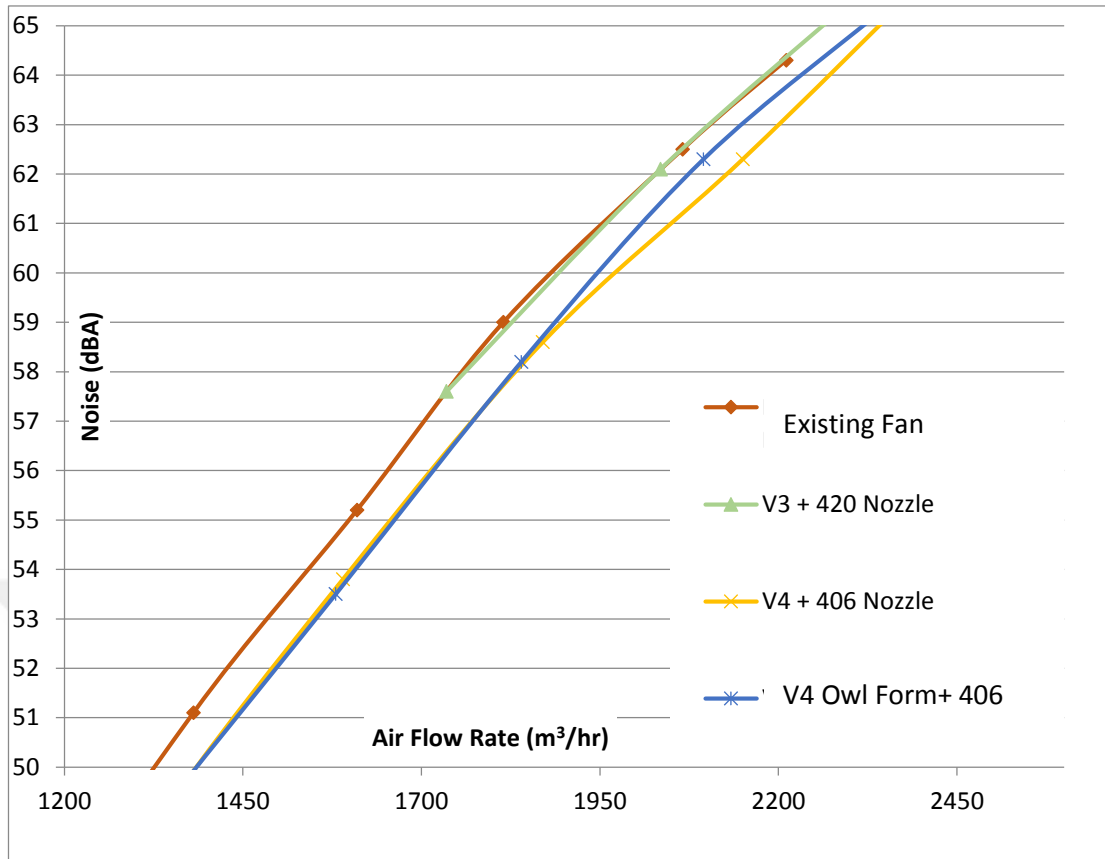


Figure 5.6 Noise-air flow rate comparison of axial outdoor fans

When the figures in Figures 5.5 and 5.6 are evaluated together, it can be said that the V3 is a slightly louder fan compared to the V4, despite its higher flow performance. Also, the V4's depth and diameter are smaller than V3, providing an advantage in designing smaller outdoor units. Compared to its own, owl formed version of the V4, the sound level is better. Therefore, V4 is selected as the best design.

5.1.2 Evaluation of Alternative Add-ons on Blade Forms for Reducing the Noise

In this part of the study, novel wing forms for reducing the noise evaluated. These add-ons were added to fan V4. Two types of add-ons were designed.

The first one of these is the rounded blade tip form for reducing the tip vortex of the blade. This form is used at plane wings for reducing the noise and energy consumption. This form is given at Figure 5.7.

However, a new design has to be applied because the wing form of aeroplane and the wing form of the axial fan are very different from each other. The prototype fan with this new rounded-shaped has been reduced the noise despite the fact that the tests do not result in loss of flow rate. These results are given at the end of this chapter in the final comparison.



Figure 5.7 Form used on aircraft wings to break the tip vortex (www.airbus.com)

The other add-on placed at V4 is the droplet forms which placed at the axial fan surface. The droplet forms to be added on the fan blades are firstly numerically investigated by the CFD method. In these analyses, the droplet inlet radius, droplet tail length and distance to the wing tip of the droplet were examined parametrically. The droplet parameters that were examined are shown in Figure 5.8. In the parametric study 250 analyses were performed.

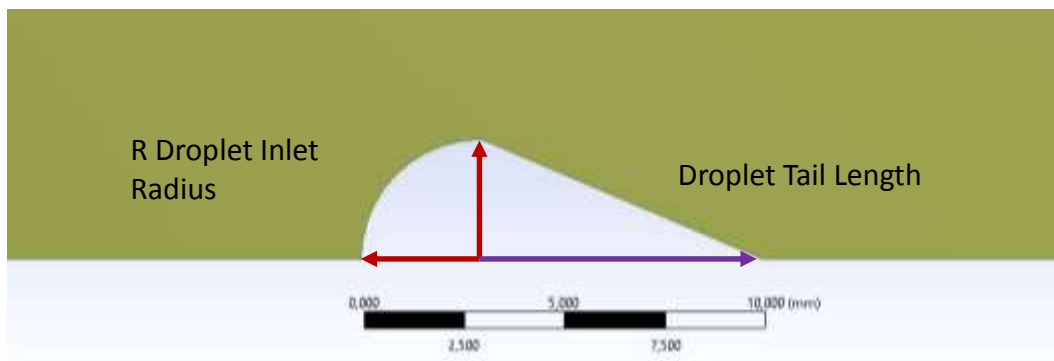


Figure 5.8 Rain drop parameters

The output parameters used to evaluate the result are the velocity drop and the turbulence kinetic energy. The turbulence kinetic energy is the energy that flow has due to vortices it contains.

The velocity drop is the velocity difference between the inlet and outlet velocities of the fan blade. It is aimed that the added droplet creates a minimum obstacle to the flow but creates a flow field with less friction between the flowing air and the wing with the generated flow structure. So, if the design is successful, the turbulence kinetic energy will increase slightly as the speed drop decreases relative to the flat wing. Table 5.2 presents the top 30 results in accordance with this goal.

As a result of the analysis made, the velocity drop of the flat wing without added droplet form was found to be -0.25 m/s and the turbulence kinetic energy was found to be 0.16 j/kg. When this result is compared with the results in Table 5.2, it is determined that the above condition is fulfilled. The velocity distribution map of the blade analysis with no droplet add-on is shown in Figure 5.9.

Table 5.2 Parametric CFD results of droplets

Droplet Position on Blade (mm)	Droplet Inlet Radius (mm)	Droplet Tail Length (mm)	Velocity Loss (m/s)	Turbulence Kinetic Energy (j/kg)
30,14667113	1,758059	9,956791	-0,219833	0,177869
31,05222702	1,694092	11,27179	-0,223807	0,178201
32,03165233	2,839967	10,00007	-0,234131	0,201611
30,40656936	1,038169	11,69622	-0,234469	0,170335
31,7245942	2,440885	8,409936	-0,23509	0,197011
32,49487786	1,209567	10,62729	-0,235322	0,170523
30,34242325	1,108366	9,590133	-0,236981	0,171425
33,8143396	1,492693	8,46325	-0,24299	0,176849
31,31386928	2,129608	6,140328	-0,251019	0,201434
36,35223508	2,307862	9,479422	-0,252863	0,187855
31,83244268	2,611185	7,085746	-0,253571	0,210356
37,64354165	2,300993	11,88838	-0,253604	0,184695
38,58907488	2,298742	10,69576	-0,259609	0,185554
36,07957488	1,120752	5,237569	-0,26179	0,174508
30,14107988	3,388342	7,578217	-0,269623	0,246208
45,93169282	1,012072	6,964794	-0,269855	0,171071
54,11590189	1,192994	10,89972	-0,271574	0,170904
54,15964599	1,002106	9,695892	-0,271646	0,169425



Figure 5.9 Velocity distribution map of the blade without droplet form add-on

In the parametric analysis using the wing with the droplet form, the diameter, tail length and position information on the wing were obtained for the droplet form having the minimum velocity drop and minimum turbulence kinetic energy. A droplet-form velocity distribution map with a droplet inlet diameter of 1.75 mm, a droplet tail length of 10 mm, a position wing center and a minimum velocity drop value is given in Figure 5.10.

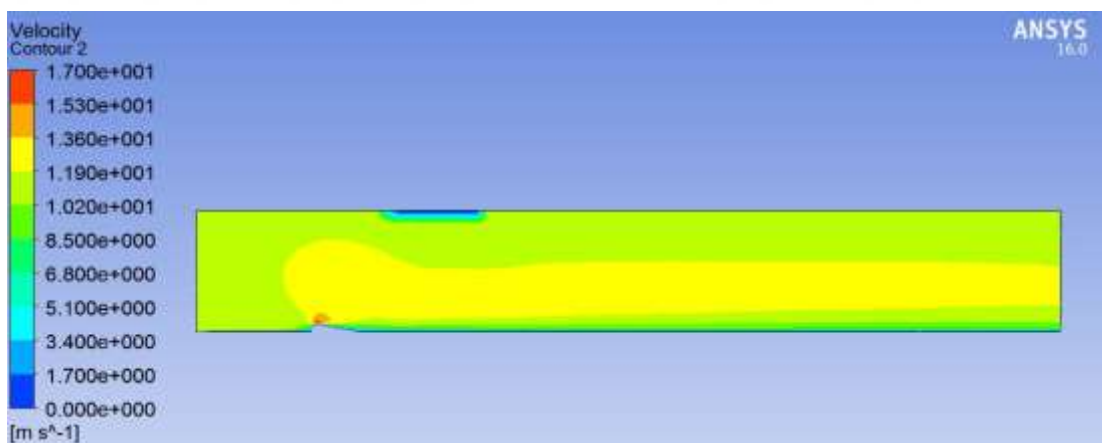


Figure 5.10 Velocity distribution map of the droplet design providing the highest performance as the result of the 250 analysis

The highest performance droplet form obtained from the analysis was added to the fan prototype named V4R1 and sound and flow tests were performed. The photograph of the fan and the droplet form used in the tests is given in Figure 5.11.



Figure 5.11 Fan prototype named V4R1 with added droplet form (Personal archive, 2015)

The newly designed prototype axial fan integrated to the newly designed SACOU. The photograph of the new SACOU is given at Figure 5.12. The test results of this prototype also given at the end of this chapter in the final comparison.



Figure 5.12 Final prototype of outdoor unit with axial fan (Personal archive, 2015)

5.2 Design of Split Air Conditioner Outdoor Unit with Cross-Flow Fan

The other product to be designed in the scope of this chapter of the thesis besides the axial fan SACOU examined in the previous section is the SACOU with CFF which is not commercially available in series.

As a beginning, the air flow rate needed for the design was evaluated. The indoor units which utilize CFF, generally have an air flow rate about 600~700 m³/hr. In outdoor units the air flow rate is about 1600~1800 m³/hr.

Although the difference seems to be very large, it must be noted that the indoor units has stricter constraints on the noise and the dimensions which the outdoor unit does not have. As the restrictions soften on the outdoor unit design, this difference will be reduced. Nevertheless, it has been decided to use two CFFs in the preliminary designs in order to guarantee the success of the design.

This will make it easier to achieve the desired result and design quieter outdoor units at lower speeds. Another advantage of the two-fan design is that it sucks air from three surfaces. Conventional external units can only be sucked from two surfaces.

Two preliminary designs were done in this way. The first of these was the "vertical positioning cross flow fan outdoor unit" design. This design is shown in Figure 5.13. The compressor for the movement of the refrigerant is located between the blowing openings of the two fans. Thus, it does not obstruct the flow surface as it is in conventional outer units.

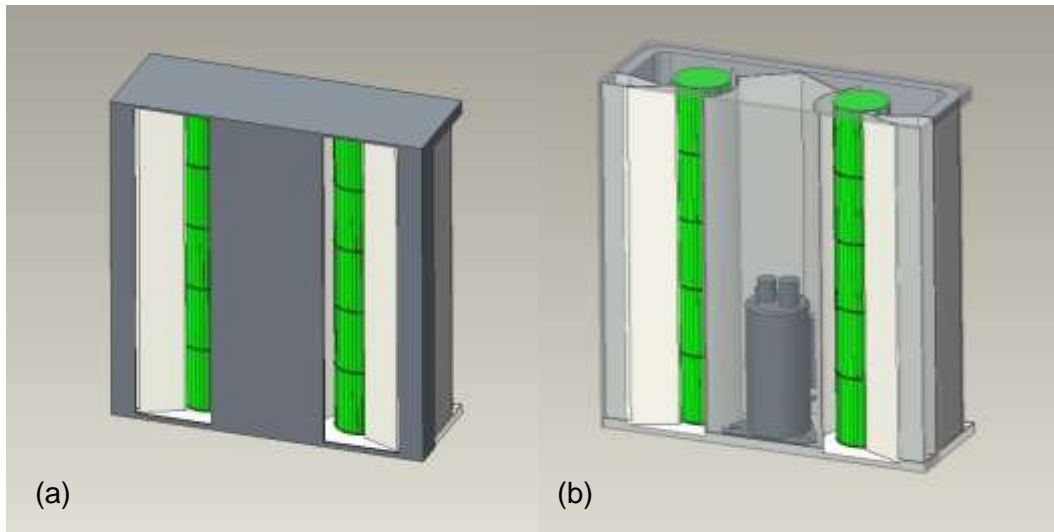


Figure 5.13 Outdoor unit with CFF in which the fans are vertically. a) Exterior view, b) Compressor positioning

The second design, which is designed as an alternative to this design, is "an outdoor unit with a CFF where the fans are positioned horizontally". In this design, the space between the fans is not suitable for the placement of the compressor, so a separate section has been created for the compressor. In the other design; right, left and rear suction is realized in the bottom, top and back of this design.

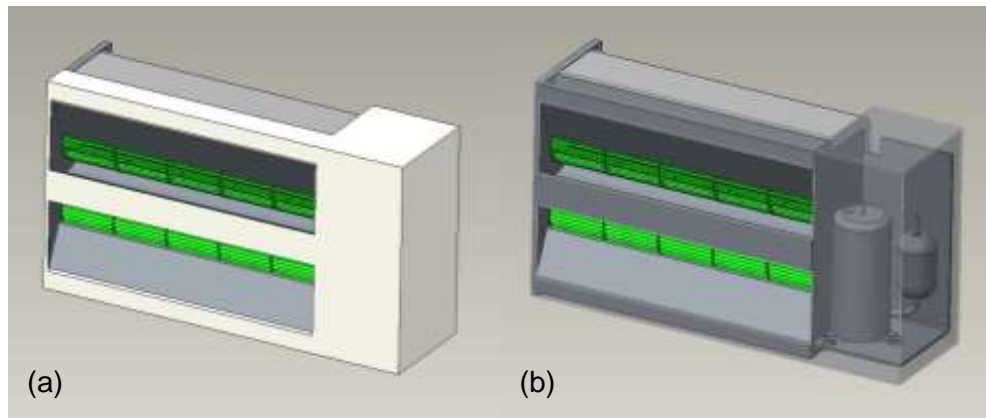


Figure 5.14 Outdoor unit with CFF in which the fans are horizontally positioned a) Exterior view, b) Compressor positioning

As two models compared, it is considered that the vertical model can be more advantageous in terms of suction when the outdoor unit is placed on the ground. Furthermore, the fact that the compressor can be placed in the gap between the two

fans in vertical model, it allows a smaller outdoor unit to be produced. Finally, in the vertical design, the sub-base is a single piece so that it will form a solid carrying floor, while the horizontal design requires a wide opening in the bottom plate that carry the system in order to ensure suction of the fan.

It can be said that vertical design is more advantageous in all these evaluations. With the completion of the preliminary design and evaluation, the digital models of the draft design have been developed.

5.2.1 Numerical Model and Parametric Analyses

Following the completion of the preliminary designs made, the numerical models of the created draft designs are started to be created. Two-dimensional model with the aim of shortening the analysis period has been preferred in order to carry out multiple analyses in the development of designs.

The model's air volume is modeled to be 20 times the fan diameter. This modeling method is accepted in the literature in the modeling of a crossflow fan (Kumlutaş, Karadeniz & Kuru, 2013). This expanded air volume is used both in the suction zone and in the blow zone.

These wide openings are not in actual condition as the system wall hangs under normal operating conditions. However, this wall effect is not taken into consideration in laboratory tests that are in accordance with the standards. The verification process is modeled according to these tests so that the numerical model is compared with these laboratory tests. The effects of wall influences on the performance of the unit can also be examined. Numerical model of air volume is given in Figure 5.15.

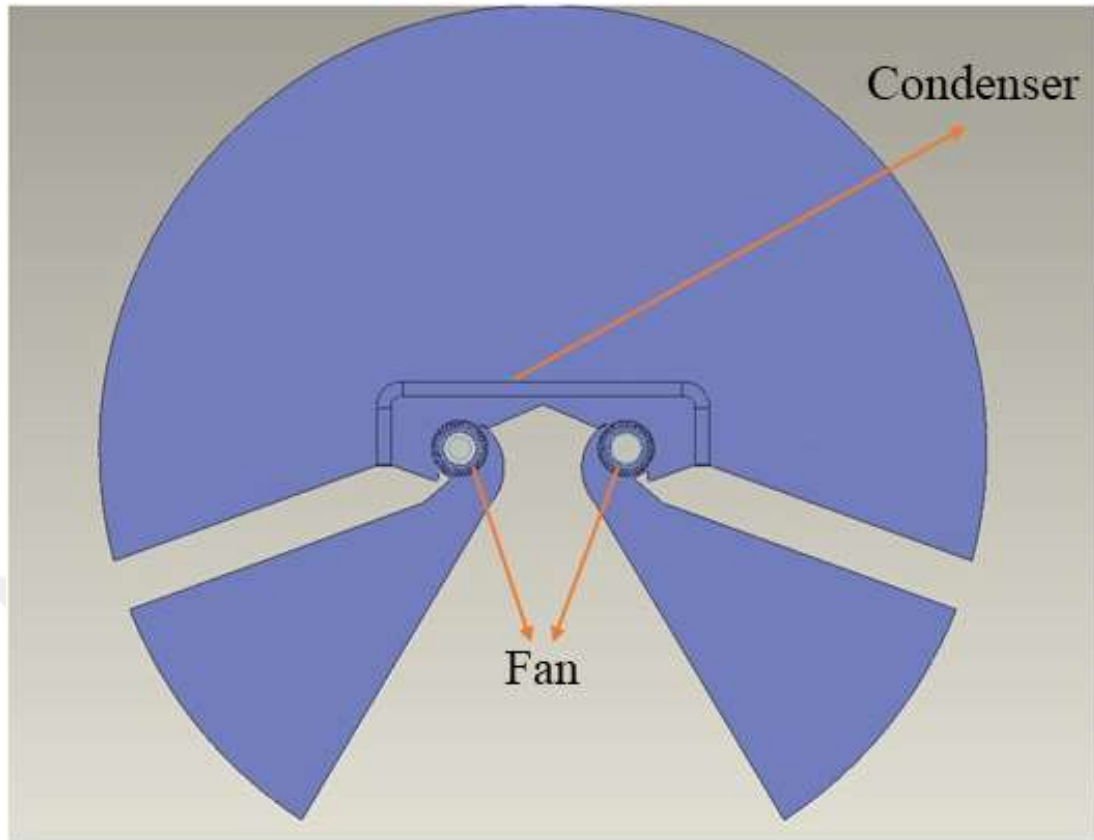


Figure 5.15 Air model for CFD

During the meetings with the company. The parameters to be examined through the preliminary design created in the device and their inspection intervals are determined. Since the model is symmetric in terms of the shortening of the analysis period. The parametric analyses are completed through the half model. These parameters are specified in Table 5.3 and shown in Figure 5.16.

Table 5.3 Parameters and inspection interval

Parameter Name	Inspection Interval
L_1	155 mm – 180 mm
L_2	90 mm – 125 mm
Ω	15° - 21°

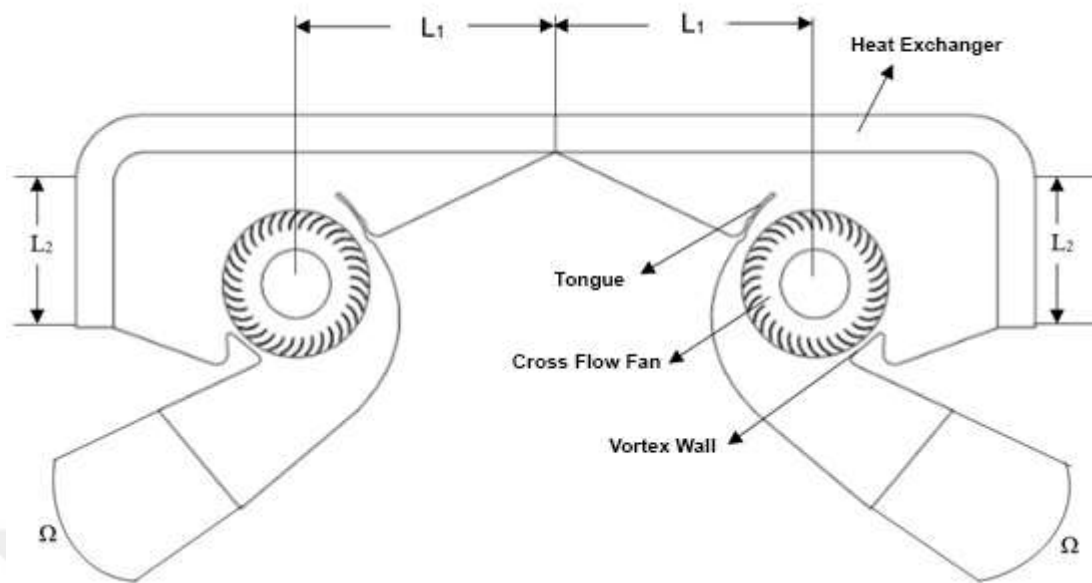


Figure 5.16 Schematic of the parameters examined on the outdoor unit design with CFF

In the preliminary design, the distance between the two fans ($2L_1$) determined by considering the fan's rear back geometry and the position of the condenser is taken as 150 mm. In the parametric study, the length of L_1 was changed and examined. Therefore, the effect of this parameter on the flow was investigated by increasing the distance between the two fans by 20%.

L_2 is the depth of the outdoor unit and the heat exchanger. This dimension, designed as 102.5 mm in the preliminary design. Its range modified in the range of -12% and +22%. The effects of these modification on the flow has been investigated.

Ω is the blowing angle. This angle, which was determined as 17° in the preliminary design, was scanned from -13% to +23% and the effect on the flow field was examined.

When the parameters are taken into preliminary consideration. L_1 , L_2 expand the dimensions of the product, the suction area and the heat exchanger dimensions. Ω widens the outlet opening while not affecting product dimensions.

Two output parameters have been determined for the evaluation of these parameters. These are the total pressure coefficient (Ψ_t) and the flow coefficient (ϕ). These two coefficients are the dimensionless numbers used in evaluating the performance of the crossflow fans. The formulas are presented below (Lazzaretto & Martegani, 2001).

$$\Psi_t = \frac{p_t}{\frac{1}{2}\rho u_2^2} \quad (5.1)$$

$$\phi = \frac{q_v}{LD_2 u_2} \quad (5.2)$$

In the Equation 5.1. P_t [Pa] is the total pressure, ρ [kg/m^3] is the density of the fluid and u_2 [m/s] is the linear velocity of the outer diameter of the crossflow fan. In the Equation 5.2, q_v [m^3/s] is the volumetric flow rate. L [m] is the total length of the fan (depth according to Figure 5.16), and D_2 [m] is the fan's outer diameter. The result of the CFD analysis is given in Table 5.4.

When evaluated in Table 5.4. The increase of the flow coefficient indicates that the device will give higher flow rate. The increase in the total pressure coefficient represents how far the device will push the fluid. The further push of the conditioned air prevents the air from being sucked back into the unit, thus making the system more comfortable to operate. Sorting in Table 5.4, flow coefficient. Analysis results are presented in Figure 5.17, 5.18 and 5.19.

In terms of the flow coefficient, design number 17 has the highest success. On the other hand, design number 20 gives the highest value as the total pressure coefficient. When the output parameters are evaluated together, the numbers 20 are designed, which is a little behind the 17th flow rate, is chosen as the prototype to be produced because of its very high pressure advantage. The velocity distribution obtained from the numerical analysis of the selected prototype 20 is shown in Figure 5.17. The pressure distribution is given in Figure 5.18 and the vorticity distribution map is given in Figure 5.19.

Table 5.4 Results of the parametric CFD analyses

Design Number	Ω (degree)	L_1 (mm)	L_2 (mm)	Total Pressure Coefficient. (Ψ_t)	Flow Coefficient. (ϕ)
17	15.627	156.410	90.348	0.607	1.395
11	16.400	179.167	107.500	0.629	1.379
5	15.200	159.167	105.167	0.594	1.353
30	18.156	155.149	124.992	0.568	1.343
13	18.000	155.833	100.500	0.519	1.343
<u>20</u>	<u>15.016</u>	<u>176.605</u>	<u>97.431</u>	<u>0.676</u>	<u>1.336</u>
21	15.002	155.169	119.392	0.575	1.332
3	15.600	170.833	114.500	0.575	1.325
2	17.200	175.833	93.500	0.491	1.314
12	16.000	167.500	98.167	0.640	1.296
19	15.573	179.365	124.100	0.314	1.269
7	18.800	164.167	91.167	0.294	1.246
15	16.800	160.833	121.500	0.267	1.244
24	20.999	171.309	106.387	0.188	1.227
10	17.600	172.500	123.833	0.233	1.215
28	18.881	179.376	124.675	0.261	1.214
6	20.800	162.500	102.833	0.160	1.211
22	15.016	165.801	124.738	0.286	1.207
14	19.200	177.500	112.167	0.147	1.203
9	18.400	165.833	109.833	0.299	1.200
27	17.126	155.494	111.494	0.249	1.200
26	18.921	164.455	123.458	0.192	1.197
29	18.203	173.310	103.420	0.224	1.194
18	20.955	179.866	124.837	0.148	1.190
16	20.414	155.126	90.316	0.198	1.148
4	19.600	157.500	116.833	0.168	1.136
1	20.000	174.167	95.833	0.095	1.126
8	20.400	170.000	119.167	0.097	1.104

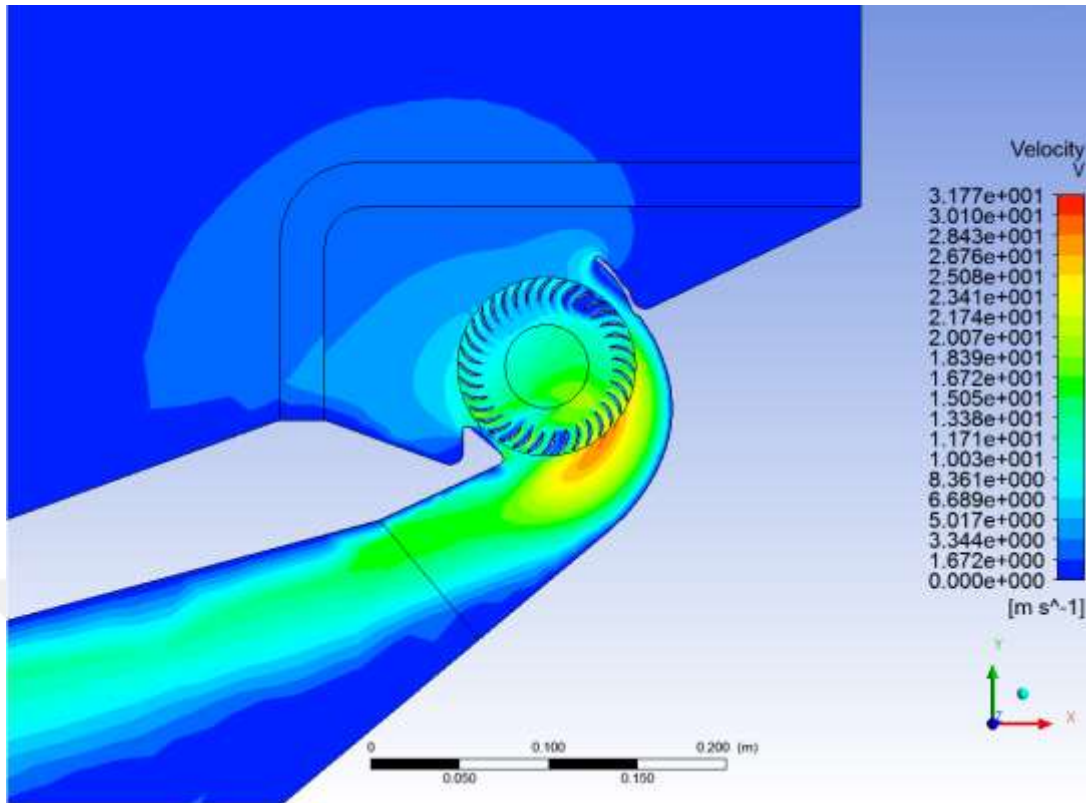


Figure 5.17 Velocity distribution map of design number 20

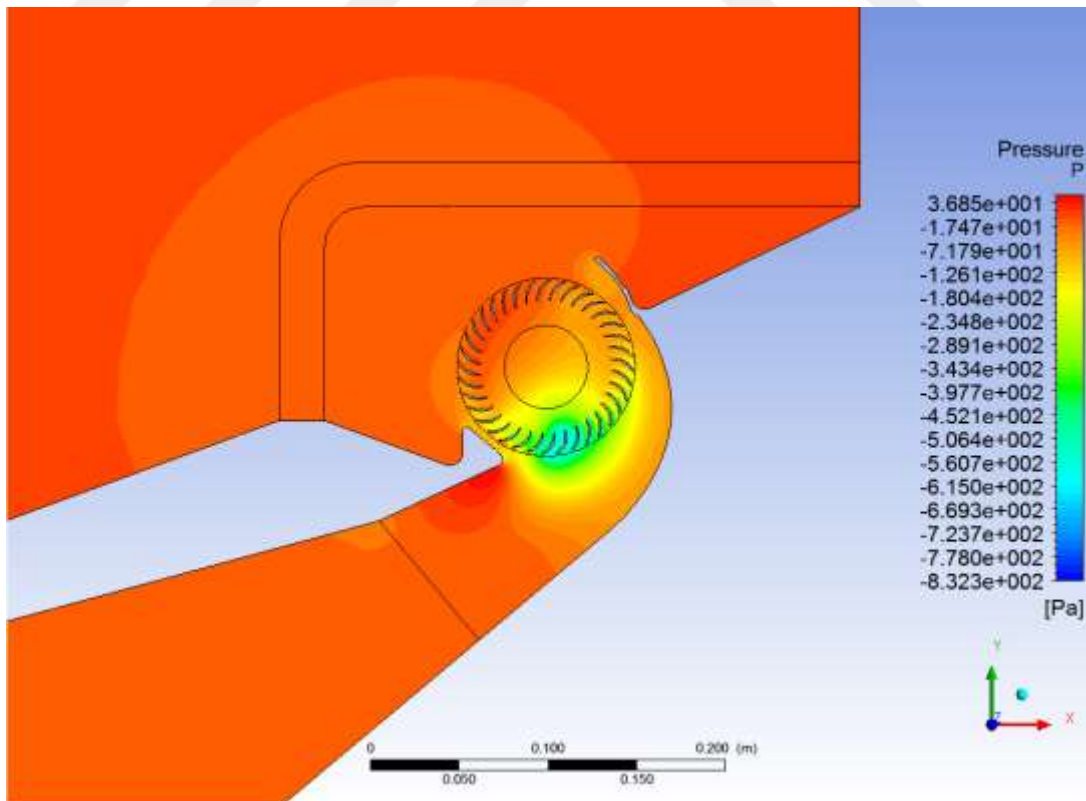


Figure 5.18 Pressure distribution map of design number 20

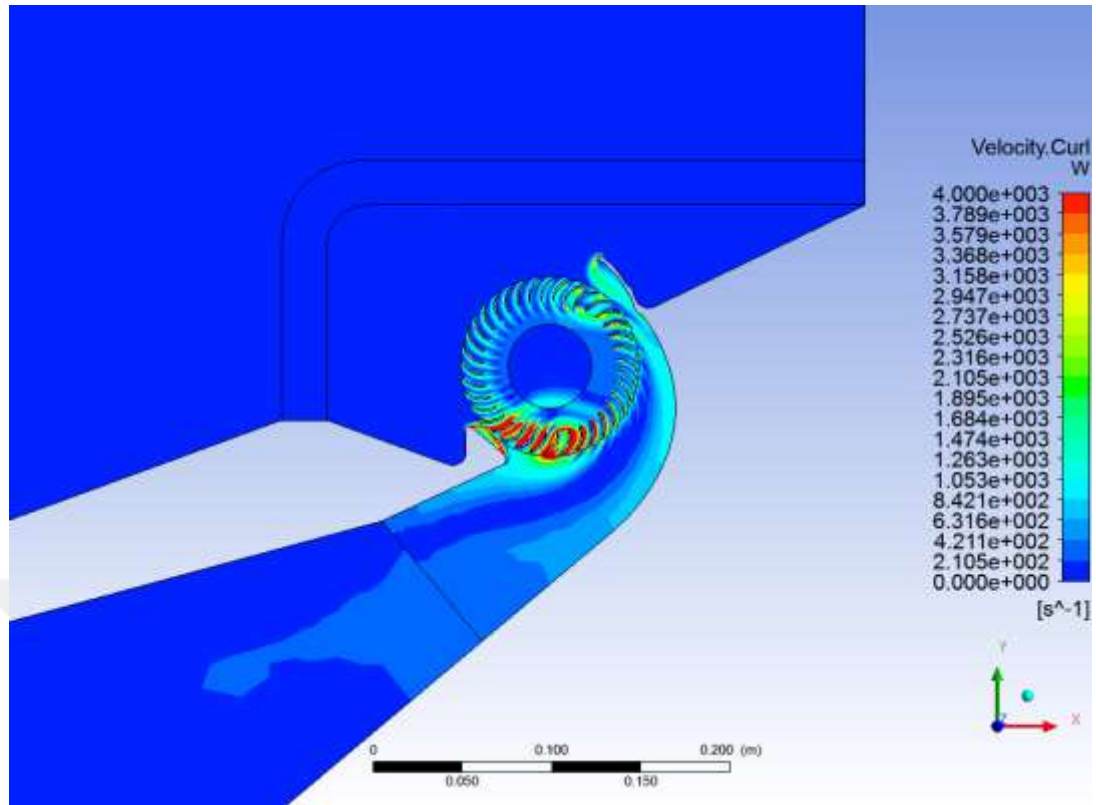


Figure 5.19 Vorticity distribution map of design number 20

In Figure 5.17, the jet flow generated by the crossflow fan is observed in a literature-compatible manner. The average speed of the device suction is 2.044 m/s and the speed at the outlet is 8.806 m/s. When the pressure distribution map in Figure 5.18 is examined. Low pressure area in which the eccentric vortex exists is in accordance with the working principle of the CFF. It appears to be at the vortex wall. The presence of this vortex is also observed in the vorticity distribution map in Figure 5.19. Certain vortex fields are formed in the upper and lower parts of the jet. These fields formed due to jet contacting the channel walls and slowing down. This consideration can be seen clearly as the Figure 5.17 and Figure 5.19 examined together.

In general, when three figures are evaluated, a flow is separated in the tongue part and pressure drop is observed accordingly. However, since the studies related to the tongue carried out experimentally. Apart from this, no aerodynamic defect that creates velocity drop or vortex, was detected.

CFD analysis were completed and design alternative 20 was selected as the most successful design. Its prototype was produced.

5.2.2 The Production Process of the Split Air Conditioner Outdoor Unit Prototype with Cross Flow Fan

After obtaining the general design parameters of the device, the production of the SACOU prototype with CFF has been started.

The design parameters which were not inspected in the parametric CFD study such as back geometry, swirl wall position, swirl wall fan distance ... etc. were decided by using the experimental method explained at Chapter 3. However some validation experiments were done. The prototypes used in this experiments were given at Figure 5.20.



Figure 5.20 The CFF cut of prototypes used for endoscopic PIV (Personal archive, 2016)

As mentioned, the prototypes shown in Fig. 5.20 were developed by adapting the parametric prototype for the inner units to the CFF outdoor unit. The model is made three fan module height of the crossflow fan for a clear investigation with PIV method. In prototypes production, a 3D Printer was used in the company. The tongue angle in

the prototypes were examined. The results of this study are compatible with the study done in Chapter 3. (Fan modul: One of the main advantages of CFFs is that the length of the fan can be arranged according to the required design. However, the blades of the fan are subjected to buckling due to the torque after a certain length. In order to prevent this, flange-like structures are added to the CFFs at regular intervals. Between these two structures is called a fan modul.)

In Figure 5.21 the results of the experimental study on tongue angle is given. In the prototypes produced, the variation of the angles of the tongues for different sizes and flow cross sections was investigated. The zero position of the tongue angle has been chosen so that it continues the tongue geometry. The positive values are that the language has moved away from the fan. The negative values are the geometries that the tongue approaches to the fan.

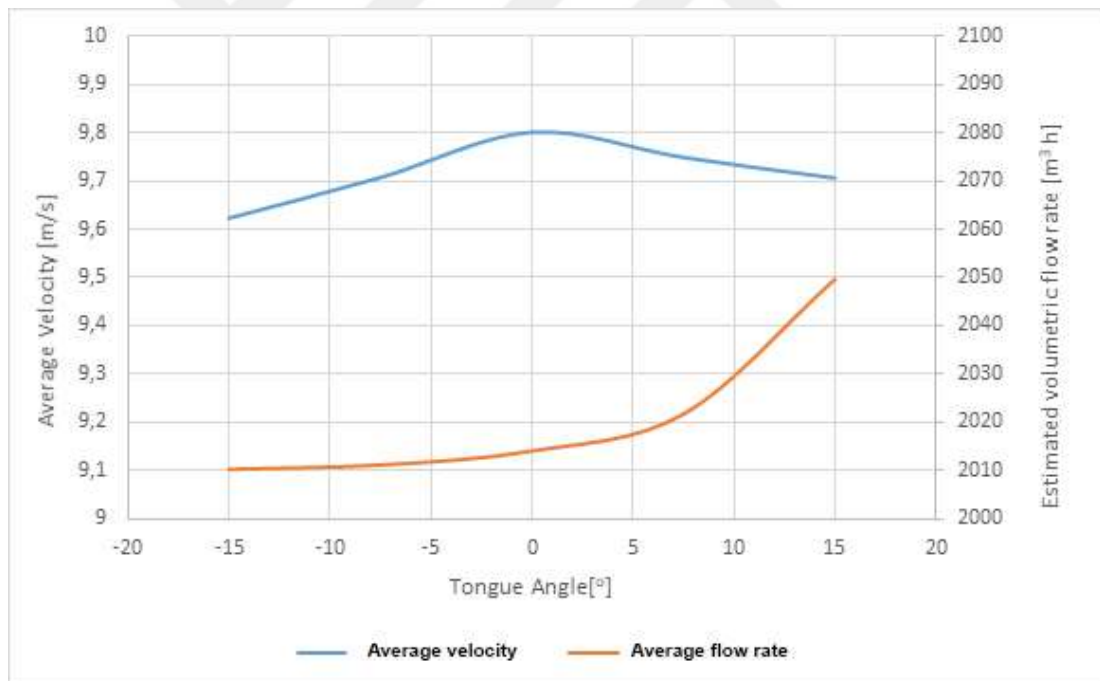


Figure 5.21 The effects of tongue angle on estimated volumetric flow rate and average velocity

If the language angle decreases to negative values, the flow field narrows due to the fact that the tongue is too close to the fan, and accordingly both the average speed and the average flow rate are reduced. The highest average speed is obtained for the zero position of the tongue. When the language angle goes to the surplus value, the flow

rate increases even more because of the channel expansion, but the average speed is somewhat reduced. Nevertheless, when the results obtained are evaluated dimensionally, it can be said that they do not make great differences in terms of design as well as being within the difference of measurement accuracy. These can be observed in Figure 5.21.

After the completion of the validation experiments, the production of the full prototype was started.

Elements such as heat exchangers and compressors to be used in this design are produced or supplied by the company itself. The remaining parts of the system were produced in a subsidiary industry prototype company. The image of the prototype is given at Figure 5.22 and Figure 5.23.



Figure 5.22 Front view of the prototype of the outdoor unit with CFF (Personal archive, 2016)

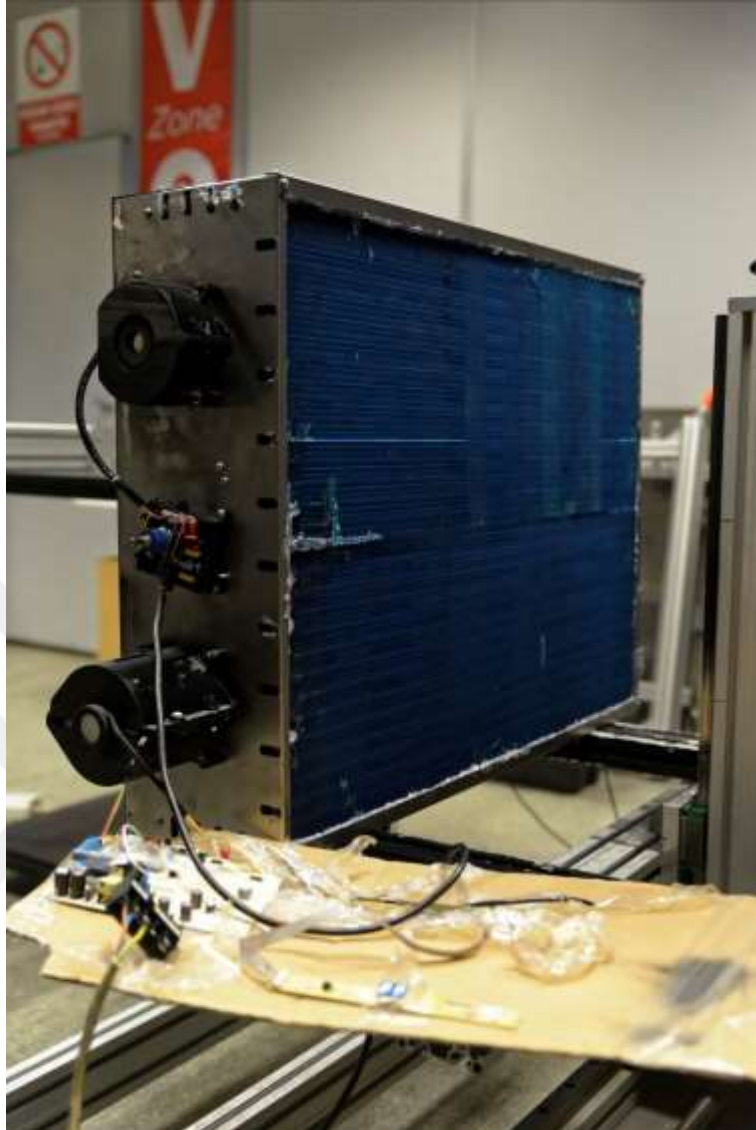


Figure 5.23 Rear view of the final prototype of the outdoor unit with CFF (Personal archive, 2016)

After obtaining the final prototype, the prototype was examined experimentally.

5.2.3 Investigation Experimental of the Cross Flow Fan Outdoor Unit Prototype

In this context, the flow structure of the prototype has been investigated by the PIV method. In addition, air flow rate and sound tests were performed on the device using the test rooms in the company.

The flow structure of the crossflow fan was investigated volumetrically by the Stereo PIV experiment. The image recorded during the experiment is given in Figure 5.24.



Figure 5.24 Investigation of prototype of outdoor unit with CFF by SPIV method (Personal archive, 2016)

The scanning method described in chapter 2 is used to perform the volumetric investigation. In this method, two cameras were taken 200 Image Couple (400 images per camera) from the selected planes along the blowing mouth of the device. Then two dimensional two-component velocity distribution map was obtained by processing these images. After that, the average of this 200 velocity distribution map is created for every measurement plane. The use of dual cameras during experiments ensures that the third dimension components on the plane can also be measured. So average planar three component velocity distribution maps were obtained by processing the velocity maps from both cameras by calibration data. Planar mean three-component velocity distribution maps obtained from the mentioned planes are given in Figure 5.25.

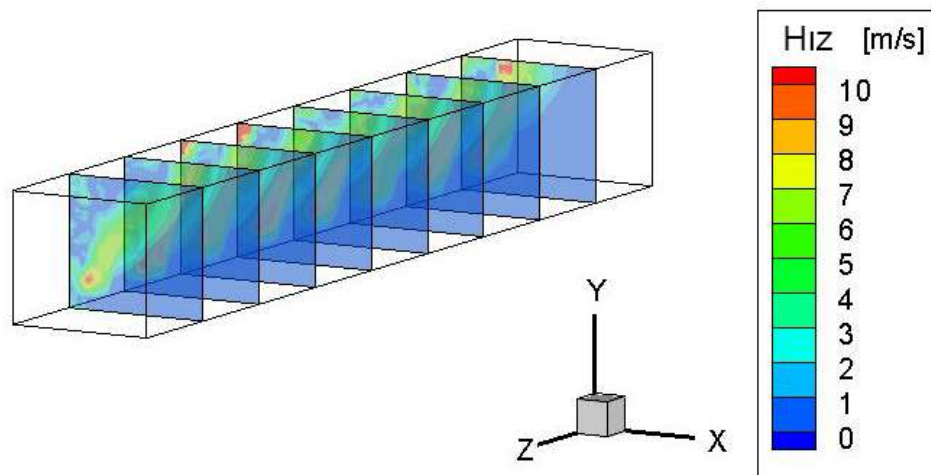


Figure 5.25 Planar mean three-component velocity distribution maps

In order to obtain the volumetric flow distribution, the data obtained from the planes is interpolated. The interpolation resultant flow distribution is shown in Figure 5.26.

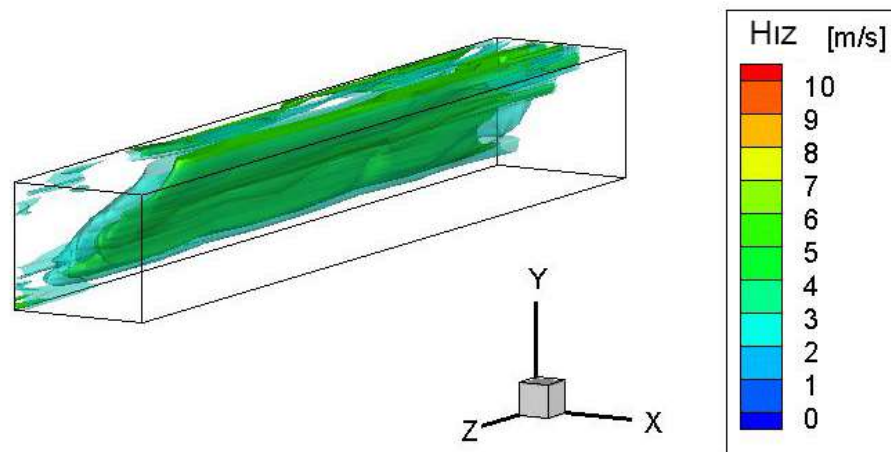


Figure 5.26 Velocity isosurfaces of volumetric average three component flow field of CFF obtained by PIV (3-5 m/s)

When the obtained volumetric flow distribution map was examined, it was observed that the jet flowed out of the device with a smooth, consistent profile along the flow mouth. In accordance with the analysis made in the previous section, it was determined that the lower jet flow does not affect the upper jet flow. This confirms once again the acceptance of symmetry in the previous section.

Sound and flow tests were performed after the completion of the stereo PIV experiments. The results of the tests made are given in Figures 5.27 and Figure 5.28.

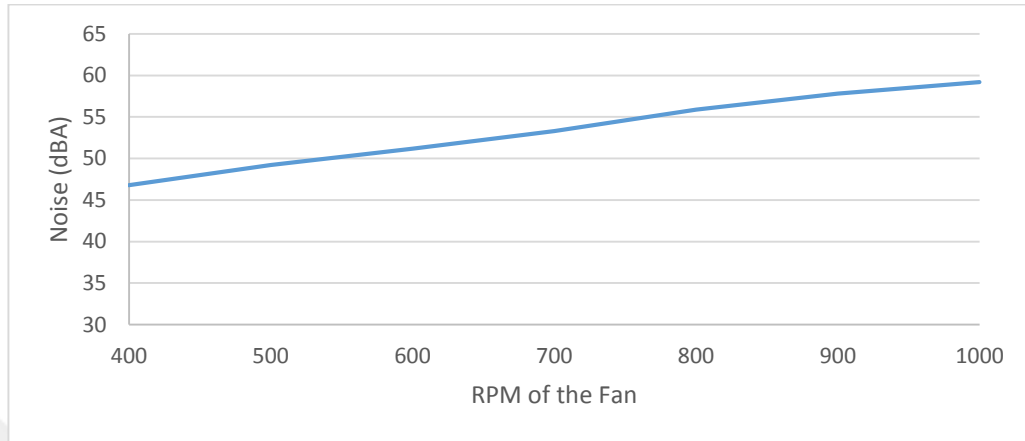


Figure 5.27 Noise test results of the outdoor unit with CFF

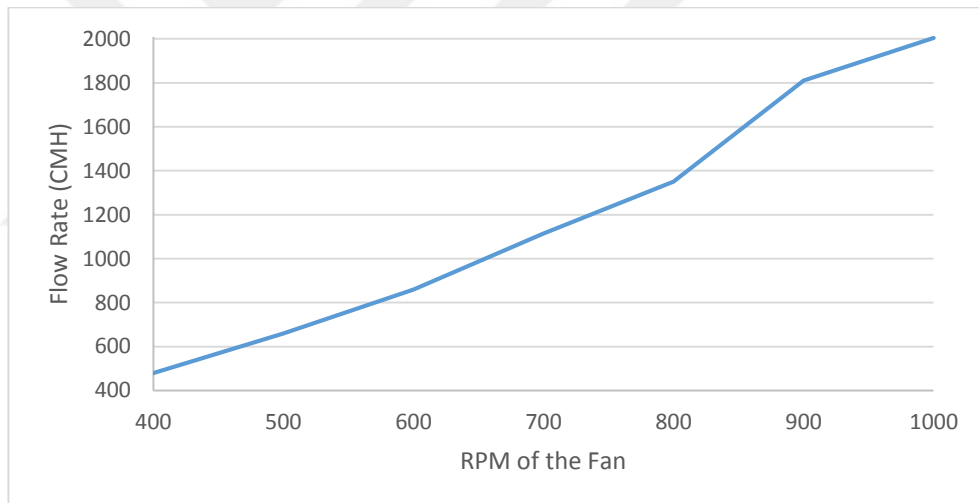


Figure 5.28 Air flow rate test results of the outdoor unit with CFF

In accordance with the other studies carried out within the scope of this thesis and the literature, it has been observed that as the Round per Minute (RPM) increase, the air flow rate and the noise also increases naturally.

The important question is, is this increase and the obtained values are better than the axial fan outdoor units. This evaluation was made in the following section.

5.3 Comparison of Outdoor Unit with Axial and Cross Flow Fan

After the completion of the outdoor units with axial fan and CFF, the comparison of these two prototypes has been started. The existing product was also added to the comparison for evaluating the improvement of the two devices.

The first comparison which is air flow rate-RPM graph is presented in Figure 5.29. When the graph is examined, the improvements on the nozzle, the grid and the fan design have been to be a serious improvement effect on air flow rate per RPM. This effect increases even more effective at high speeds. The average flow rate gain is 14.17%. The flow rate gain at 800 RPM is 17.9% which the device is working predominantly.

Another element to be examined in Figure 5.29 is the outdoor unit prototype with CFF. It can be seen from this graph that the air flow rate per RPM is rather low. But the fact that the geometries and working principles of the fans are completely different is a fact that should not be overlooked. For example, the diameter of the axial fan used in the system is 400 mm. the diameter of the CFF is 100 mm. When the fan's linear velocity is evaluated on this information, the same central axial fan rotates the fan four times faster. From this point of view, it is expected that the number of flow per cycle is higher in axial fans. Therefore, the information on the cross-flow fan outdoor unit in this chart is presented in terms of transparency.

The second comparison of the axial fan model and the CFF prototype is a Noise-Air flow rate comparison. In this comparison, the noise per unit flow rate is examined. Normally it is expected that the noise increases with air flow rate. The graph of this comparison is given in Figure 5.30.

When assessed in Figure 5.30, it is observed that the fan named V4R1, produces the lowest noise per flow rate. When the performance of the prototype of the outdoor unit with CFF is evaluated, it is determined that the device works with the least noise till 1600 m³/h air flow rate. This advantage lost at higher flow rates.

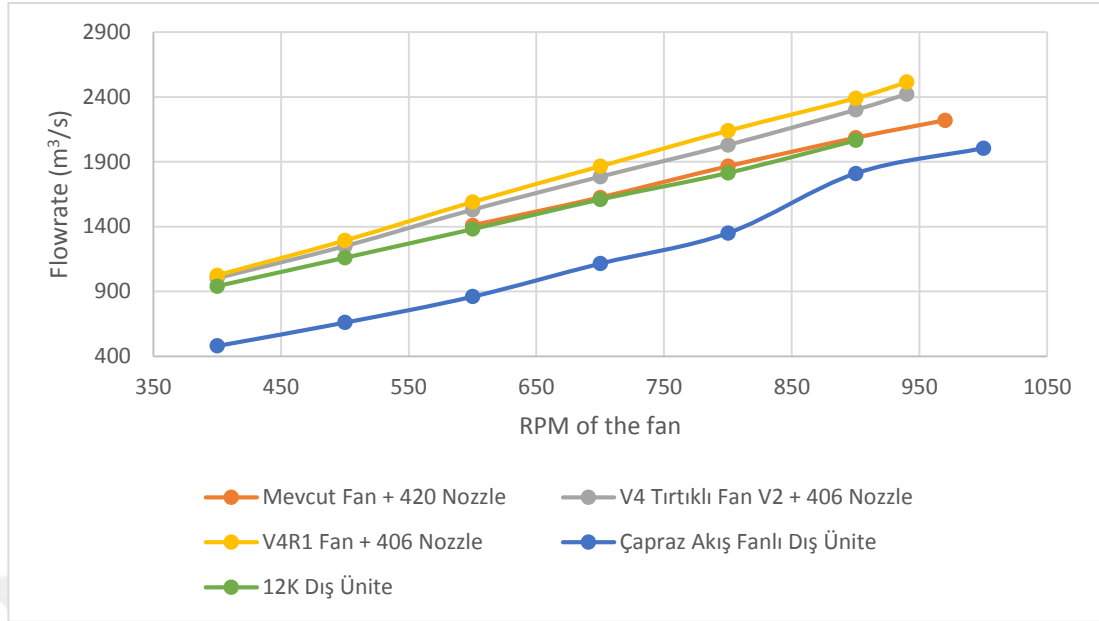


Figure 5.29 Air flow rate-RPM chart

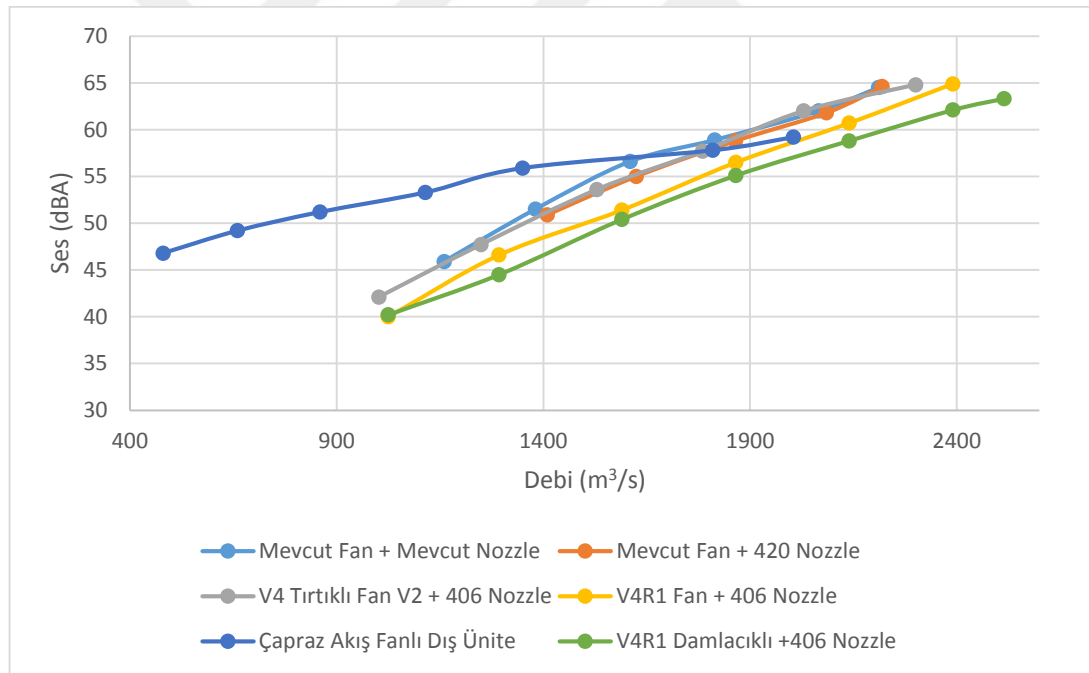


Figure 5.30 Noise-Air flow Rate comparison chart

When all the results are evaluated; it was determined that the new axial fan outdoor unit designed within the scope of this thesis's average air flow rate is 14.17% higher than the existing outdoor unit and 17.9% higher in the working cycle. The advantage of this air flow rate allows the fan to achieve the desired output at lower speeds. Thus, the outdoor unit with a new axial fan has 2.43 dBA lower sound level than the current

outdoor unit at the need air flow rate. In the case of maximum air flow rate demand in the eastern provinces, this difference is up to 4.66 dBA. In the direction of these results, studies were started by the company about the mass production of the newly designed axial fan outdoor unit.

The prototype of the outdoor unit with a CFF has successfully met the lower sound expectation, which is the forecast for the beginning of the project. Although the new axial fan outdoor unit developed within the scope of the project has higher success than the outdoor unit with CFF, the outdoor unit with CFF offers potential for low noise SACOU.



CHAPTER SIX
IMPROVING THE DESIGN OF WASHING MACHINE WITH DRYING
FEATURE AND INCREASING ITS EFFICIENCY

This part of the thesis consists of the works done on the SANTEZ project encoded with 00998.STZ.2011-2. This project aimed to improve the design of the dryer washing machine and to increase its performance in line with customer requests and expectations. The flow structure of the air directed by the fan in the washing machines were investigated for improving the process of designing the fan and dryer system.

6.1 Particle Image Velocimetry Experiments at the Output Section of the Centrifugal Fan

Reviewing the current system, the first component to be investigated is the fan of the drying system. The laser is placed to the exhaust mouth of the fan perpendicularly. The camera is placed to view the laser plane perpendicularly.

Table 6.1 Locations of the measurements planes

Plane Number	Distance to Origin (mm)	Plane Number	Distance to Origin (mm)
1	0	16	63
2	4,5	17	68
3	9	18	72
4	13,5	19	77
5	18	20	80
6	23	21 (2nd Edge)	82,5
7	28,5	22	86,5
8	31	23	90
9 (1st Edge)	34	24	94
10	37	25	98,5
11	41	26	103
12	45	27	107
13	49	28	112
14	53,5	29	116,5
15	58,5		

Measurements were taken from 29 different planes at the output mouth of the fan. In order to fully capture the flow structure, the scan area of the measurement points are taken larger than the mouth section. The locations of the measurements are

specified in Table 6.1. The edges are marked. The zero point is selected on the points far from the camera. The photography of the experiment is given in Figure 6.1.

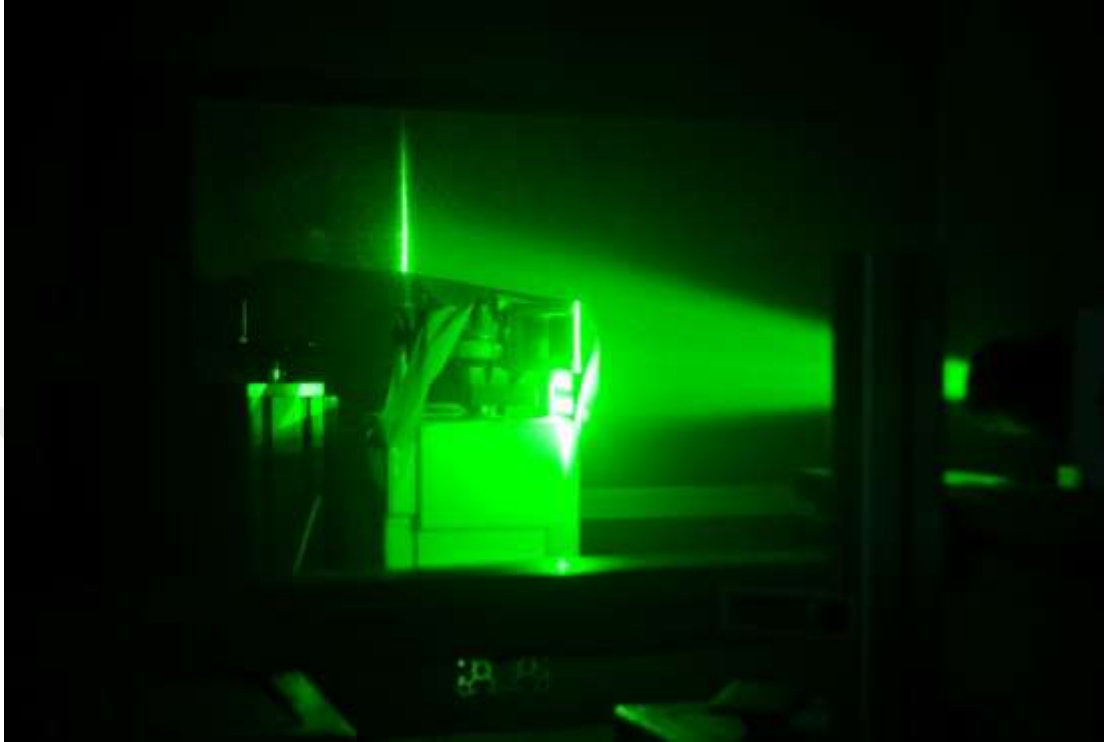


Figure 6.1 The photograph of the PIV experiments conducted at the output mouth of the centrifugal fan (Personal archive, 2012)

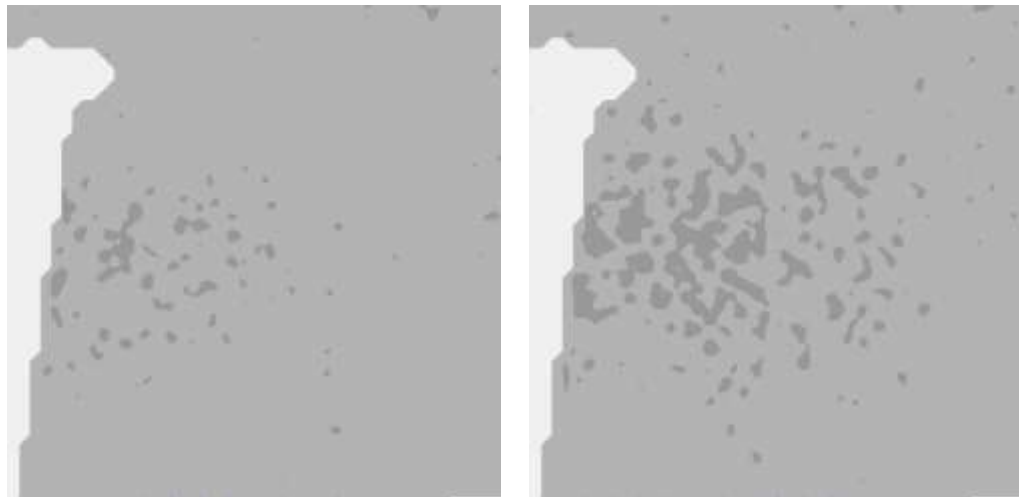
The first laser plane is created 30 mm right of the output mouth of the centrifugal fan, on 0 mm point and following conducting experiments on the planes specified in Table 6.1, the laser plane is shifted. 200 image couples were recorded with 2 cameras from each plane. The 3D vector maps of these measurement planes are given in Figure 6.2. They are evaluated by taking the averages of the 200 instantaneous vector maps obtained from each camera. Then they are converted to 3D by using the calibration data. This data forms a temporal average of the flow which is suitable to compare with the steady state solutions that used in numerical studies.

In Figure 6.2 the vectors specify the velocities in measurement planes, the gray background specifies the out of plane velocities. The black sections indicate the vectors toward the viewer, the white sections indicate the vectors travelling at the opposite direction. In order to ensure greater visibility for vectors, on the maps where

out of plane velocities are higher, the vectors are indicated as yellow, however in other visuals they are indicated as blue. This difference in color does not have further indication than easing the review.

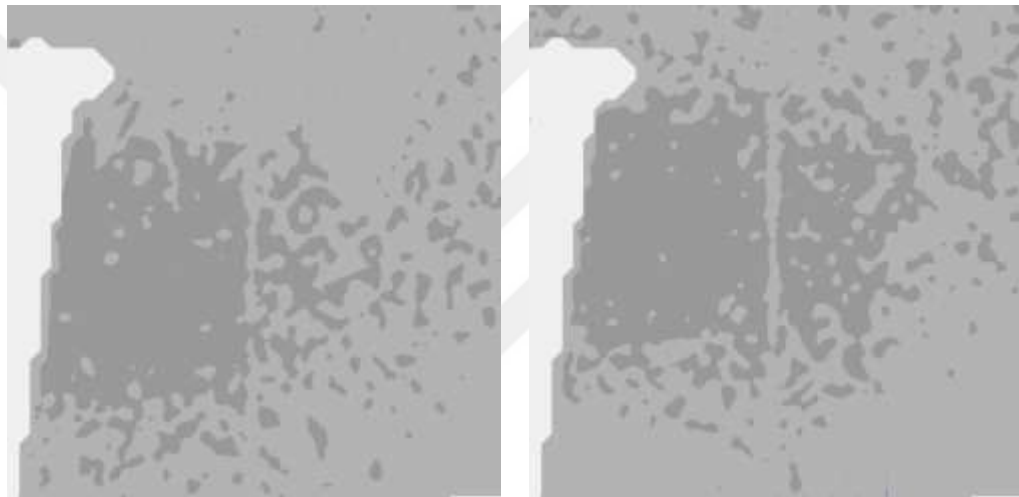
When the first 8 vector maps are reviewed it is seen that the velocities are under 1m/s. The reason behind this is the centrifugal fan flows are outward from the center. On measuring point 9, at the measurement point where the fan is initiated, the velocity of the flow starts to increase. Up to the experiment point 21 (the 2nd edge) output velocities up to 12 - 15 m/s are measured. As these measurement points are investigated it should be noted that the out of plane velocities are high as well.

It is also observed that on the measurement planes further than measurement point 21, the high velocity vectors initiate further from the output mouth. The reason behind this is the flow entering the investigation plane from the prior plane due to out of plane velocity component. Therefore, as the further measurement planes are investigated, the initiation point of the vectors is shifted further.



(1)

(2)



(3)

(4)



(5)

(6)

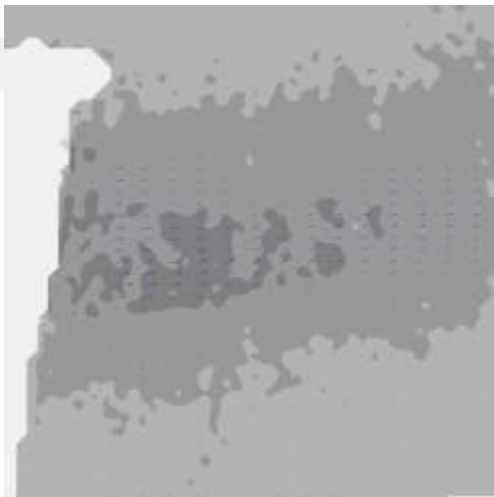
Figure 6.2 3D vector maps compiled from PIV experiments



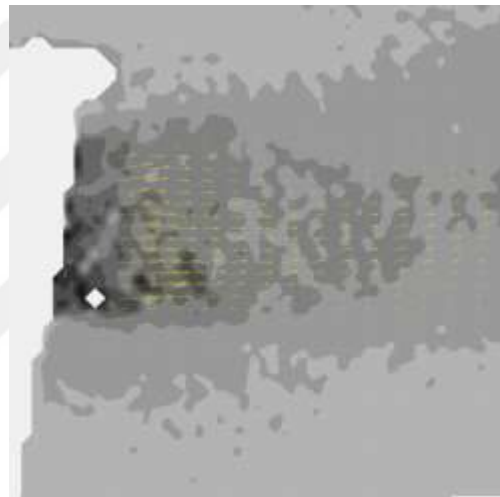
(7)



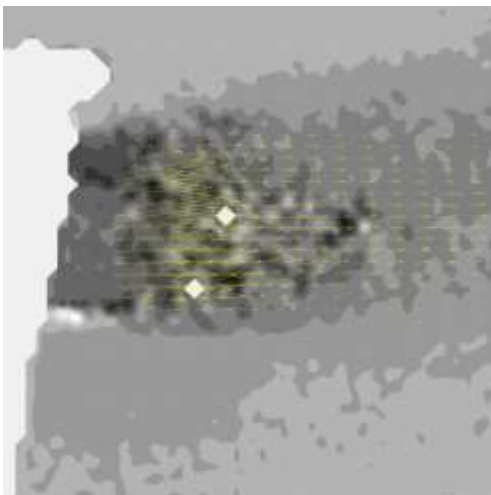
(8)



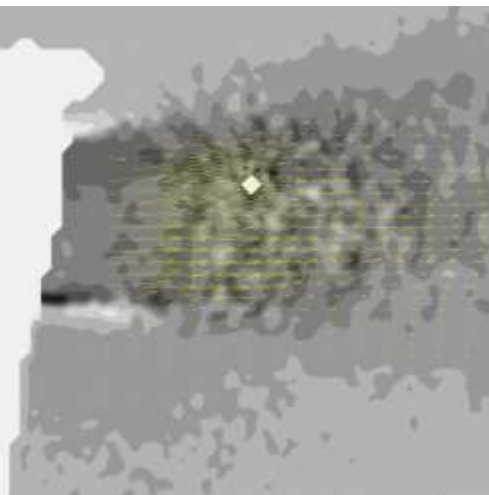
(9)



(10)

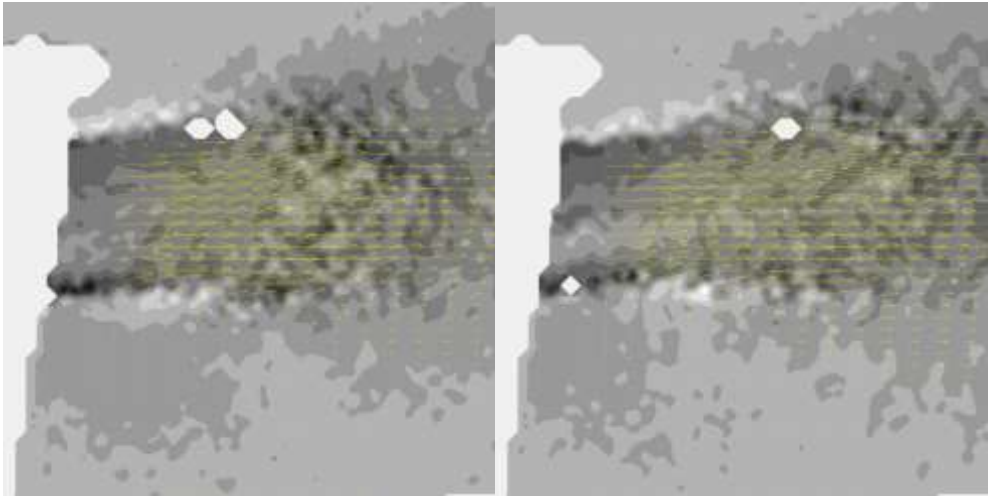


(11)



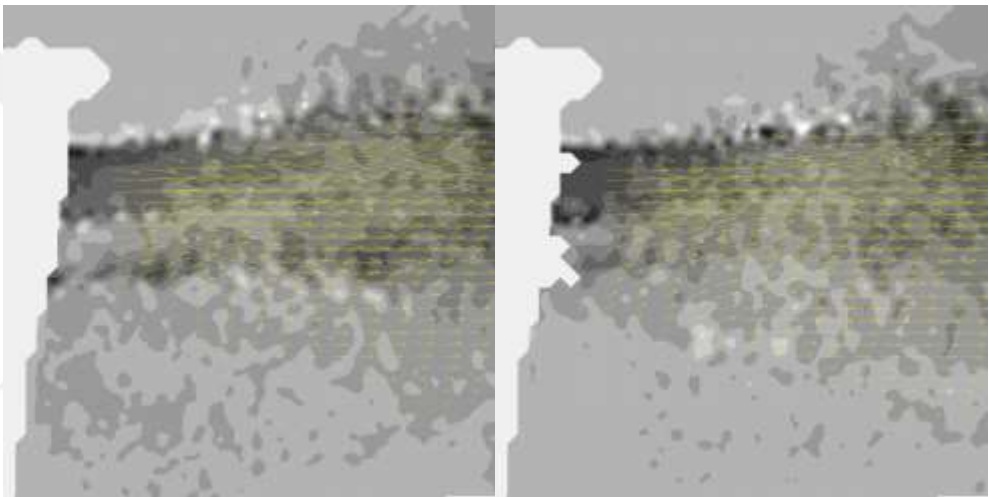
(12)

Figure 6.2 continues



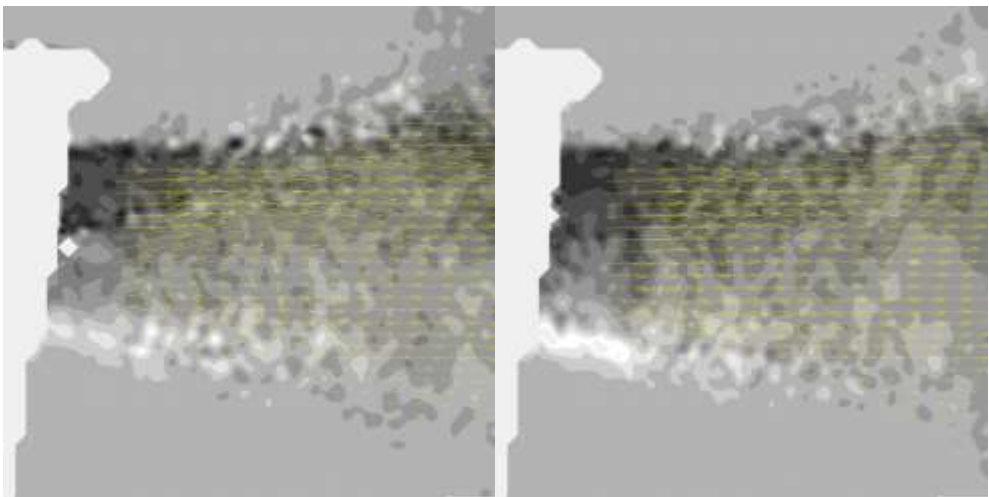
(13)

(14)



(15)

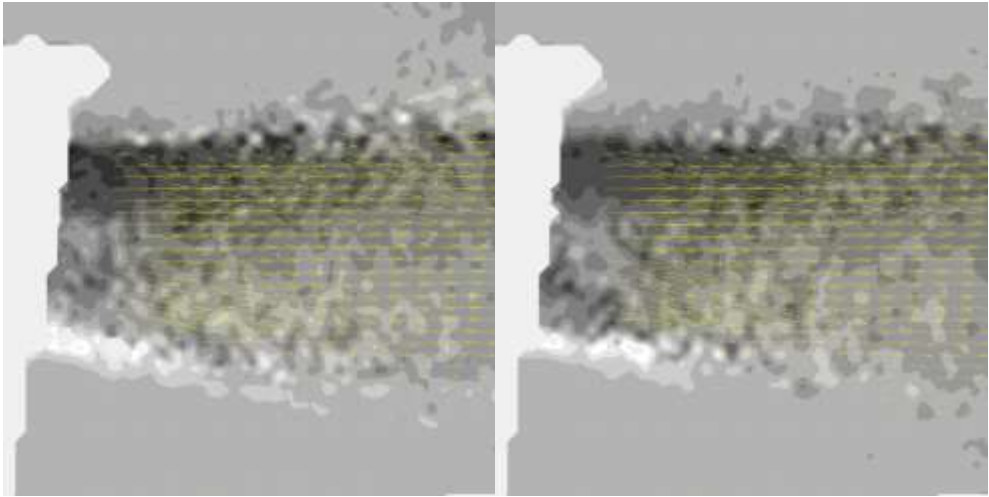
(16)



(17)

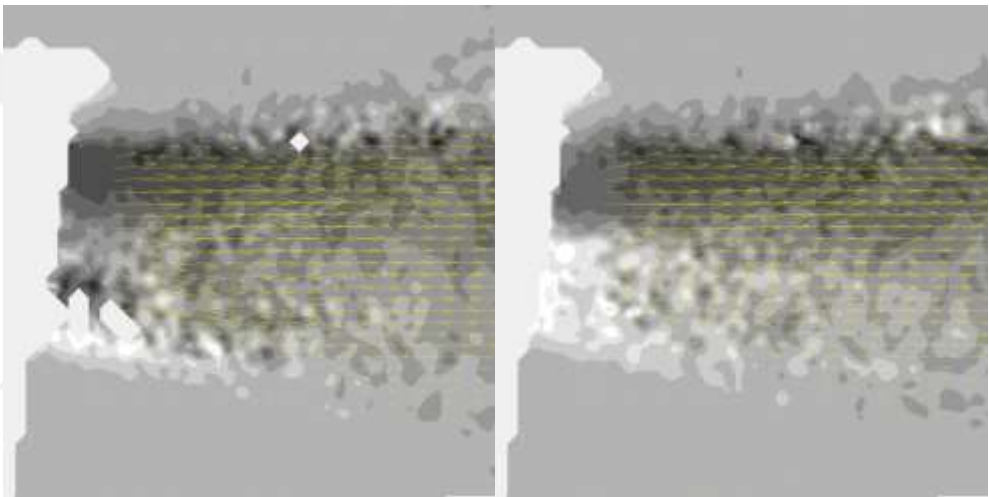
(18)

Figure 6.2 continues



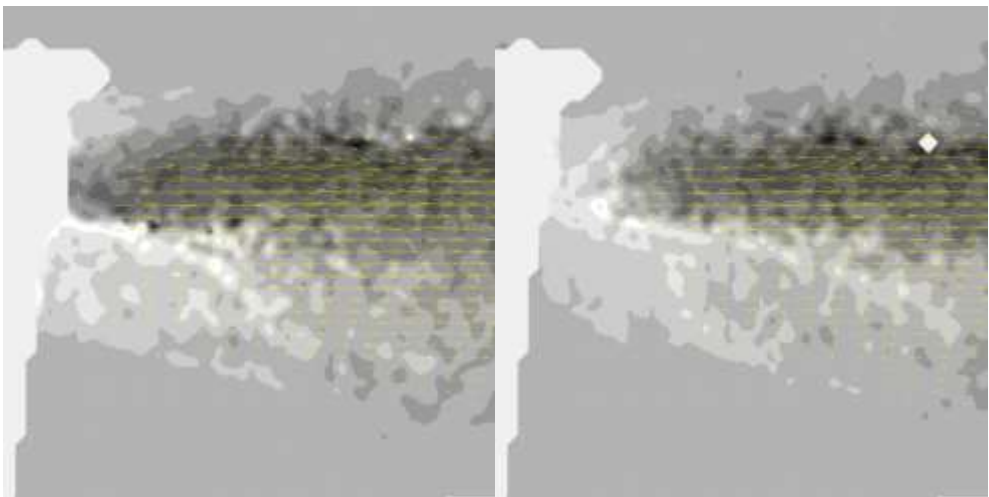
(19)

(20)



(21)

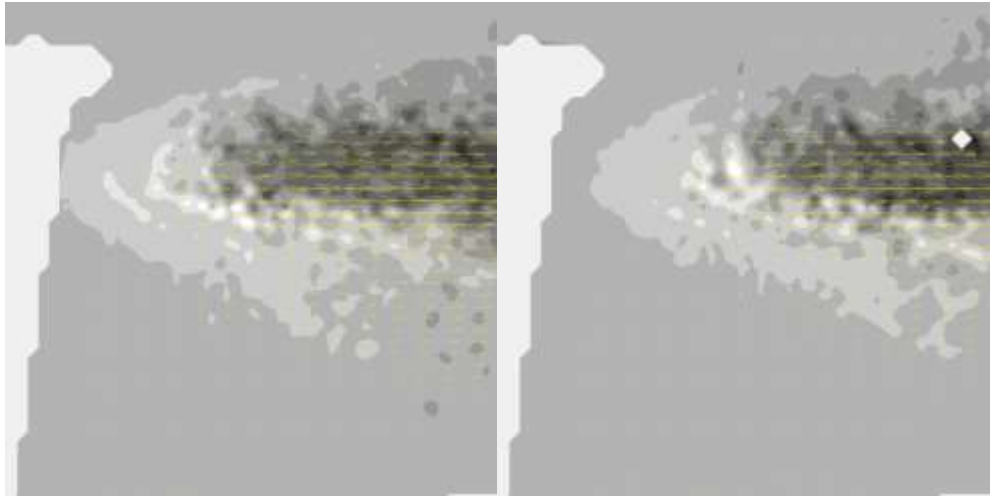
(22)



(23)

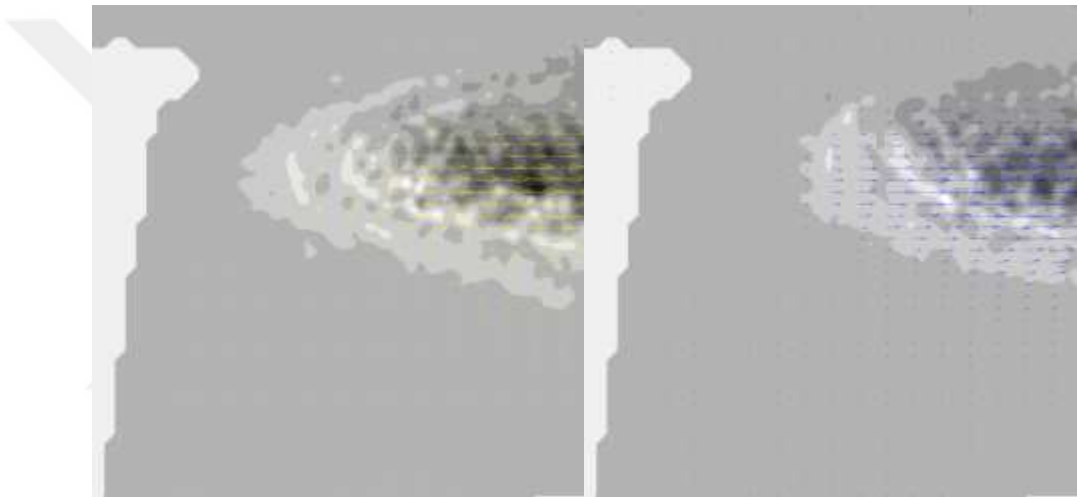
(24)

Figure 6.2 continues



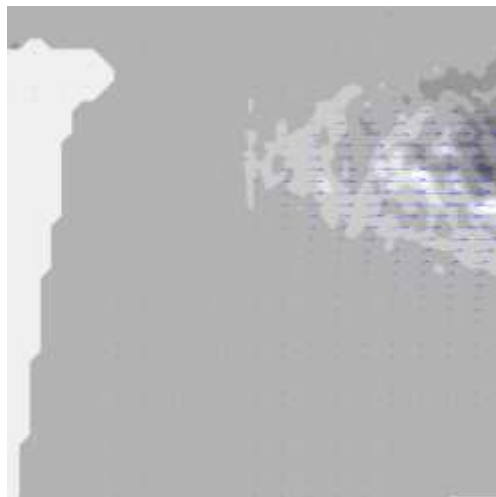
(25)

(26)



(27)

(28)



(29)



Figure 6.2 continues

In the following stage of the study, by interpolating the planer 3D average velocity data obtained from different measurement planes, the volumetric 3D velocity data is generated. By conducting this study, the data evaluation and investigation method is completed.

Following this stage, by utilizing this method the suction section of the fan is investigated. Furthermore, an alternative fan that is considered to be used in the system is compared with the current fan with PIV method.

6.2 Investigation of the 3D Flow Profile of the Centrifugal Fan Output Mouth

In the previous section, PIV experiments are conducted throughout the blowing mouth of the centrifugal fan and flow profiles in 29 cross sections throughout the mentioned blowing mouth were obtained. This study is conducted in order to generate the 3D flow profile by utilizing the obtained planes. The locations of the experiment planes throughout the fan mouth is shown in Table 6.1. In Figure 6.3 the relation of the mentioned planes' locations and the investigated volume is visualized.

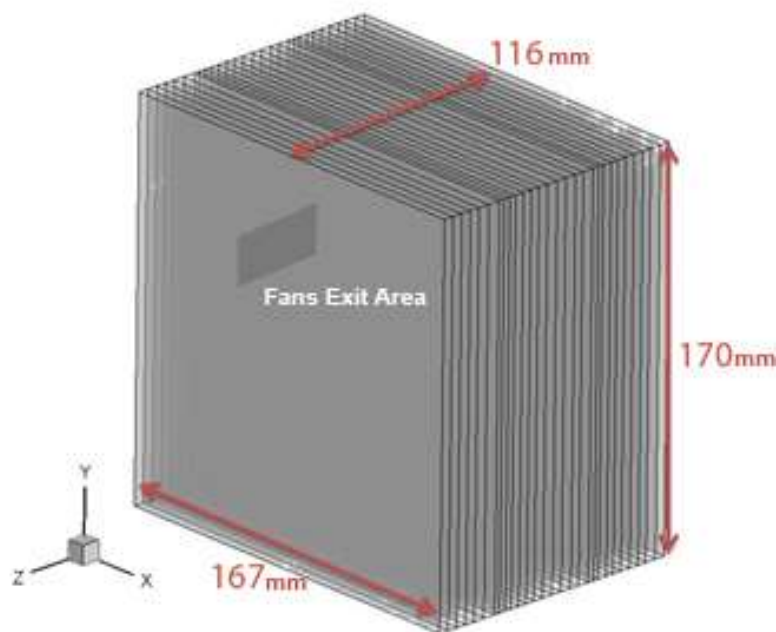


Figure 6.3 Locations of the investigated planes on the flow structure

In order to fully capture the flow structure, the scan intervals of the measurement points are taken larger than the mouth section. The first laser plane is located 30 mm outside the centrifugal fan output mouth and this point is taken as a reference, the subsequent planes are placed throughout the output mouth. As the measurements were taken, instead of a scan with a constant interval, the frequency of the scans are increased at critical regions. The total number of measurement plane is an odd number, the reason behind this is to provide symmetry.

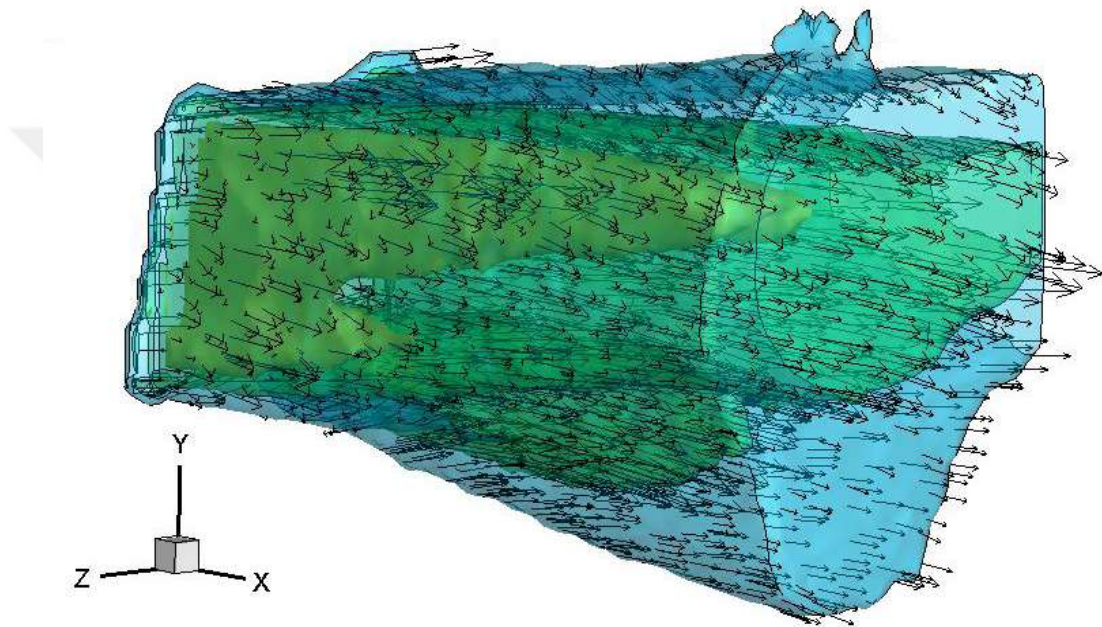


Figure 6.4 Matching velocity surfaces illustrated on the volumetric 3D velocity data obtained via interpolation of the planar 3D velocity data compiled throughout the blowing mouth of the centrifugal fan (Inner Surface 12 m/s, Central Surface 7 m/s, Outer Surface 3 m/s)

The planar 3d average velocity maps obtained from these planes individually were provided in part 6.1. The mentioned vector maps are taken as input to the Tecplot software and after conducting evaluation, the interpolated volumetric 3D average velocity map is compiled (Figure 6.4).

6.3 Investigation of the 3D Flow Profile of the Centrifugal Fan Suction Mouth

The suction side of the fan also investigated. In order to achieve this, the method structured in the prior section is replicated and the suction section of the fan is investigated.

As a result of the investigation it is determined that the flow structure is stable as expected. Figure 6.5 Iso-surfaces of velocity illustrated on the volumetric 3D velocity data obtained via interpolation of the planar 3D velocity data compiled throughout the suction mouth of the centrifugal fan. The surfaces starting from inner and going to outer surfaces, shows where 1 m/s, 2 m/s and 3m/s velocities are formed.

As expected, the suction is symmetrical on all directions. However, when investigated with the surface, it is seen that the flow takes form of a flat semi sphere. This shows that the flow perpendicular to the suction mouth has a higher velocity. The fundamental reason behind this phenomenon may be the incoming flow losing a certain amount of energy via friction.

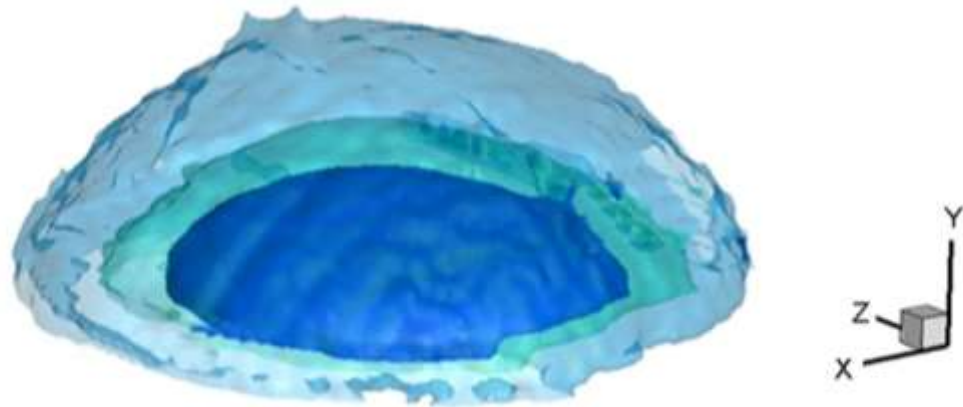


Figure 6.5 Matching velocity surfaces illustrated on the volumetric 3D velocity data obtained via interpolation of the planar 3D velocity data compiled throughout the suction mouth of the centrifugal fan (Outer 1 m/s, central 2 m/s, inner 3m/s)

6.4 Comparison of Alternative Centrifugal Fans

In this section of the study, the centrifugal fan that is considered by the company as an alternative and investigated in the numerical study is compared to the centrifugal fan in the current model by PIV method.

In order to extensively compare the two fans, the experiments are replicated including the same locations. In these experiments PIV measurements were taken from 30 planes with 5 mm intervals. Following this stage, by following the process phases where the output mouth 3D flow profile is investigated and finalized, the volumetric 3D flow structures of the fans are obtained. The results are shown in Figure 6.6.

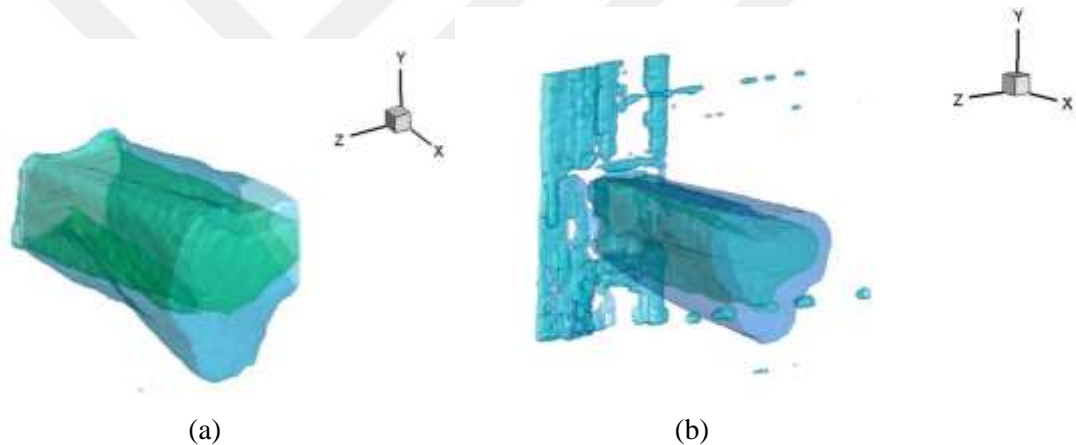


Figure 6.6 Matching velocity surfaces illustrated on the volumetric 3D velocity data obtained via interpolation of the planar 3D velocity data compiled throughout the blowing mouth of the centrifugal fan (Inner Surface 7 m/s, Outer Surface 3 m/s) (a) the current high diameter plastic fan (b) small diameter metal fan

As the results obtained are reviewed, it is observed that the fan with metal flaps being considered as an alternative provides a blowing flow at a higher velocity and shows less dispersion compared to the fan with plastic flaps. Furthermore, two fans that are manufactured by different materials, have different amount of flaps and even different fan diameters generating a similar flow structures may be an indication that how much the fan housing has effect on the flow. At this point it is estimated that the flap structure, flap type and the amount of flaps of a fan have a strong influence on the performance, however the fan housing has a strong influence on the flow structure.

6.5 Single Piece Heating Housing Design Studies

The components of the drier system is investigated as a whole and individually and the component most suitable for enhancement is determined. In light of the information obtained from this, the first work item in the design enhancement works is developing a single piece heater housing instead of a router plastic part and remodelling the housing based on this is initiated. The new prototype is given in Figure 6.7.

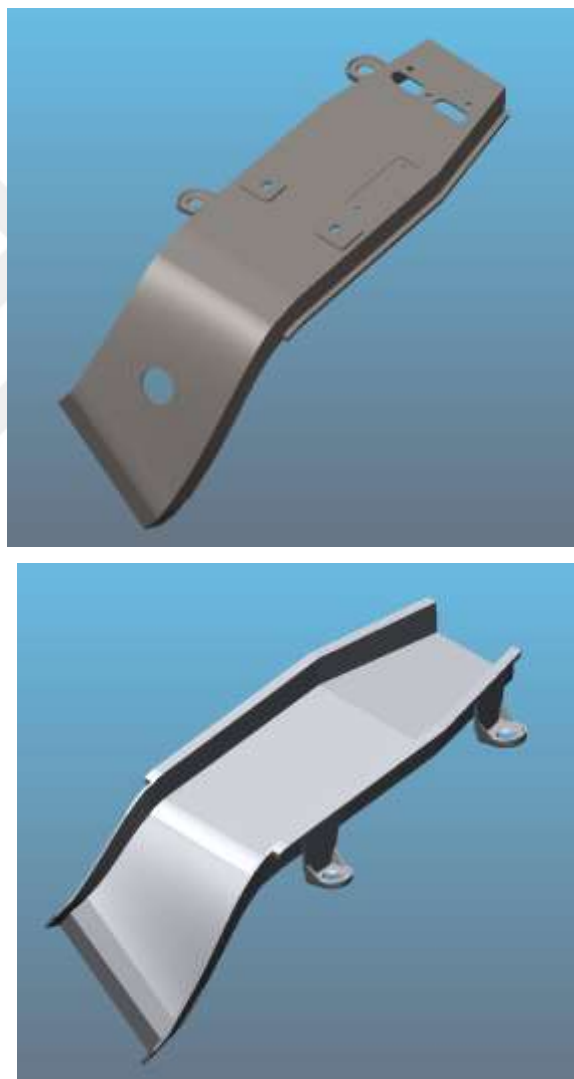


Figure 6.7 3D model of the single piece heater housing design works

In light of the conducted parametric numerical study done with Funda Kuru, as a result of forming the new heating housing canal in order to improve the flow structure and switching to solid design, numerical analysis and experimental verification works are conducted on two different heating housing where the canal width is narrowed by 12 mm and the routing mouth is redesigned.

The air volume model of the current design (a) and the air volume models of the blowing mouth that is redesigned with the purpose of improving the flow structure taking the heating canal that is formed in align with the parametric studies (b and c) are shown in Figure 6.8.

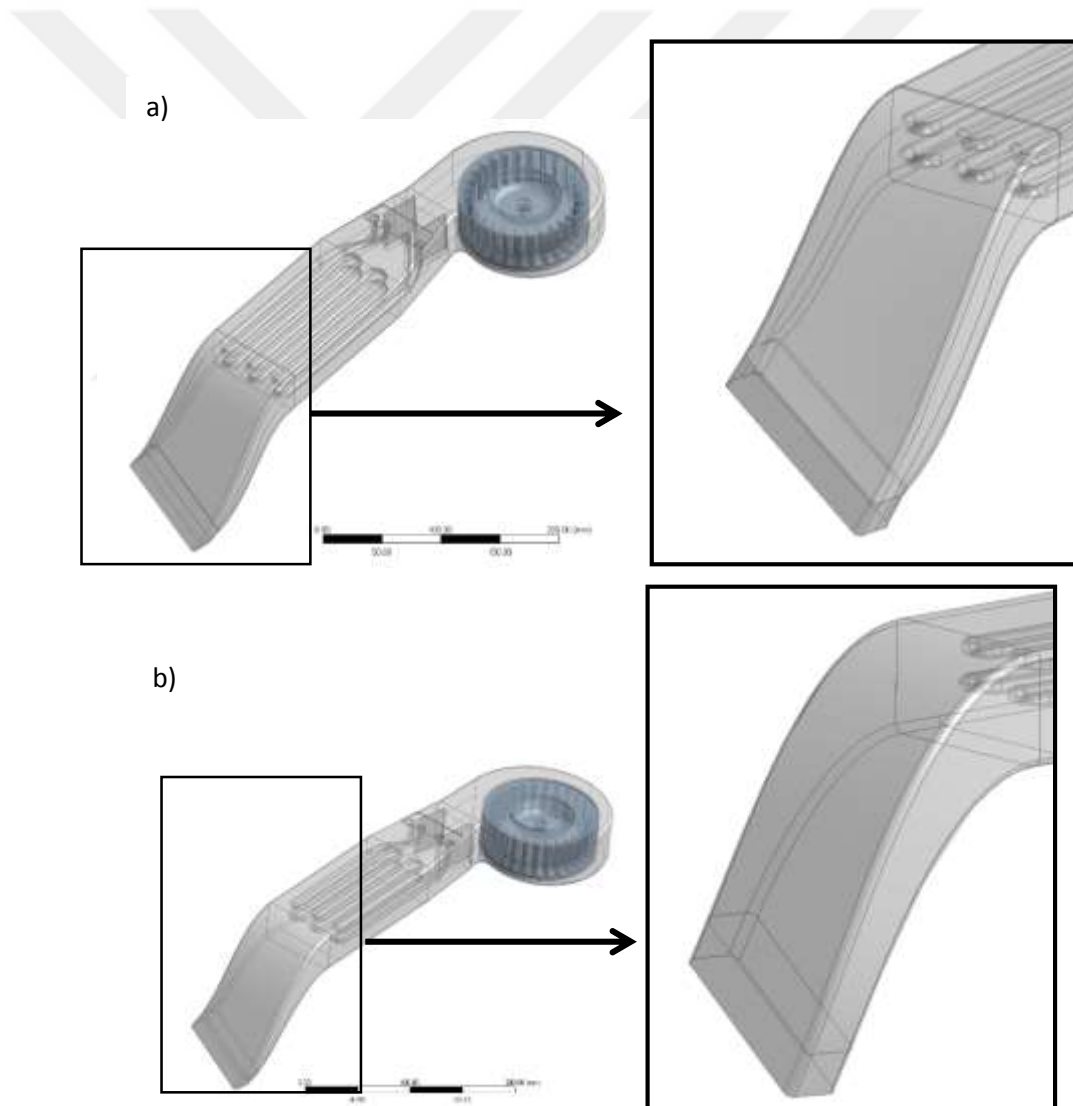


Figure 6.8 Air volume geometries of drier group a) Current state b) Design offer

These models then constructed by 3d printers. The general view of the prototype constructed is provided in Figure 6.9 and 6.10. In particular, the detailed view of the routing plastic part which is considered as a critical section for redesign is provided in Figure 6.11 and the detailed view of the resistance is provided in Figure 6.12. The manufactured prototype then connected to the current fan that is accepted applicable in previous studies that is painted black in order to prevent the laser to reflect and harm the researchers or the cameras and the PIV experiments are conducted.



Figure 6.9 The downside view of the prototype heating housing manufactured for design offer-2 (Personal archive, 2014)



Figure 6.10 The side view of the prototype heating housing manufactured for design offer (Personal archive, 2014)



Figure 6.11 The routing plastic section of the prototype heating housing manufactured for design offer (Personal archive, 2014)



Figure 6.12 The detailed photograph of the resistance section of the prototype heating housing manufactured for design offer (Personal archive, 2014)

As conducted previously, the PIV experiments are conducted by scanning the output mouth and 200 image couples are taken from each investigation plane. By conducting required digital image processing on the obtained image couples and made ready for analysis, then the analysis is conducted by utilizing the identical correlation methods used in prior experiments. Following completing the post processing, the average 3D vector map is generated for each investigation plane.

As these results are investigated, it is observed that throughout the routing plastic part, the flow profile disperse homogenously compared to the prior design and velocities at the jet core is increased. The change in lesser extent throughout the profile, considering the edge effects by jet flow and stationary air coming in contact, can be identified as normal. In order to evaluate the differences with the prior prototype thoroughly, volumetric 3D velocity vectors are obtained by interpolation through the planar 3D velocity vector maps. The flow profile of the prior prototype provided in the prior reports are shown in Figure 6.13, the flow prototype of the new prototype is shown in Figure 6.14.

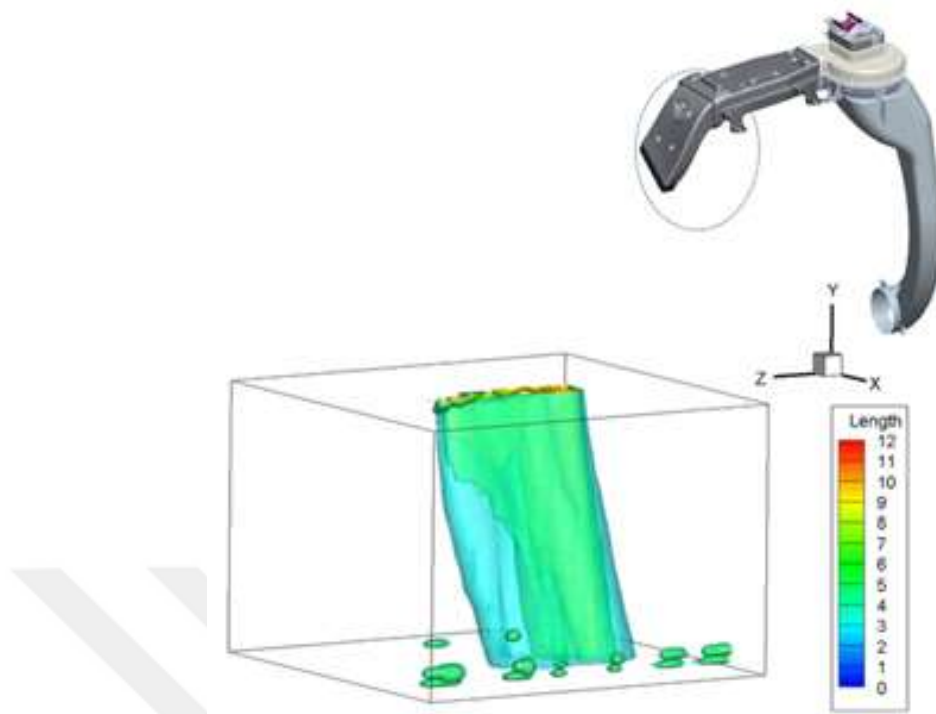


Figure 6.13 Iso-velocity surfaces of the prior routing plastic part obtained via SPIV method

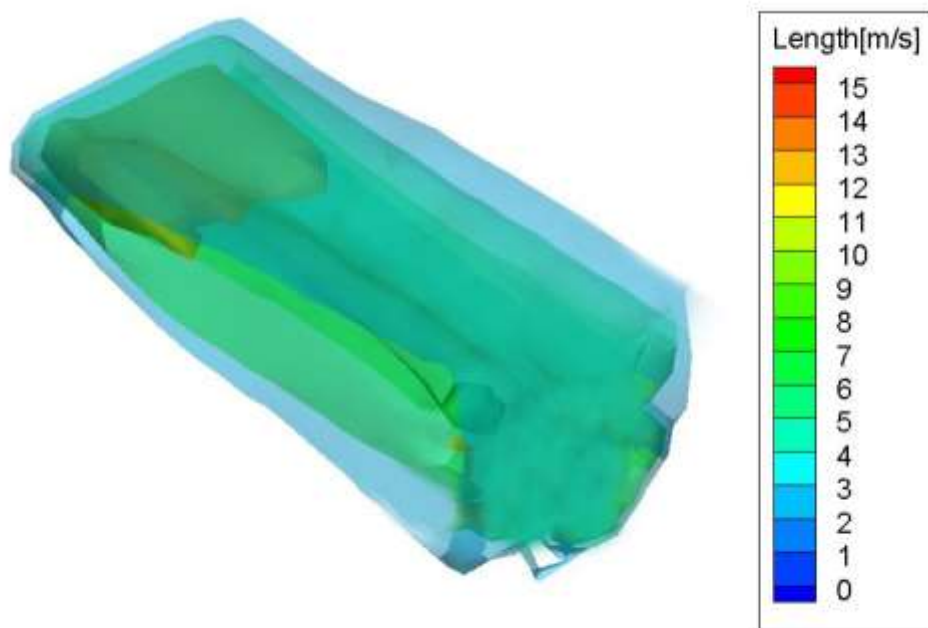


Figure 6.14 Iso-velocity surfaces of the new routing plastic part obtained via SPIV method.

When Figure 6.13 is observed, it is seen that the flow profile formed by the former prototype is asymmetrically leaning on the right wall. On the other hand the flow structure formed new heating housing, resistance and routing channel, as provided in

Figure 6.14, is dispersing homogenously throughout the output mouth. Furthermore, when the jet cores in two figures are investigated, it is seen that the jet core of the new prototype is 13 m/s, the former is 12 m/s. This is an expected outcome due to the reduced width of the channel. However a significant change in two cores and flow profile areas indicates a gain in flow rate. In addition, jet streams in higher velocities tend to penetrate the laundry at a higher rate.



CHAPTER SEVEN
COMPARISON EXPERIMENTS OF 3D MESHED INFRARED
THERMOGRAPHY

7.1 Experimental Comparison of Two Dimensional Targets

In this part of the study meshed infrared thermography method is experimentally compared with the other measurement screens which are plane measurement screen and thin wire measurement screen.

A metal frame with thickness of 1 mm is used for carrying all the measurements screens. The plane measurement screen is made of paper based material with the thickness about 0.1 mm. The thin wire measurement screen is made of plastic based material with the radius about 0.2 mm. The gap between the wires is about 1.4 mm.

These three measurement screens are investigated in terms of temperature measurement performance and flow distortion. The CFF which is used for validation experiments also used in these comparison experiments. It must be noted that these comparisons are made in two dimensions due to the fact that plane and thin wire measurement screen cannot be applied in three dimensions.

7.1.1 Comparison of Temperature Measurement Capabilities of Measurement Screens

The experimental setup used for validating MIT method is also used for comparison of temperature measurement capabilities of measurement screens. Five measurement points are selected in the core of the jet for quantitative comparison. The gap between two points is 25 mm. Temperature measurement with thermocouples is also done at these points for validation of the comparison.

In Figure 7.1, the temperature values measured at these points are given. Figure 7.2 shows temperature distributions obtained by MIT, Plane Target and Thin Wire Target. The temperature measurement points are also marked in Figure 7.2.

Figure 7.1 shows that the closest results to the thermocouple measurement are obtained by MIT method. The average absolute error of the MIT results is 0.48 °C. However, MIT results has a slight fluctuation due to image processing effects. This fluctuation can be decreased by increasing the resolution of the thermal camera or decreasing the distance between the thermal camera and the target which also enhanced the accuracy of the results.

When the trend of the plane target is examined, it is observed that it measures 1.51 °C higher at every measurement point. The reason of this is the plane target transfers the heat of the hot jet also by conduction. Therefore, temperature distribution diffuses more. This phenomenon also can be seen in Figure 7.2. In Figure 7.2-a and c, the temperature distribution was not expanded downward because the jet did not affect this area. However, in Figure 7.2-b, the temperature distribution also expanded downward due to conduction of the plane target.

The Thin Wire Target's results have the highest amount of absolute error with the average of 7.29 °C. This measurement error occurred because the thin wires did not fill the pixel areas and the results represent area weighted average of the thin wire and the background. The amount of error would increase as the temperature difference between the jet and the background.

It must be noted that in this experiments, the targets are placed parallel to the flow which creates minimum drag coefficient. As it is also indicated in Chapter 2, as the angle of attack increases, the flow distortion which is created by the plane target and the thin wire target will also increase that deform the temperature distribution.

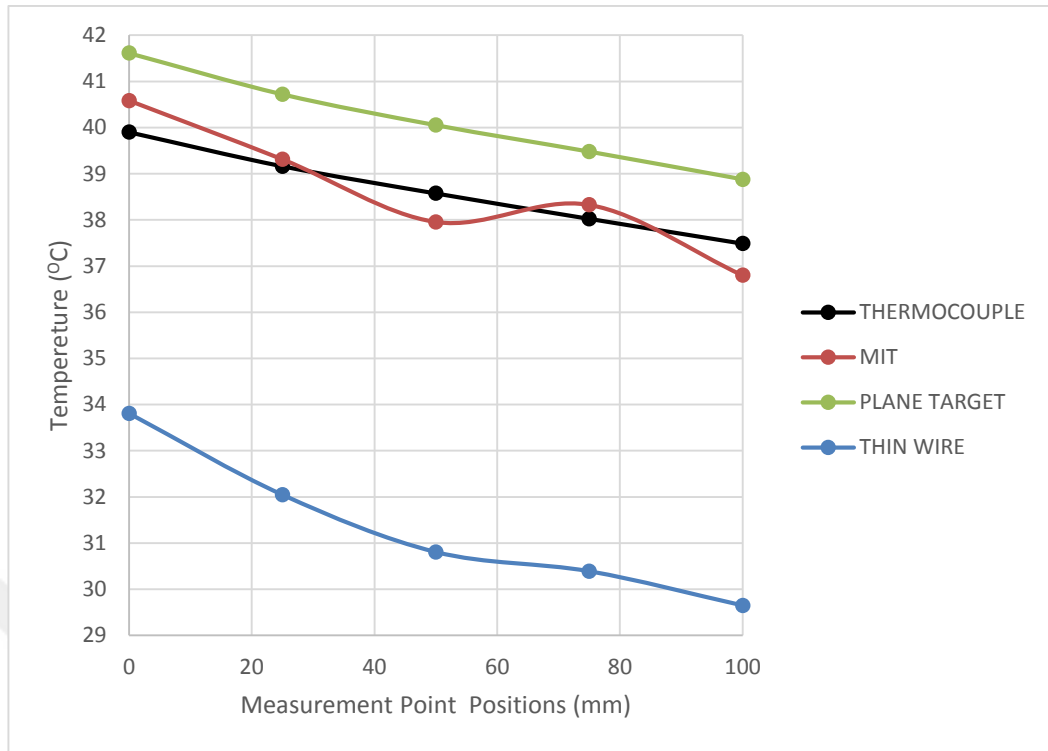


Figure 7.1. Comparison of average temperature measurement obtained by measurement screens and thermocouples

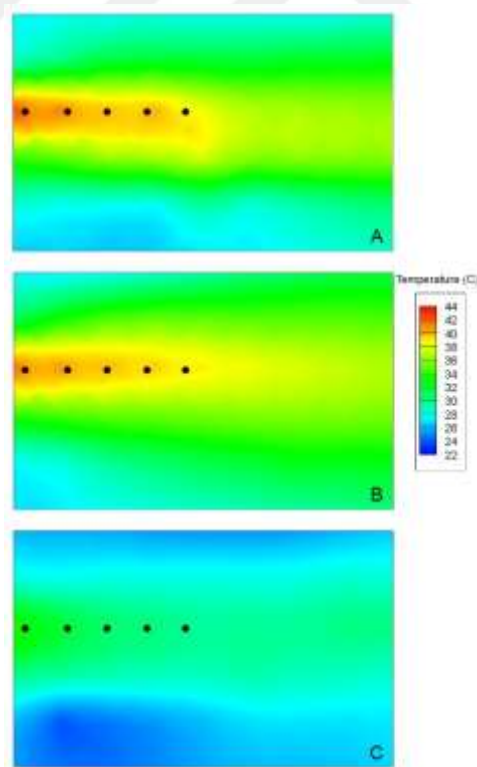


Figure 7.2 Comparison of average temperature distribution obtained by a) MIT, b) Plane target, c) Thin wire target

7.2 3D Flow Structure Validation of 3D Meshed Infrared Thermography by Particle Image Velocimetry

As a final result of 3D MIT, the data obtained from measurement mesh used for reconstruction of volumetric temperature distribution. At the first step of this process, the temperatures of the spheres in the thermal image of the target are matched to the positions of the spheres at the three-dimensional space. This matching can be done manually or automated algorithms can be used by taking advantage of fix geometry of the measurement target. Then, the measured temperatures positioned in the virtual 3D media for visualizing. For a clearer view, iso-temperature surfaces calculated and given in Figure 7.3-a. In Figure 7.3-b, average volumetric velocity iso-surfaces were reconstructed by using SPIV method for validating and comparing the flow structure. For acquiring this data, 16 equal spaced measurement planes were selected throughout the outlet of the CFF and SPIV experiments are done in this planes. Then, two dimensional three component velocity maps are obtained for each measurement plane. The gathered data planes are placed sequentially within a three dimensional space in a virtual environment and interpolated to form the average three dimensional flow field of the CFF.

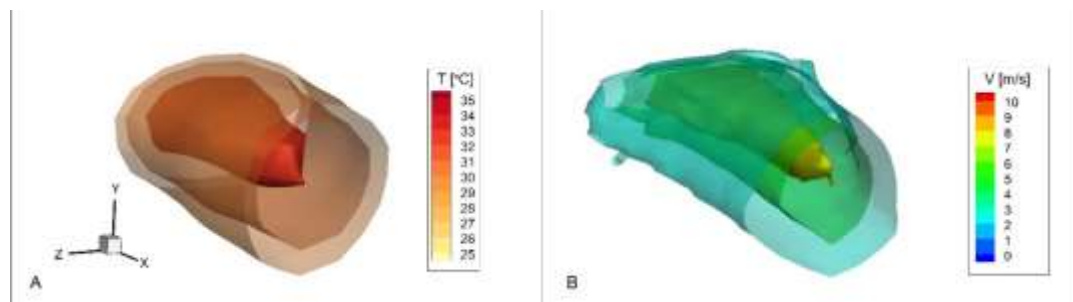


Figure 7.3 a) Average volumetric temperature iso-surfaces of CFF obtained by 3D MIT, b) Average volumetric velocity iso-surfaces of CFF obtained by PIV

While 3D MIT measures temperature, SPIV measures velocity. So, it can be said that quantitatively comparison cannot be done between these results. However, when a hot jet is blown into the stationary air, the jet flow loses both its temperature and velocity due to its mixing with the surrounding air. Therefore, the iso-surfaces of

temperature and velocity measurement would be alike an each other in the geometrical sense. In Figure 7.3-a and b, this phenomenon can be seen.

Based on all these results, it can be said that the 3D MIT method can be successfully used in investigating the 3D flow characteristics.



CHAPTER EIGHT

CONCLUSION

In this thesis, fan driven flow fields were investigated by using Particle Imaging Velocimetry (PIV) and infrared thermography methods.

Improvements in the PIV method have been made which enables in detail research of three-dimensional flow fields. In addition, Three Dimensional Meshed Infrared Temperature Measurement method has been developed that can measure the volumetric temperature distribution of air with a single camera. Then these methods used for the investigation of the fan driven flow fields in variety of devices.

The flow effects of the CFF's casing parameters were investigated over 480 experiment sets. A total of 384000 images were captured. These investigated parameters were the tongue angle, vortex wall distance, vortex wall angle, volute curvature and the presence of a heat exchanger.

As a single parameter's individual effects were investigated, we observed that vortex wall angle (11.63% effect on flow rate), volute curvature (32.03 % effect on flow rate) and the presence of a heat exchanger have strong influence on the SAC flow structure. However, the tongue angle and the vortex wall distance to the fan cause only minor changes to the output parameters. We should noted that the vortex wall distance to the fan influences the vorticity to some extent.

One of the important results derived from this study is the fan and fan casing designs for the SAC units and how the effect of a heat exchanger on the flow structure shall be taken into consideration. As shown by the experiments, merely including the heat exchanger to an overall well performing fan design does not provide the best results. Therefore, in designing the SAC units, the fan design and the heat exchanger must not be considered independently and instead shall be designed to complement one another.

Furthermore, at the end of this study, a well performing and an industrially successful SAC unit was manufactured, indicating the success of the methodology. We note that this methodology was applied over a relatively small research group, which is further evidence that this methodology offers a wide data range that can be gathered and processed to provide a successful product within a small work group.

In future studies, additional parameters, such as the fan, the heat exchanger or additional casing parameters, may be added to the ones investigated in this paper to enable new design alternatives for SAC units. In addition, the adoption of artificial intelligence in data processing to compile and handle the data obtained from this study and future studies may be considered as an alternative. Therefore, more refined and accurate solutions will be able to be created.

The outdoor unit also investigated in the scope of this thesis. When all the results are evaluated; it was determined that the new axial fan outdoor unit designed within this thesis's average air flow rate is 14.17% higher than the existing outdoor unit and 17.9% higher in the working cycle. The advantage of this air flow rate allows the fan to achieve the desired output at lower speeds. Thus, the outdoor unit with a new axial fan has 2.43 dBA lower sound level than the current outdoor unit at the need air flow rate. In the case of maximum air flow rate demand in the eastern provinces, this difference is up to 4.66 dBA. In the direction of these results, studies were started by the company about the mass production of the newly designed axial fan outdoor unit. The prototype of the outdoor unit with a CFF has successfully met the lower sound expectation, which is the forecast for the beginning of the project. Although the new axial fan outdoor unit developed within the scope of the project has higher success than the outdoor unit with CFF, the outdoor unit with CFF offers potential for low noise SACOU.

Another aim of this study was to investigate the heat transfer and fluid (air) flow characteristics of domestic ovens with aspirating cooling system (ACS) systems by implementing numerical methods. A prototype pyrolytic domestic oven was used. In the literature, numerical and experimental studies have been conducted for measuring

the heat transfer and air flow inside oven cavities and within oven doors. The oven door and its upper fan provide active air suction from the door and were modelled using a CFDHT method. The numerical results were validated by comparing with results obtained from experimental tests. In the literature, only a few studies have observed the heat transfer mechanisms of the oven door. A combined oven door and ACS was modelled in three dimensions, and parametric studies were performed. First, the ACS was modelled, and fluid flow was investigated. Based on these parametric studies, a new ACS model was developed with optimized CFF position and ACS channel geometry. After improving the ACS, the oven door and ACS were modelled together, and the outer surface temperature distribution of the oven door was investigated. Furthermore, the airflow Reynolds number was parametrically investigated.

The computational results show that the designs of ACS channels, the CFF position and the rotational speed of CFF play important roles on the outer surface temperature distributions of the oven door and the flow fields of the ACS. These predictions are proven by experimental comparison of these models. The maximum temperature of the oven door decreased 65 K and the average temperature decreased 25.25 K in respect to the oven without ACS.

These results shown that ACS can strongly reduce the surface temperature at the oven door which enables to design cool touch ovens even in the pyrolytic function where the inner temperature of the oven reach about 723 K.

It must be noted that these results can be improved by increasing the number of the design parameters such as the diameter of the CFF, the positions of the oven door glasses... etc. Also it must be taken to the consideration that the investigated flow structures include laminar, turbulent and transition regions therefore slight changes of design parameters may significantly affect the results.

The ongoing researches also showed enhancement of the materials also has strong effect on the surface temperature. However, the aerodynamic design must be revised

according to these properties. For decreasing the solution time, artificial intelligence algorithms such as artificial neural networks may be also integrated to the solution method for the future studies.



REFERENCES

- Abraham, J.P., & Sparrow, E., M. (2004). A simple model and validating experiments for predicting the heat transfer to a load situated in an electrically heated oven. *Journal of Food Engineering*. 62, 409–415.
- Adrian, R. J. (2005). Twenty years of particle image velocimetry. *Experiments in Fluids*, 39, 159-169.
- Alava, I., Onederra, U., Marin, R., & Laresgoiti, A. (2003). Comparison between PIV measurements and CFD modelling on a domestic gas oven. *In Pivnet2 Workshop On PIV Application to Appliances*.
- Anderson, R., Hassani, V., & Kirkpatrick, A. (1991). Visualizing the air flow from cold air ceiling jets. *ASHRAE Journal*, 33, 30-35.
- Araneo, L., Coghe, A., & Solero, G. (2003). Natural gas burners for domestic appliances: application of the particle image velocimetry technique (PIV). *In Pivnet2 Workshop on PIV Application to Appliances*.
- Auteri, F., Belan, M., Ceccon, S., Gibertini, G., & Quadrio, M. (2006). Endoscopic PIV in a helical pipe coil. *Dipartimento Di Ingegneria Aerospaziale Politecnico Di Milano Via La Masa 34, 20156 Milano*.
- Bricaud, C., Richter, B., Dullenkopf, K., & Bauer, H. J. (2005). Stereo PIV measurements in an enclosed rotor stator system with pre-swirled cooling air. *Experiments in Fluids*, 39-2, 202–212.
- Burch, S. D., Hassani, V., & Penney, T. R. (1992). Use of infrared thermography for automotive climate control analysis. *Warrendale: National Renewable Energy Laboratory*.

- Canepa, E., Cattanei, A., & Zecchin, F., M. (2015). Effect of the rotor–stator gap variation on the tonal noise generated by axial-flow fans. *Applied Acoustics*, 94, 29–38.
- Casarsa, L., & Giannattasio, P. (2011). Experimental study of the three-dimensional flow field in cross-flow fans. *Experimental Thermal and Fluid Science*, 35, 948–959.
- Cehlin, M., Moshfegh, B., & Sandberg, M. (2002). Measurements of air temperatures close to a low-velocity diffuser in displacement ventilation using an infrared camera. *Energy and Buildings*, 34, 687–698.
- Dabiri, D. (2009). Digital particle image 15 thermometry/velocimetry: A review. *Experiments in Fluids*, 46, 191–241.
- Datong, Q., Yijun, M., Xiaoliang, L., & Minjian, Y. (2009). Experimental study on the noise reduction of an industrial forward-curved blades centrifugal fan. *Applied Acoustics*, 70, 1041–1050.
- Dierksheide, U., Meyer, P., Hovestadt, T., & Hentschel, W. (2002). Endoscopic 2D particle image velocimetry (PIV) flow field measurements in ic engines. *Experiments in Fluids*, 33.
- Earth overshoot day*. (n.d.). Retrieved August 11, 2017, from <http://www.overshootday.org/>
- Airboss image*. (n.d.). Retrieved October 01, 2017, from <http://www.airbus.com>
- Eck, B. (1973). *Design and operation of centrifugal, axial flow and cross flow fans*. Oxford: Pergamon Press.

- Elvsén, P., & Sandberg, M. (2009). Buoyant jet in a ventilated room: velocity field, temperature field and air flow patterns analyzed with three different whole-field methods. *Building and Environment*, 44, 137-145.
- Fahey, M., Wakes, S. J., & Shaw, C. T. (2008). Use of computational fluid dynamics in domestic oven design. *The International Journal of Multiphysics*. 1, 37-57.
- Gabi, M., Dornstetter, S., & Klemm, T. (2003). Flow field and performance of Cross flow fans - Experimental and theoretical investigations. *Journal of Thermal Science*, 12, 234-238.
- Gallo, M., Kunsch, J. P., & Rösgen, T. (2010). A novel infrared thermography (IRT) based experimental technique for distributed temperature measurements in hot gas flows. *10th International Conference on Quantitative Infrared Thermography*, , Quebec.
- Harari, Y. (2016). *Hayvanlardan Tanrılara – Sapiens*. Kolektif Kitap.
- Hu, S., S., & Huang B., J. (2005). Study of a high efficiency residential split water-cooled air conditioner. *Applied Thermal Engineering*, 25, 1599-1613.
- Incropera , F. P., & DeWitt, D. P. (1996). *Fundamentals of heat and mass transfer (Fourth Edition b.)*. New York: John Wiley & Sons.
- Karadeniz, Z. H., Kumlutaş, D., & Özer, Ö. (2013) Experimental visualization of the flow characteristics of the outflow of a split air conditioner indoor unit by meshed infrared thermography and stereo particle image velocimetry. *Experimental Thermal and Fluid Science*, 44, 334-344.
- Karadeniz, Z. H., Kumlutaş, D., & Özer, Ö. (2013). Experimental visualization of the flow characteristics of the outflow of a split air conditioner indoor unit by meshed

- infrared thermography and stereo particle image velocimetry. *Experimental Thermal and Fluid Science*, 44, 334-344.
- Kim, J. W. (2003). Mixed flows near inlet air-conditioner. In *Pivnet2 Workshop On PIV Application to Appliances*.
- Krause, N., Zahringer, K., & Pap, E. (2005). Time-Resolved particle imaging velocimetry for the investigation of rotating stall in a radial pump. *Experiments in Fluids*, 39, 192-201.
- Kühn, M., Bosbach, J., & Wagner, C. (2009). Experimental parametric study of forced and mixed convection in a passenger aircraft cabin mock-up. *Building and Environment*, 44.
- Kumlutaş, D., Karadeniz, Z. H., & Kuru, F. (2013). Investigation of flow and heat transfer for a split air conditioner indoor unit. *Applied Thermal Engineering*, 51, 262-272.
- Lazar, E., De Blauw, B., Glumac, N., Dutton, C., & Elliott, G. (2010). A practical approach to piv uncertainty analysis. *27th AIAA Aerodynamic Measurement Technology and Ground Testing Conference*, Chicago.
- Lazzarato, M., Meneghin, G., & Scattolin, M. (2003). PIV applied to the internal fluid dynamics of close control air-conditioning systems. In *Pivnet2 Workshop On PIV Application to Appliances*.
- Lazzaretto A. (2003). A criterion to define cross-flow fan design parameters. *Journal of Fluids Engineering*, 125 (4), 680-683.
- Lazzaretto, A., Toffolo, A., & Martegani, A. D. (2003). A systematic experimental approach to cross-flow fan design. *Journal of Fluids Engineering*, 125, 680-683.

- Lazzarotto, L., Lazzaretto, A., Macor, A., & Martegani, A.D. (2001). On cross-flow fan similarity: effects of casing shape. *Journal of Fluids Engineering*, 123 (3), 523-531.
- Lee, W. L., Chen, H., & Yik, F. W. H. (2008a). Modeling the performance characteristics of water-cooled air-conditioners. *Energy and Buildings*, 40, 1456-1465.
- Lee, W. L., Chen, H., & Yik, F. W. H. (2008b) Applying water cooled air conditioners in residential buildings in Hong Kong. *Energy Conversion and Management*, 49, 1416-1423.
- Meinhart, D. C., Wereley, T. S., & Santiago, G. J. (2000). A PIV algorithm for estimating time-averaged velocity fields. *Journal of Fluids Engineering*, 122, 285-289.
- Miles, R., & Lempert, W. (1990). Two-dimensional measurement of density, velocity, and 25 temperatures in turbulent high-speed air flows by UV rayleigh scattering. *Applied Physics B Photophysics Laser Chem*, 51, 1-7.
- Mistry, H., Ganapathi-subbu, S., Dey, S., Bishnoi, P., & Castillo, J. L. (2006). Modeling of transient natural convection heat transfer in electric ovens. *Applied Thermal Engineering*, 26, 2448-2456.
- Mistry, H., Ganapathisubbu, S., Dey, S., Bishnoi, P., & Castillo, J.L. (2011). A methodology to model flow-thermals inside a domestic gas oven. *Applied Thermal Engineering*. 31, 103-111.
- Murata, S., & Nisnihara, K. (1976a). Experimental study of cross flow fan - 1. Effects of housing geometry on the fan performance. *Bull JSME*, 19 (129), 314-321.

- Murata, S., & Nisnihara, K. (1976b). Experimental study of cross flow fan - 2. Movements of eccentric vortex inside impeller. *Bull JSME*, 19 (129), 322-329.
- Neely, A. J. (2008). Mapping Temperature Distributions in Flows Using Radiating High-Porosity Meshes. *Experiments in Fluids*, 45, 423-433.
- Neto, L. P., Gambero Silva, M. C., & Costa, J. J. (2006). On the use of infrared thermography in studies with air curtain devices. *Energy and Buildings*, 38, 1194-1199.
- Özer, Ö., & Kumlutaş, D. (2017). Experimental investigation on cross flow fan's casing parameters inside of a split air conditioner indoor unit by Stereo Particle Image Velocimetry. *Applied Thermal Engineering*, 124, 1233-1246.
- Paone, N., Marassi, M., & Santonicola, P. (2003). PIV applied to kitchen evacuation hoods. *In Pivnet2 Workshop On PIV Application to Appliances*.
- Raffel, M., Willert, C., Wereley, S., & Kompenhans, J. (2007). *Partical Image Velocimetry: a Pratical Guide*, (2nd. ed.). Springer, Berlin Heidelberg New York.
- Rek, Z., Rudolf, M., Zun, I. (2012). Application of CFD simulation in the development of a new generation heating oven. *Strojniški vestnik - Journal of Mechanical Engineering*. 58, 134-144.
- Rita, S., & Guzzini, A. (2003). Study of lamp cooling by 3d PIV. *In Pivnet2 Workshop On PIV Application to Appliances*.
- Scarano, F., & Riethmuller, M. L. (1999). Iterative multigrid approach in PIV image processing with discrete window offset. *Experiments in Fluids*, 26, Springer-Verlag.

- Schroeder, A., & Willert, E. C. (2008). *Particle Image Velocimetry New Developments and Recent Applications*. Springer-Verlag Berlin Heidelberg.
- Shih, Y. C., Hou, H. C., & Chiang, H. (2004). Numerical study of the similarity law for the cross-flow fan of a split-type air conditioner. *ASHRAE Transactions 110 PART I*, 378-388.
- Shih, Y.C., Hou, H. C., & Chiang H. (2008). On similitude of the cross flow fan in a split-type air-conditioner. *Applied Thermal Engineering*, 28, 1853-1864.
- Smolka, J., Nowak, A. J., & Rybarz, D. (2009). Improved 3-D temperature uniformity in a laboratory drying oven based on experimentally validated CFD computations. *Journal of Food Engineering*, 97, 373–383.
- Sun, K., Ouyang, H., Tian, J., Wu, Y., & Du Z. (2015). Experimental and numerical investigations on the eccentric vortex of the cross flow fan. *International Journal of Refrigeration*, 50, 146-155.
- Toffolo, A. (2005). On the theoretical link between design parameters and performance in cross-flow fans: A numerical and experimental study. *Computers & Fluids*, 34, 49-66.
- Toffolo, A., Lazzaretto, A., & Martegani, A.D. (2004). An experimental investigation of the flow field pattern within the impeller of a cross-flow fan. *Experimental Thermal and Fluid Science*, 29 (1), 53–64.
- Velarde-Suarez, S., Ballesteros-Tajadura, R., Hurtado-Cruz, J. P., & Santolaria-Morros, C. (2006). Experimental Determination of the Tonal Noise Sources in a Centrifugal Fan. *Journal of Sound and Vibration*, 295, 781-796.

- Verboven, P., Scheerlinck, N., Baerdemaeker, J. D., & Nicolai, B. M. (2000). Computational fluid dynamics modelling and validation of the isothermal airflow in a forced convection oven. *J. Food Eng.*, *43*, 41–53.
- Vinnichenko, N., Plaksina, Y., Yakimchuk, O., Soldatenkova, K., & Uvarov, A. (2016). Air flow temperature measurements using infrared thermography. *Quantitative InfraRed Thermography Journal*, 1–15.
- Wang, H., Tian, J., Ouyang, H., Wu, Y., & Du, Z. (2014). Aerodynamic performance improvement of up-flow outdoor unit of air conditioner by redesigning the bell-mouth profile. *International Journal of Refrigeration*, *46*, 173-184.
- Wernet, M. P. (2000). Application of DPIV to study both steady state and transient turbomachinery flows. *Optics & Laser Technology*, *32*, 497-525.
- Wu, C. J., Liu, D. P., & Pan, J. (2012). A study of the aerodynamic and acoustic performance of an indoor unit of a DC-inverter split air-conditioner. *Applied Acoustics*, *73*, 415-422.
- Yamafuji, K. (1975) Studies on the flow of cross-flow impellers - 1. Experimental study. *Bull JSME*, *18* (123), 1018-1025.
- Yoon, J. H., & Lee, S.J. (2004). Stereoscopic PIV measurements of flow behind an isolated low-speed axial-fan. *Experimental Thermal and Fluid Science*, *28*, 791-802.
- Younsi, M., Bakır, F., Kouidri, S. & Rey, R. (2007). Influence of impeller geometry on the unsteady flow in a centrifugal fan: numerical and experimental analysis. *International Journal of Rotating Machinery*, 2007.

Younsi, M., Bakır, F., Kouidri, S., & Rey, R. (2007). 3D unsteady flow in a centrifugal fan: impeller – volute interaction. *Journal of Computational and Applied Mechanics*, 8, 211-223.

Zhao, X., Sun, J. & Zhang, Z. (2013). Prediction and measurement of axial flow fan aerodynamic and aeroacoustic performance in a split-type air-conditioner outdoor unit. *International Journal of Refrigeration*, 36, 1098-1108.

